

**Applications of
Bayesian Probability Theory
in Fusion Data Analysis**

Christopher Bowman

Doctor of Philosophy

University of York

Physics

June 2016

Abstract

Bayesian probability theory is a powerful tool for solving complex problems in experimental data analysis. In this thesis we explore the use of Bayesian methods in magnetic confinement fusion with an emphasis toward developing analysis tools and techniques. The original research content is presented in three chapters. In the first we develop a new approach to efficiently characterising multi-dimensional posterior distributions. This is achieved through an algorithm which, for any number of posterior dimensions, can decide which areas of the probability space contain significant information and evaluate only those areas. This addresses the computational challenges which arise in calculating marginal distributions from many-dimensional posteriors. In the second research chapter Bayesian probability theory is applied to the discrete Fourier-transform of an arbitrary real series containing random noise. The effect of the noise on the Fourier coefficients is used to derive a correction to the Fourier magnitudes, which results in a reduction in the overall noise-level after an inverse-transform. Calculating these corrections requires the solution of a challenging inverse problem which is discussed at length, and several methods for obtaining approximate solutions are developed and tested. The correction itself, plus the methods allowing its calculation together form the basis of a new technique for noise correction which is completely general, as no assumptions are made about the series which is to be corrected. In the final research chapter the inference of physics parameters using the DIII-D CER system is discussed. A Bayesian network approach is used to derive a model for the observed charge-exchange spectrum, which is itself used to construct a posterior distribution for the model parameters. The spectrum model is used to explore the possibility of inferring the time-evolution of physical parameters on sub-integration time-scales.

Contents

Abstract	3
Contents	5
List of Tables	9
List of Figures	10
Acknowledgements	13
Declaration	15
1 Introduction	17
1.1 Fusion as an energy source	17
1.1.1 The demand for renewable energy sources	17
1.1.2 The Deuterium-Tritium fusion reaction	19
1.1.3 Magnetic confinement fusion	20
1.2 Tokamak physics experiments	21
1.2.1 Outline of the tokamak concept	21
1.2.2 Progress toward fusion	23
1.3 Complexity in magnetic confinement fusion	24
1.3.1 This thesis	26
2 Bayesian data analysis	29
2.1 Introduction to Bayesian probability theory	30
2.1.1 The Bayesian view of probability	30
2.1.2 Notation	31
2.1.3 Fundamentals of probability: the sum and product rules	31
2.1.4 Bayes' Theorem	32
2.1.5 Marginalisation	33
2.1.6 Conditional independence	33
2.2 Bayes theorem example: decay of an excited state	34
2.2.1 Potential 'frequentist' approaches to estimating λ	35
2.2.2 Inference from a single time measurement	36
2.2.3 Likelihood of a dataset: multiple time measurements	38
2.2.4 Approaching the frequentist limit	40
2.3 Inference of physics model parameters	42

Contents

2.3.1	Example: Spectroscopy data analysis	42
2.3.2	The model parameter posterior distribution	44
2.3.3	Marginalisation of nuisance parameters	45
2.3.4	Inference of the line widths: $P(w_1, w_2 \mathcal{D})$	46
2.4	Summary	47
3	Developing tools for Bayesian analysis	49
3.1	Introduction	49
3.2	Computational challenges of many-parameter inference	49
3.2.1	Limitations of grid-based approaches	50
3.2.2	Posterior sampling	51
3.3	Improving grid-based approaches	53
3.3.1	The GridFill algorithm	54
3.3.2	Implementation	56
3.3.3	Performance testing	58
3.3.4	A note on parallelisation	60
3.3.5	Comparison with MCMC	62
3.3.6	Future development	63
3.4	Probabilistic calculation of credible region contour densities	65
3.4.1	Constructing the bounding density probability distribution	66
3.4.2	Mean, variance and error scaling	68
3.4.3	Effective presentation of inference results	69
3.5	Summary	71
4	Probabilistic noise-correction of discrete Fourier transform coefficients	73
4.1	Introduction	73
4.2	Random noise in the Fourier domain	75
4.2.1	Relating the time and Fourier domain noise levels	78
4.2.2	Inference of \bar{z}_k	78
4.2.3	The $P(\bar{x}, \bar{y})$ prior distribution	79
4.2.4	Challenges of correcting z_k	80
4.3	Deriving a magnitude correction	81
4.3.1	Distribution of the Fourier magnitude	81
4.3.2	Correcting the magnitudes	83
4.3.3	Analytical result for a uniform prior: $P(S) \propto 1$	85
4.3.4	Analytical result for a half-normal prior	86
4.3.5	Residual error after magnitude correction	87
4.3.6	On the possibility of phase-correction	89
4.4	Estimating the prior distribution $P(S)$	90
4.4.1	Properties of $P(S)$	90
4.4.2	Modifying the inverse problem	93
4.4.3	Bayesian iterative procedure for estimating $P(S)$	96

4.4.4	Linearisation of integral transforms	99
4.4.5	Chebyshev representation and prior constraints	102
4.4.6	Estimating \mathbf{c} via non-linear optimisation	107
4.4.7	Prior-evidence equivalence approximation	110
4.4.8	Comparison of prior estimation techniques	111
4.5	Demonstration of magnitude correction method	112
4.5.1	Inference of σ	113
4.5.2	Selecting the pass-band region of frequency space	115
4.5.3	Calculating the correction factors	116
4.5.4	Demonstration of reduction in magnitude errors	117
4.6	Correction performance testing	118
4.6.1	Investigating ideal correction performance	119
4.6.2	Quantitative comparison of prior estimation techniques	120
4.7	Application to KSTAR ECEI data	122
4.8	Conclusions and further work	123
4.8.1	Potential further work	125
5	Bayesian CER analysis on DIII-D	127
5.1	Introduction	127
5.2	Constructing the CER spectrum	129
5.2.1	Relativistic effects	129
5.2.2	Doppler effects	130
5.2.3	Natural line-width	130
5.2.4	Fine-structure splitting	131
5.2.5	Charge-exchange cross-section variation	131
5.2.6	Non-thermal ion populations	132
5.3	Bayesian inference in CER spectroscopy systems	132
5.3.1	Modelling photon detection probability	133
5.3.2	Distribution of wavelengths for incident photons	135
5.3.3	Model for the instrument function	136
5.3.4	Model for pixel sensitivity	137
5.3.5	Expected counts & time-dependence of the CER spectrum	137
5.3.6	Inference of model parameter distributions	139
5.4	Numerical optimisation of the model	141
5.4.1	Wavelength integration	141
5.4.2	Pixel-width integration	143
5.4.3	Time integration	144
5.5	Effects of time-dependence on predicted spectra	147
5.5.1	Analytical results for linear velocity changes	147
5.5.2	Simultaneous linear changes in v_0 , T_i and R_γ	149
5.6	Inference validation	151
5.7	Summary	153

Contents	
6 Summary & Conclusions	155
Appendix - Estimation of tearing stability parameters using KSTAR ECEI data	159
Bibliography	167

List of Tables

2.1	Parameters used for simulated data generation	43
5.1	DIII-D CER instrument function coefficients	151

List of Figures

1.1	Global energy expenditure by energy source	18
1.2	Deuterium-Tritium reactivity versus plasma temperature	20
1.3	Schematic representation of the tokamak configuration	22
1.4	Fusion triple product in various tokamak experiments	24
1.5	Overview of diagnostics on JET	25
2.1	Posterior distribution for the atomic decay rate example	39
2.2	Simulated CCD data for the spectroscopy example	43
2.3	Joint marginal distribution for the spectral line widths	47
2.4	Univariate marginal distributions for the spectral line widths	48
3.1	Flow diagram representation of the GridFill algorithm	56
3.2	2D example of progressing GridFill evaluations	57
3.3	Summary of GridFill testing results	59
3.4	Example of GridFill evaluation batch sizes	60
3.5	Comparison of GridFill and MCMC methods	63
3.6	Bounding density probability distribution compared with analytic case	67
3.7	Scaling of bounding density variance with sample size	69
3.8	Example of a typical bivariate colour plot	70
3.9	Example of credible contour plotting in a bivariate distribution	71
4.1	KSTAR ECEI channel data from shot 6123	74
4.2	Demonstration of the central limit theorem	77
4.3	Example of the forward-problem integral transform	82
4.4	Analytical results for $E[\tau]$ using half-normal priors	86
4.5	Summary of the audio test signal data	91
4.6	Example of the re-parameterised log-normal distribution	93
4.7	Example results of inversion using the BIPA method	99
4.8	Example results of inversion using the linearisation approach	106
4.9	MCMC sampling results for linear inversion	110
4.10	Applicability of the prior-evidence equivalence approximation	112
4.11	Inference of the Fourier-space noise level σ	114
4.12	Inference of filter cut-off frequencies	116
4.13	Summary of example magnitude correction results	117
4.14	Demonstration of reduced magnitude errors	118
4.15	Summary of ideal correction performance results	120

4.16	Comparison of correction performance for different inversion methods	121
4.17	KSTAR ECEI data noise-correction example	123
5.1	DIII-D charge-exchange system geometry	128
5.2	Bayesian network model of the CER spectrometer-CCD system	134
5.3	Poisson limit of the binomial distribution	140
5.4	Errors incurred from the Gaussian spectrum approximation	142
5.5	Results of simultaneous linear changes in model parameters	150
5.6	Simulated CER data used for validation	152
5.7	Inference results derived from simulated data	152

Acknowledgements

Thank you to my supervisor Prof. Kieran Gibson for his support and advice throughout my PhD studies, and to my friends and colleagues at the York Plasma Institute for many useful discussions which have undoubtedly improved this thesis.

Declaration

I declare that the work presented in this thesis, except where it is otherwise stated, is based on my own research and has not been submitted previously for a degree in this or any other university, and that all sources acknowledged as references. Parts of the work presented in this thesis have been published in:

Minjun J Choi, Gunsu S Yun, Woochang Lee, Hyeon K Park, Young-Seok Park, Steve A Sabbagh, Kieran J Gibson, Christopher Bowman, Calvin W Domier, Neville C Luhmann, Jun-Gyo Bak, and Sang G Lee. *Improved accuracy in the estimation of the tearing mode stability parameters using 2D ECEI data in KSTAR*. Nuclear Fusion, 54(8):083010, 2014.

The work in this thesis has been presented at the following conferences:

- Institute of Physics plasma physics conference 2014 - research content from chapter 4 (oral presentation)
- American Physical Society plasma physics conference 2014 - research content from chapter 5 (poster presentation)

“I think it is much more interesting to live with uncertainty than to live with answers that might be wrong.”

Richard Feynman

Chapter 1

Introduction

1.1 Fusion as an energy source

1.1.1 The demand for renewable energy sources

At present over 80% of global energy demand is met by burning fossil fuels, and this demand is projected to grow by over 40% by 2040 [1, 2]. Meeting this increase whilst simultaneously honouring international commitments to reduce carbon emissions poses a significant challenge. The only available solution is to greatly reduce fossil fuel consumption and invest heavily in carbon-neutral energy production on a global scale. At the very least, crude oil and natural gas must be phased out of the fuel mix before reserves are depleted, which by current estimates will last around 50 years [3]. This is likely an overestimate of the time available in which to address these problems for two reasons. Firstly, the impact of climate change may dictate that the total carbon emissions resulting from the burning of all remaining fossil fuels are completely unacceptable. Secondly, serious consequences for the global energy market will set in not when fossil fuels are exhausted completely, but when available supply can no longer meet demand.

Purely renewable energy sources such as wind, hydro and solar are not sufficient to meet energy demand alone, mostly due to a combination of limited availability and low

Chapter 1. Introduction

power output [4]. These renewables will still play an important role in our transition to carbon-neutral energy production, but they must be supplemented by other sources. Nuclear fission is a strong option to help bridge the supply gap, having no carbon emissions and providing high, consistent power production. The total available fuel for nuclear fission (including estimates of undiscovered resources) is expected to last roughly 230 years at the current rate of consumption. However we see in figure 1.1 that fission accounts for only 5% of global energy supply. For fission to play a substantial role in replacing fossil fuels, this fraction must be brought up to 30-50%. This is a large increase but not infeasible - note that France, for example, currently generates around 75% of its total electricity supply through fission. However, greatly increasing global fission energy production would bring down the lifetime of nuclear fuel reserves significantly making fission a relatively short-term solution. It may be possible to extend the lifetime of these reserves by making use of alternative fuels such as Thorium, or through fast-breeder reactors but these technologies are yet to be widely adopted. It

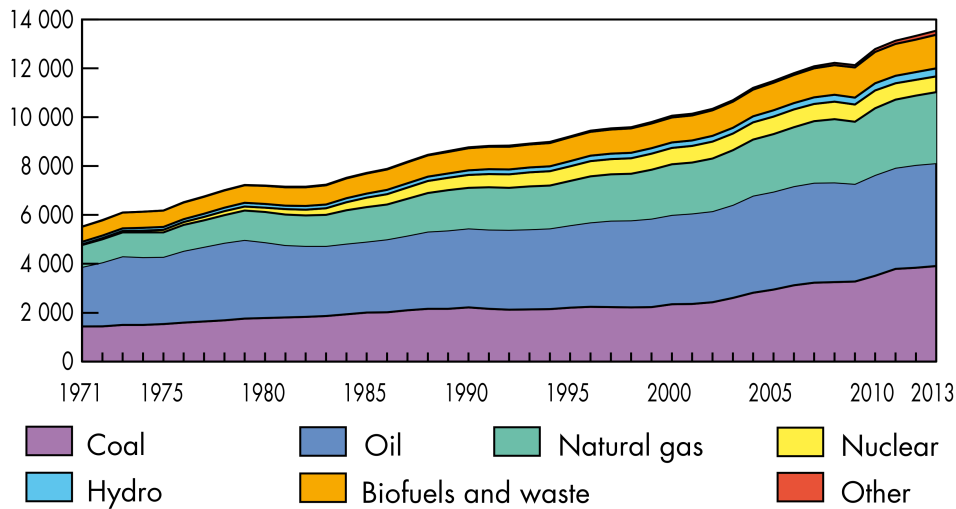


Figure 1.1: Contributions of various energy sources toward total global energy expenditure over a ~ 40 year period. [1]

is also likely that such a drastic increase in fission power would be politically difficult to accomplish. Fission has long suffered from poor public perception, which has recently declined further on account of the Fukushima reactor nuclear incident in 2011. Only days after Fukushima, large anti-nuclear energy protests led to the German government pledging to shut down all 16 of the country's fission plants by 2022, which at the time generated around 25% of Germany's electricity [5, 6].

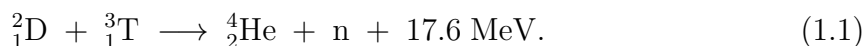
Nuclear fusion is a potential source of carbon-free energy that is well-suited to take

1.1. Fusion as an energy source over from fission as a long-term solution to the global energy crisis. Although achieving fusion power has proved challenging, incredible progress has been made since research began in the 1950's and this progress continues today with construction of next-step devices such as ITER [7]. We now give a brief overview of nuclear fusion as an energy source.

1.1.2 The Deuterium-Tritium fusion reaction

Nuclear fusion is a process by which two nuclei may fuse together, producing a heavier nucleus and additional products. By undergoing fusion, the system of the two original nuclei transition into a state with lower potential energy, and the potential difference is transferred to the reaction products as kinetic energy. The drop in potential is observed as an equivalent (through $E = m_0c^2$) reduction in the rest-mass of the system.

For fusion to occur, two nuclei must be brought into close proximity (within tens of femtometres) such that they interact via the strong nuclear force. This requires that the reactants have sufficient relative collision velocity to overcome their mutual coulomb repulsion. The most promising fusion reaction for energy production is that between the two heavy isotopes of Hydrogen - Dueterium and Tritium:



This is the referred to as the 'DT' reaction and is the focus of most fusion energy research due its very high reactivity as shown in figure 1.2. Dueterium is a naturally-occurring isotope and is most commonly harvested from seawater. Roughly one in every 6400 hydrogen atoms in earth's oceans is Dueterium, so although purification is required the supply of Deuterium is for practical purposes unlimited. Tritium is an unstable isotope which undergoes beta decay with a half-life of 12.3 years, and as such does not occur naturally on earth in useful quantities. Any tritium to be used as fusion

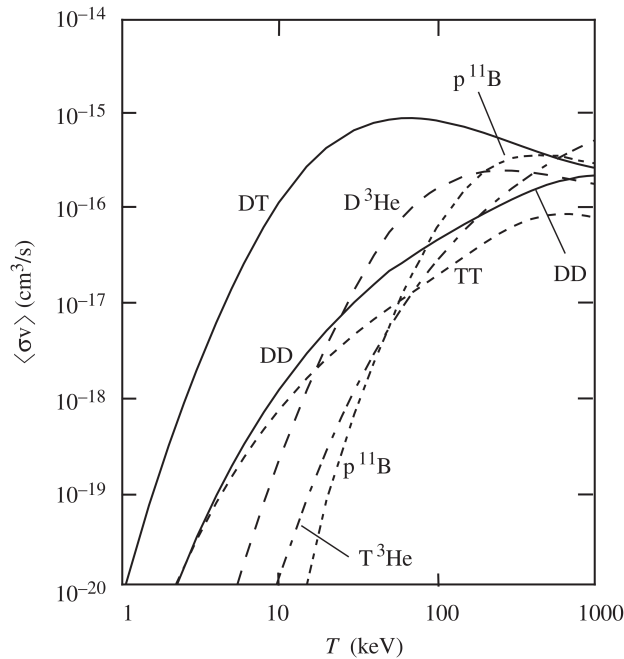


Figure 1.2: Plot of the reactivity $\langle\sigma v\rangle$ for various nuclear fusion reactions as a function of temperature. [8]

fuel must therefore be produced artificially, and currently the most promising approach is neutron-activation of Lithium-6 where



Most fusion energy schemes aim to make use of the neutron produced in the DT reaction to activate Lithium, which then produces more Tritium to be used as fuel. Assuming this process is sufficient to supply all required tritium, the total fuel reserves of nuclear fusion are effectively dictated by the availability of Lithium. Easily-accessible land-based lithium resources are estimated to last over one thousand years assuming fusion were used to generate a significant fraction of global energy, and extraction of Lithium from seawater could extend this lifetime to over a million years [9].

1.1.3 Magnetic confinement fusion

The two basic challenges of fusion energy production are the following: firstly, we must heat the DT fuel mixture to high enough temperatures that fusion reactions are occurring at an acceptable rate, and secondly the fuel must be confined in this state for

1.2. Tokamak physics experiments

sufficient time that we may extract useful amounts of energy from the process. Referring again to figure 1.2 we see that the reactivity of DT increases strongly for higher fuel temperatures up to around 70 keV (8×10^8 Kelvin) where it peaks. The extreme temperatures required to achieve high reactivity ensure two things: no materials exist which are capable of physically confining the fuel, and the fuel itself must be a plasma.

Magnetic confinement fusion is currently the most promising fusion energy scheme, and exploits the fact that when the DT fuel is in a plasma state, it becomes responsive to electromagnetic fields. In a plasma, the nuclei and electrons in the fuel are no longer bound together and move independent of one another - they are therefore both affected by the Lorentz force

$$\mathbf{F} = q (\mathbf{E} + \mathbf{v} \times \mathbf{B}), \quad (1.3)$$

for particle velocity \mathbf{v} and charge q . The $\mathbf{v} \times \mathbf{B}$ term gives rise to a force which acts perpendicular to both \mathbf{v} and \mathbf{B} , causing charged particles to gyrate around magnetic field lines with the cyclotron frequency $\omega_c = qB/m$ and Larmor radius $r_l = v_{\perp}/\omega_c$. Such a particle can be thought of as being confined to the space surrounding the magnetic field-line which lies at the centre of its orbit. If we were to configure \mathbf{B} such that this field-line formed a closed loop, the particle would be spatially confined in motion both parallel and perpendicular to the field. Confining particles in a ‘closed’ field configuration in this manner is the basic idea which underpins magnetic confinement fusion.

1.2 Tokamak physics experiments

1.2.1 Outline of the tokamak concept

The most widely studied MCF device is the ‘tokamak’ - a toroidal chamber surrounded by coils which produce a magnetic field that forms a closed loop around the interior of the torus. An illustration of the tokamak configuration is shown in figure 1.3. It can be shown that charged particles in a toroidal device whose magnetic field points only in either the toroidal or poloidal direction will ‘drift’ towards the wall of the device, and

Chapter 1. Introduction

are therefore not confined. These particle drifts occur due to either additional forces experienced by the particles (e.g. centripetal force, electric fields) or from gradients in the local magnetic field.

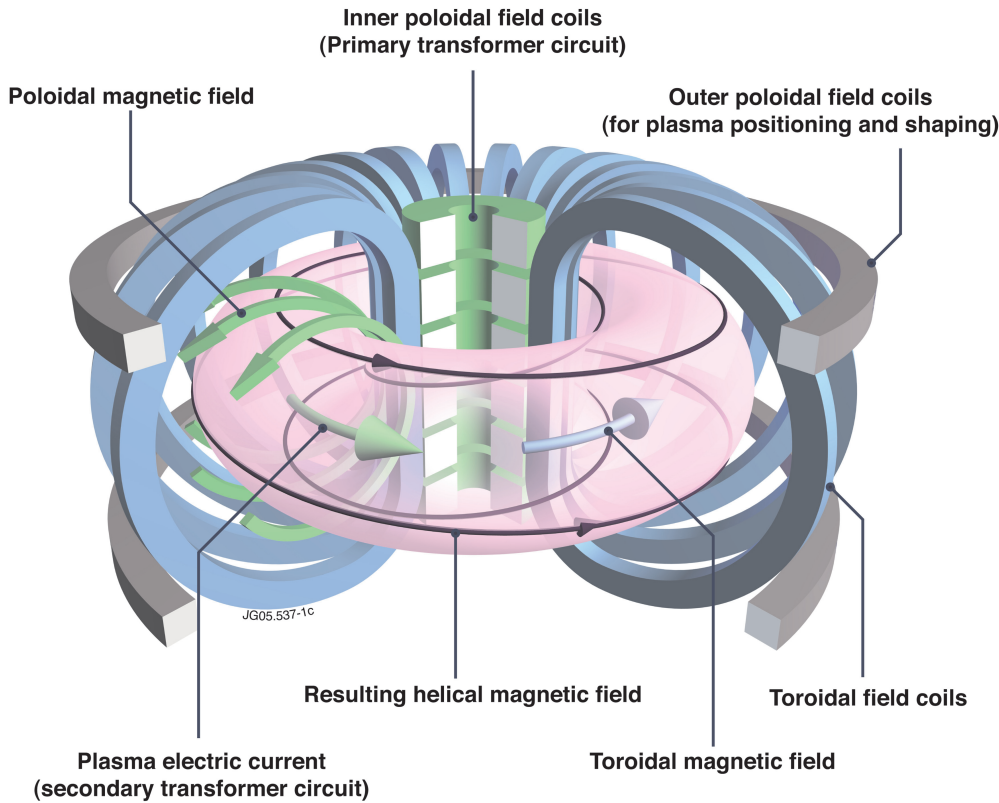


Figure 1.3: Schematic representation of the tokamak configuration. [10]

The solution to this problem is to create a helical magnetic field configuration which is the combination of toroidal *and* poloidal fields. This does not prevent the particle drifts from occurring altogether, but instead periodically reverses their direction such that the time-average of the drift motion is zero [11]. The defining feature of the tokamak concept is the means by which the required helical field is generated. The toroidal component of the field is generated by current-carrying coils which surround the exterior of the device, whereas the poloidal component is generated by inducing a toroidal current in the plasma confined by the tokamak. This plasma current is driven using a solenoid placed at the central axis of the torus, and has the additional benefit of resistively heating the plasma.

To achieve the conditions necessary for fusion, the core of the plasma must be brought up to high temperature and density. The edge however must be kept at a relatively low density and temperature in order for the plasma-facing device components to survive.

As a consequence strong gradients in temperature and density between the core and edge are unavoidable. These gradients give rise to a variety of mechanisms by which heat and particles are transported away from the core and toward the edge. Although the diffusive transport we would naively expect is indeed present, energy transport is in fact dominated by plasma turbulence attributed to various micro-instabilities [12]. This turbulent transport significantly degrades the ability of an MCF device to confine energy, and is the primary barrier to achieving fusion conditions.

1.2.2 Progress toward fusion

The ultimate goal of MCF research is improve energy confinement to the point where the self-heating of the plasma due to fusion reactions is greater than the energy losses due to heat and particle transport. This state is known as ‘ignition’, because the energy released by the plasma as it ‘burns’ the DT fuel is sufficient to sustain the burning process. The rate at which the plasma loses energy P_L is quantified in terms of an ‘energy confinement time’ τ_E such that $P_L = W/\tau_E$ where W is the stored energy. For a homogeneous plasma of volume V , temperature T and number density n the stored energy is $W = 3nTV$. The rate at which the plasma gains energy from fusion reactions is $P_\alpha = \frac{1}{4}n^2\langle\sigma v\rangle E_\alpha V$. To achieve ignition we require that $P_\alpha > P_L$, which may be rearranged to give the Lawson criterion

$$n\tau_E > \frac{12T}{\langle\sigma v\rangle E_\alpha}. \quad (1.4)$$

Both τ_E and $\langle\sigma v\rangle$ are functions of temperature, and based on their behaviour the ignition criterion can most easily be met in the range $T = 10 - 25$ keV. Over this range, the reactivity is well approximated as $\langle\sigma v\rangle \approx T^2 \times 1.1 \times 10^{-24}$. Using this approximation in (1.4) and collecting $nT\tau_E$ on LHS leaves only a product of known constants on the RHS, allowing the ignition criterion to be expressed as

$$nT\tau_E > 3 \times 10^{21} \text{ m}^{-3}\text{keVs} \quad (1.5)$$

This makes $nT\tau_E$, which we refer to as the ‘fusion triple product’, a useful metric for the performance of MCF devices because it tells us how ‘far away’ any given device is from achieving plasma ignition. Figure 1.4 shows triple products measured in major tokamak experiments, illustrating the huge progress that has been made towards ignition since research began.

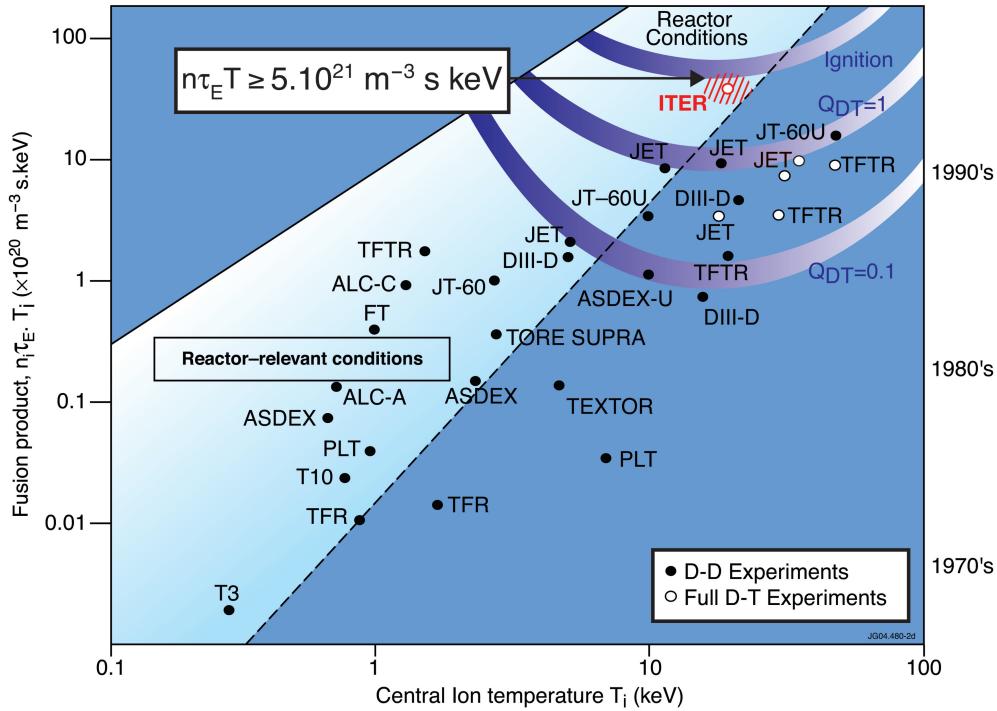


Figure 1.4: The fusion triple-product as measured in various tokamak experiments over the history of MCF research. [10]

1.3 Complexity in magnetic confinement fusion

The physics of magnetised plasmas and magnetic confinement fusion is a rich and complex field. There is, for example, an extreme diversity of scales involved. Micro-instabilities at the Larmor orbit scale which drive energy transport and global magneto-hydrodynamic instabilities which affect the stability of the entire plasma both play crucial roles, and we must understand the physics of both. There exists similarly extreme variation in energy densities, with fully-ionised core plasmas at hundreds of millions of kelvin separated by only a few metres from semi-ionised plasmas interacting with material surfaces. MCF is also very diverse with respect to the disciplines required, and

1.3. Complexity in magnetic confinement fusion

brings together electromagnetism, plasma kinetics, fluid dynamics, turbulence theory, plasma chemistry, atomic physics, materials science and more.

This huge variety of physical conditions and phenomena, all of which are important, require a similar variety of diagnostic equipment and techniques in order to study and understand the physics at work. This is well illustrated by figure 1.5 which highlights the major diagnostic systems on the JET tokamak.

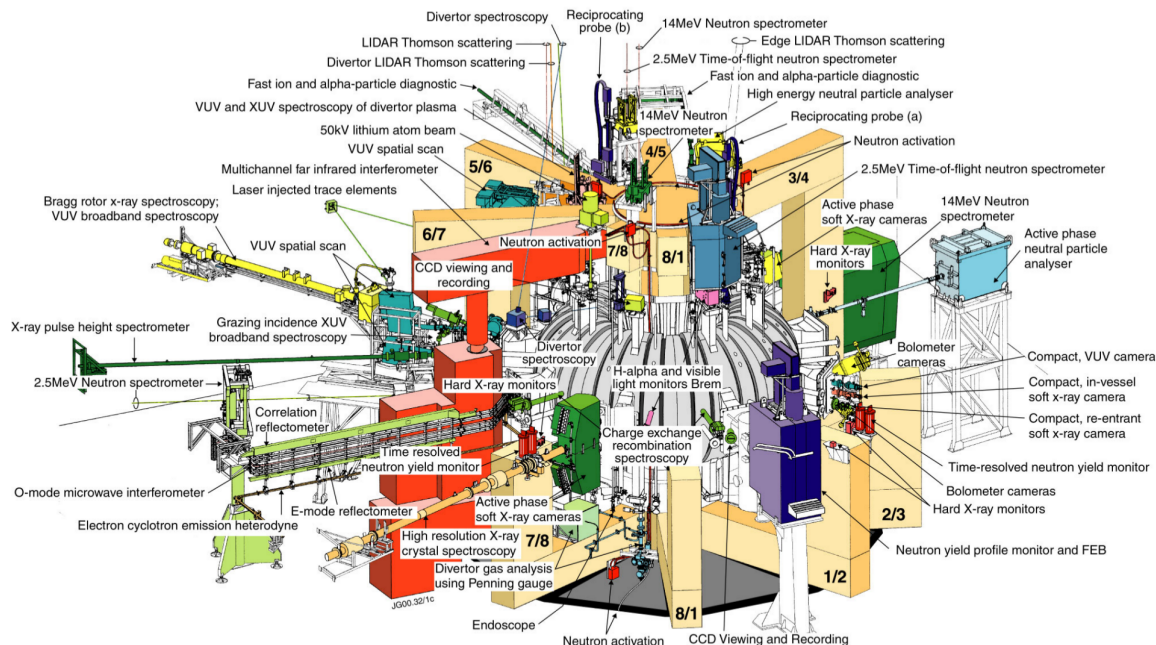


Figure 1.5: Schematic of the JET tokamak with many (but not all) of the diagnostic systems labelled. [13]

In most cases the output of a diagnostic does not vary straightforwardly with a single parameter. Instead, the data often depend on multiple physical parameters simultaneously as well as a variety of diagnostic calibration factors. Consequently, extracting reliable information regarding a single parameter from the data can be challenging. Conventional data analysis techniques can provide estimates of these parameters, but generally fail to properly account for experimental uncertainties or how variation in one parameter affects our information regarding the others.

Bayesian probability theory offers a solution to these problems. It can aide in the analysis of individual diagnostics by using probabilities to rigorously quantify to what extent we believe any possible value of a parameter is the true value given the experimental data. Additionally, it provides a powerful framework for combining information from

Chapter 1. Introduction

multiple diagnostic sources, an approach referred to as ‘multi-diagnostic inference’ or ‘integrated data analysis’. It allows data from many sources, each of which individually may carry very weak information regarding a certain parameter, to be combined to yield strong information about said parameter. Bayesian probability theory has already been successfully applied to fusion data analysis in several cases [14, 15, 16] and is growing in popularity within the field.

1.3.1 This thesis

In this thesis we investigate various ways in which Bayesian probability theory may be applied to data analysis problems within magnetic confinement fusion. In chapter 2 we give an introduction to Bayesian probability theory and present examples of how it can be used to infer desired parameters from experimental data.

In chapter 3 we discuss computational challenges associated with Bayesian methods, and investigate techniques for overcoming some of these difficulties. In particular we present a new approach to efficiently characterising multi-dimensional posterior distributions. This is achieved through an algorithm, the details of which are discussed, that makes decisions regarding which regions of probability space contain useful information and evaluates only those areas.

In chapter 4 Bayesian probability theory is applied to the discrete Fourier transform of an arbitrary signal containing unknown noise. We show that a probabilistic noise-correction can be made by adjusting the magnitude of the Fourier coefficients based on their measured values. This correction requires the solution of an interesting inverse problem which arises naturally during the analysis. Several approaches to obtaining approximate solutions to the problem are developed and then tested using example data. Finally the correction technique is used to reduce the noise level in KSTAR electron-cyclotron emission imaging data. This data was used as part of a collaboration between the York Plasma Institute, POSTECH university and NFRI, the results from which are published in [17] and included as an appendix to this thesis. My contribution to this publication was the development of software to forward-model measured

1.3. Complexity in magnetic confinement fusion ECEI channel data, and the design of the stochastic fitting approach used to estimate model parameters. This work was the first example of using 2D ECEI measurements, which are capable of fully characterising the temperature perturbations associated with neoclassical tearing modes, to study heat transport around magnetic islands and the impact this has on their stability.

In chapter 5 we discuss the inference of physics model parameters using the DIII-D charge-exchange recombination spectroscopy system. In particular the limits of the instrument with regard to characterising fast flow velocity fluctuations are investigated. A Bayesian network approach is used to construct a model for the observed CER spectrum, which in turn is used to construct the posterior for the model parameters. The behaviour of the model under time-varying temperature, density and flow is assessed both analytically and numerically. Finally, a summary of the thesis and conclusions are presented in chapter 6.

Chapter 2

Bayesian inference in physics data analysis

When conducting a physics experiment our objective is typically to learn something about a physical parameter of interest. This process always requires two elements - experimental observations and a model to describe those data. Conventional approaches to data analysis usually seek to find a ‘best match’ between models and observations, and take the values of the parameters resulting from this matching to be measurements of those quantities plus or minus some estimate of the uncertainty.

Bayesian probability theory offers an alternative approach to data analysis which holds many advantages over conventional techniques. Rather than treating model parameters as fixed quantities giving rise to possible observations, the Bayesian approach sees the parameters as fundamentally uncertain, being the distribution of possible causes which could have given rise to the fixed experimental observations.

In this chapter we give an introduction to Bayesian probability theory, demonstrate how it may be applied to data analysis problems and discuss the advantages offered over conventional approaches.

2.1 Introduction to Bayesian probability theory

Given a model for a physical system and assumptions about the state of that system, we may derive the expected results of any experiments conducted on it. This is the ‘forward problem’, and is an example of *deductive* logic, where by starting with a known cause we may deduce the outcomes of that cause with certainty.

Analysis of data from experiments is generally an ‘inverse’ problem where *inductive* logic is needed. This is the process of starting with observed outcomes (i.e. data) and inferring the possible causes of those outcomes. Unlike deductive logic, the conclusions of inductive logic and inverse problems are not certain - we therefore require a system for quantifying how much we believe any of the possible causes are the true cause given our observed outcomes. Physicist Richard Cox showed that for any such system to be logically consistent, it *must* follow the rules of probability theory [18].

Bayesian probability theory is a framework for inductive logical reasoning through probabilities, making it perfectly suited to the problems of data analysis. It is named for Thomas Bayes who is credited as having founded the field, but Bayes’ ideas were developed much further by Pierre-Simon Laplace in the early nineteenth century. Laplace used his formulation of Bayesian probability theory to solve problems in a variety of fields including medical statistics and celestial mechanics [19].

2.1.1 The Bayesian view of probability

Modern statistical theory (developed by Pearson, Fischer and others from the late nineteenth century onwards) generally interprets the probability associated with a particular value of a variable as a ‘frequency’ [20, 21]. The supposition is that if said variable were the outcome of some experimental trial, and we were able to repeat that experiment infinitely many times, all possible values of the variable would arise with a frequency set by their associated probability.

This is at odds with the view of early pioneers of probabilistic inference like Bayes and Laplace, for whom probabilities represented a degree of belief in, or a degree of certainty regarding a particular value of a variable. This ‘Bayesian’ interpretation of probability is more widely applicable than the ‘frequentist’ view of modern statistics, which rejected the Bayesian view believing it to be conceptually too nebulous.

In the last few decades however, Bayesian methods have grown in popularity as scientists and engineers have rediscovered their usefulness, especially when combined with modern computational techniques. This chapter serves as an introduction to the use of Bayesian inference in physics data analysis. In this section we review some fundamental results of probability theory which form the tools of Bayesian analysis.

2.1.2 Notation

The notation of Bayesian probability theory is used throughout this thesis, so a brief review is given here. We denote the ‘probability of A ’ as $P(A)$. In the context of physics data analysis, A will generally be a continuously-valued variable (e.g. the temperature of a plasma, the wavelength of a photon, ect.), making $P(A)$ a continuous probability distribution.

A comma is used to represent joint probabilities, such that $P(A, B)$ is the probability of A and B . The $|$ symbol indicates that the probability of one variable is *conditional* on another so that $P(A|B)$ is the probability of A given B . For example, $P(A, B|C, D)$ represents the ‘probability of A and B given C and D ’.

2.1.3 Fundamentals of probability: the sum and product rules

The first of two fundamental rules of probability we will discuss is the *product rule*, which states that

$$P(A, B|I) = P(A|B, I)P(B|I). \quad (2.1)$$

Throughout this section we will follow Sivia's suggestion [19] of assuming variables are conditional on some unspecified information I , so that these expressions are given in their most general form. The significance of the product rule is that it allows us to construct joint distributions of multiple variables from the product of distributions of a single variable.

The *sum rule* states that the sum of the probabilities associated with all possible values of a variable must equal one. For boolean variables, e.g. if A were a statement that could be either true or false, this implies that

$$P(A|I) + P(\bar{A}|I) = 1. \quad (2.2)$$

Generalising this concept to continuous variables yields

$$\int_{-\infty}^{+\infty} P(A|I) \, dA = 1, \quad (2.3)$$

which we recognise as the *normalisation* property of continuous probability distributions. The sum and product rules are the basis for the algebra of probabilities and we will make extensive use of them.

2.1.4 Bayes' Theorem

In (2.1) the product rule is used to construct the probability of 'A and B given I'. Logical consistency requires that this is equivalent to the probability of 'B and A given I', i.e. that $P(A, B|I) \equiv P(B, A|I)$. We may therefore write a transposed version of the product rule where

$$P(A, B|I) = P(B|A, I)P(A|I). \quad (2.4)$$

Comparing (2.1) and (2.4) we see that

$$P(B|A, I)P(A|I) = P(A|B, I)P(B|I). \quad (2.5)$$

This equality is *Bayes' theorem*, and much of this chapter will be dedicated to discussing its applications and importance. Bayes' theorem is most commonly expressed in a rearranged form of (2.5) where we solve for $P(B|A, I)$:

$$P(B|A, I) = \frac{P(A|B, I)P(B|I)}{P(A|I)}. \quad (2.6)$$

Here we can more easily see that Bayes' theorem can be used to switch the positions of two variables which are on opposite sides of the conditioning symbol |.

2.1.5 Marginalisation

Consider the integral of the product rule in (2.1) over all values of A :

$$\int_{-\infty}^{+\infty} P(A, B|I) \, dA = P(B|I) \int_{-\infty}^{+\infty} P(A|B, I) \, dA. \quad (2.7)$$

The normalisation condition in (2.3) dictates that the integral on the RHS of (2.7) must be equal to one, and as such

$$P(B|I) = \int_{-\infty}^{+\infty} P(A, B|I) \, dA. \quad (2.8)$$

This result is known as *marginalisation*. Given a joint distribution of multiple variables, it allows us to remove the dependence on any number of those variables through integration as shown above. We will demonstrate later that marginalisation is particularly useful in the case of model parameter estimation.

2.1.6 Conditional independence

If $P(A|B, I) = P(A|I)$, we say that A and B are *conditionally independent* given I . It may seem initially that this only implies that A is independent of B given I and not vice-versa, but consider again the form of Bayes' theorem given in (2.5):

$$P(A|B, I)P(B|I) = P(B|A, I)P(A|I). \quad (2.9)$$

If we make the substitution that $P(A|B, I) = P(A|I)$ we obtain

$$P(A|I)P(B|I) = P(B|A, I)P(A|I) \implies P(B|I) = P(B|A, I), \quad (2.10)$$

and as such

$$P(A|B, I) = P(A|I) \iff P(B|A, I) = P(B|I). \quad (2.11)$$

An important consequence of conditional independence is that the product rule becomes

$$P(A, B|I) = P(A|I)P(B|I). \quad (2.12)$$

This result may be generalised to an arbitrary number of variables. Consider a set of n variables $\{x_i\}$ - the joint distribution $P(x_1, x_2, \dots, x_n|I)$ is the product of the individual $P(x_i|I)$ if and only if each of the x_i is conditionally independent of all other variables in the set. This can be expressed mathematically as

$$P(x_1, x_2, \dots, x_n|I) = \prod_{i=1}^n P(x_i|I) \iff P(x_i|x_j, I) = P(x_i|I) \quad \forall i \neq j. \quad (2.13)$$

This result is particularly useful in data analysis, as often we want to generate the joint distribution of a large number of independent measurements, and therefore may do so by finding the product of the distributions for each individual measurement.

2.2 Bayes theorem example: decay of an excited state

Understanding the applications of Bayesian inference to data analysis is, in our opinion, best gained through physically motivated examples. The rest of this chapter will be dedicated to discussing several such examples, the first of which focusses on the use of Bayes' theorem.

Consider a thought experiment where we wish to measure the rate λ at which an electron decays from some excited state in an atom to one of lower energy. We will

2.2. Bayes theorem example: decay of an excited state
assume (for now) that we are able to measure the time between excitation and decay exactly with no uncertainty.

This process is not deterministic, and λ represents the probability per unit time that the state will decay. It can be shown that a constant λ implies an exponential distribution of measured state lifetimes, such that the chance that the state takes a time t to decay for a given λ is

$$P(t|\lambda) = \lambda \exp[-\lambda t]. \quad (2.14)$$

Given some number of independent measurements of t , what is the best approach to determining λ ?

2.2.1 Potential ‘frequentist’ approaches to estimating λ

In order to provide contrast for the Bayesian solution to this problem which we will subsequently discuss, it is useful to briefly mention some conventional ways a physicist might approach this task.

If a relatively large number of measurements of t are available (a few hundred or more), $P(t|\lambda)$ could be estimated by taking a histogram of the set of t values. Standard curve-fitting techniques may then be used to fit (2.14) to the data yielding an estimate of λ .

We might also note that $E[t] = \lambda^{-1}$, and estimate λ by finding the mean of all our time measurements and calculating its reciprocal.

2.2.2 Inference from a single time measurement

Initially we will examine the case where we have only a single measurement of the decay time t . Based on the non-Bayesian approaches discussed above, one might expect that little may be learned from one data point as taking an average or a histogram of the data is no longer possible - in fact Bayes' theorem provides us with an exact solution.

$P(t|\lambda)$ is given by our physics model in (2.14), however as our objective is to determine λ , the probability we actually want is that of λ *given* our value for t , i.e. $P(\lambda|t)$. By referring to Bayes' theorem in (2.6) we see that we may write $P(\lambda|t)$ as

$$P(\lambda|t) = \frac{P(t|\lambda)P(\lambda)}{P(t)}. \quad (2.15)$$

Understanding the meaning of each term in this expression is crucial, so we will now take some time to discuss them individually.

Firstly, let us examine $P(\lambda)$ - from notation alone we know that this is a probability distribution for λ , but crucially one which is *not* conditional on our experimental data t . This point is key to understanding the use of Bayes' theorem, so we emphasise - $P(\lambda)$ is the probability associated with (and hence our degree of certainty regarding) a particular value of λ irrespective of the experimental data. $P(\lambda)$ therefore represents our state of knowledge regarding λ *before* conducting the experiment, and accordingly is called the *prior distribution*. Conversely $P(\lambda|t)$ is our state of knowledge regarding λ *after* we have obtained additional information from the experiment, so is referred to as the *posterior distribution*. By allowing us to move from the prior to the posterior, Bayes' theorem provides a means to update our knowledge in light of new information.

In this example, we have no prior knowledge of λ save that we know $\lambda > 0$. Given this lack of information we might expect that any particular value of λ is no more or less likely than any other, and therefore would regard all possible values as being equally probable. Mathematically, this results in a $P(\lambda)$ which is constant for all $\lambda > 0$. This constant form of $P(\lambda)$ is called a 'flat' or 'uninformative' prior because it effectively carries no information - it also therefore has no dependence on λ .

2.2. Bayes theorem example: decay of an excited state

It may appear that taking $P(\lambda)$ to be flat is the only option which is not in some way ‘biased’ given that we have no prior information, but in fact the choice is not so straightforward. Consider that we may easily re-parametrise the problem in terms of the average lifetime $\tau = \lambda^{-1}$. Clearly, we also have no information regarding τ , so if a flat prior were the ‘natural’ choice in such a case we would also choose $P(\tau)$ to be flat. The problem now becomes clear - it is not possible to simultaneously assume that all values of both λ and τ are equally probable. If we take $P(\lambda)$ to be flat, then it must be the case that $P(\tau) \propto \tau^{-1}$ and vice-versa. This does not suggest that use of a flat prior is never appropriate, just that even when using a flat prior we are still making an assumption of some type. A common alternative to the flat prior is the Jeffreys prior, which remains invariant under re-parametrisation of variables such as that described above [22]. We will however, for the sake of simplicity, take $P(\lambda)$ to be flat for this example.

$P(t|\lambda)$ represents the information we have gained from our experiment and is called the *likelihood*. For a general case the likelihood includes all sources of uncertainty involved in obtaining the measurements. These may arise from stochastic physical processes (e.g. variation in the number of photons emitted by a plasma in a given time) or from limitations in our instrumentation (e.g. the point-spread function of a spectrometer, dark current from a CCD, ect). The likelihood is also typically a function of some physics model which predicts the observations and depends on some physical parameters we are interested in. The process of building the likelihood for an experiment will be discussed later in this chapter.

In many applications of Bayes’ theorem (including this example) $P(t)$ is essentially a normalisation factor and therefore receives little attention. However there are certain cases, in particular model selection, where $P(t)$ becomes important. For this reason it is sometimes referred to as the *model evidence*. Generally $P(t)$ may be determined using the normalisation condition in (2.3) - integrating Bayes’ theorem in (2.15) over all λ we see that

$$\int_0^\infty P(\lambda|t) d\lambda = \frac{1}{P(t)} \int_0^\infty P(t|\lambda)P(\lambda) d\lambda = 1, \quad (2.16)$$

which solved for $P(t)$ yields

$$P(t) = \int_0^{\infty} P(t|\lambda)P(\lambda) d\lambda. \quad (2.17)$$

In this example however, we have explicitly stated that $P(\lambda)$ is a *flat* prior and so has no λ dependence. This allows us to move $P(\lambda)$ outside the integral in (2.17) and write

$$\frac{P(t)}{P(\lambda)} = \int_0^{\infty} P(t|\lambda) d\lambda = \int_0^{\infty} \lambda \exp[-\lambda t] d\lambda = \frac{1}{t^2}. \quad (2.18)$$

The posterior distribution can now be obtained by substitution of the above result back into (2.15), which gives

$$P(\lambda|t) = \lambda t^2 \exp[-\lambda t]. \quad (2.19)$$

We now have a probability density for, and therefore a degree of belief in every possible value of λ based on the information provided by our value for t . For the $t = 1$ case plotted in figure 2.1 it can be shown numerically that the shortest interval which contains a total probability of 0.95 is $[0.042, 4.76]$ - we may therefore assert that $0.042 < \lambda < 4.76$ with 95% probability.

2.2.3 Likelihood of a dataset: multiple time measurements

We can now examine the more general case where we have n separate measurements of t rather than just one. Previously, our goal was to obtain the probability of λ given one measurement of t , i.e. $P(\lambda|t)$. Now we want the probability of λ given *all* n measurements of t , which we may write as $P(\lambda|t_1, t_2, \dots, t_n)$.

Just as in the single-measurement case, $P(\lambda|t_1, t_2, \dots, t_n)$ may be expressed using Bayes' theorem as

$$P(\lambda|t_1, t_2, \dots, t_n) = \frac{P(t_1, t_2, \dots, t_n|\lambda)P(\lambda)}{P(t_1, t_2, \dots, t_n)}. \quad (2.20)$$

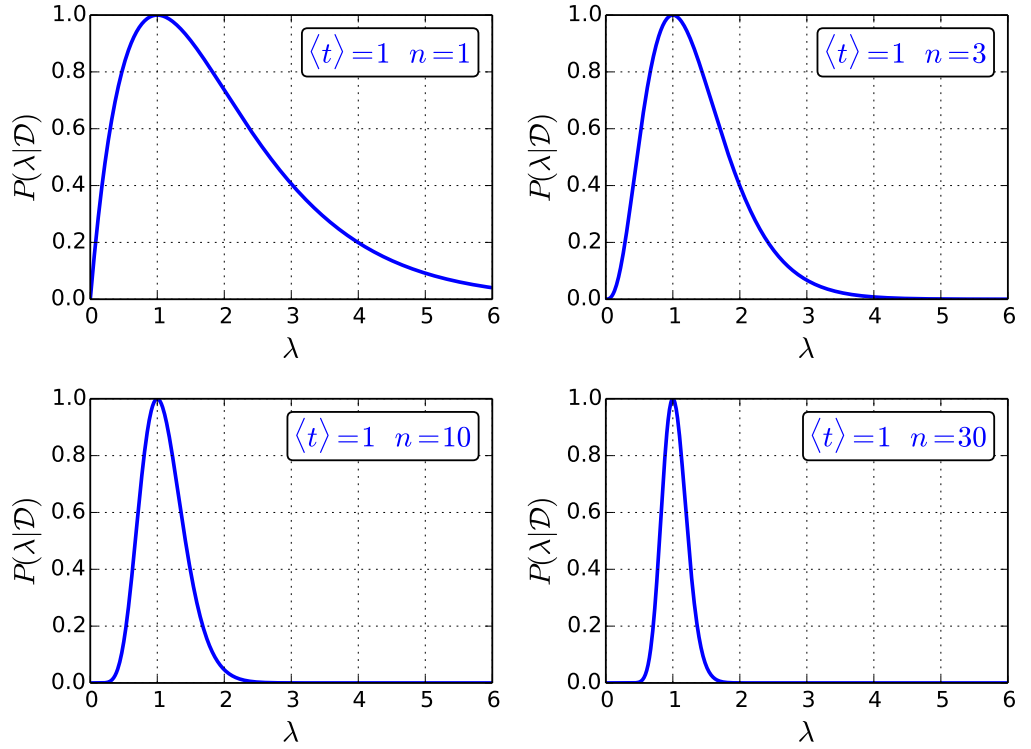


Figure 2.1: Plots of (2.26) versus the decay rate λ for $\langle t \rangle = 1$ and various n . The $n = 1$ case in the top-left is therefore also a plot of (2.19) where $t = 1$. Here we follow the common practice of scaling probability distributions to have a maximum of 1 for the purposes of plotting, as absolute density values are generally not useful to the reader.

Again taking $P(\lambda)$ to be a flat prior (because we have no information regarding λ prior to the experiment) allows $P(\lambda)/P(t_1, t_2, \dots, t_n)$ to be determined through normalisation (as shown in (2.18)) such that

$$P(\lambda|t_1, t_2, \dots, t_n) = \frac{P(t_1, t_2, \dots, t_n|\lambda)}{\int_0^\infty P(t_1, t_2, \dots, t_n|\lambda) d\lambda}. \quad (2.21)$$

We therefore need only determine $P(t_1, t_2, \dots, t_n|\lambda)$ to obtain $P(\lambda|t_1, t_2, \dots, t_n)$. As we have stated that the set of time measurements $\{t_i\}$ are independent of each other (given λ), we may use the result in (2.13) to write

$$P(t_1, t_2, \dots, t_n|\lambda) = \prod_{i=1}^n P(t_i|\lambda) = \lambda^n \exp \left[-\lambda \sum_{i=1}^n t_i \right]. \quad (2.22)$$

Joint distributions of a large number measurements often arise in Bayesian data analysis, and as such it is common practice to represent the set of all data with some symbol - in this thesis we use \mathcal{D} such that $P(t_1, t_2, \dots, t_n|\lambda) \equiv P(\mathcal{D}|\lambda)$. In this example, it is

also convenient to write (2.22) in terms of the average time

$$\langle t \rangle = \frac{1}{n} \sum_{i=1}^n t_i, \quad (2.23)$$

such that (2.22) now simplifies to

$$P(\mathcal{D}|\lambda) = \lambda^n \exp[-n\lambda\langle t \rangle]. \quad (2.24)$$

All that remains is to find the integral of $P(\mathcal{D}|\lambda)$ as is required by (2.21):

$$\frac{P(\mathcal{D})}{P(\lambda)} = \int_0^\infty \lambda^n \exp[-n\lambda\langle t \rangle] d\lambda = \frac{n!}{(n\langle t \rangle)^{n+1}}. \quad (2.25)$$

Substitution of the above result into (2.21) yields our solution

$$P(\mathcal{D}|\lambda) = \frac{\lambda^n}{n!} (n\langle t \rangle)^{n+1} \exp[-n\lambda\langle t \rangle]. \quad (2.26)$$

Plots of (2.26) for various n are shown in figure 2.1. As one would expect, we see that increasing n for a fixed $\langle t \rangle$ narrows $P(\lambda|\mathcal{D})$, corresponding to an improvement in our knowledge of λ as a result of the inclusion of additional experimental data. Additionally, making the substitution of $n = 1$ in (2.26) we recover our expression for $P(\lambda|t)$ (the single-measurement case) in (2.19).

2.2.4 Approaching the frequentist limit

We see from figure 2.1 that the maximum of $P(\lambda|\mathcal{D})$ occurs at $\lambda = 1$ irrespective of n . In fact it can be easily shown via differentiation that the rate which maximises the posterior is

$$\lambda_0 = \arg \max_{\lambda} P(\lambda|\mathcal{D}) = \langle t \rangle^{-1}, \quad (2.27)$$

indicating that the frequentist approach described in section 2.2.1 yields the mode of the posterior distribution $P(\lambda|\mathcal{D})$. Of course the Bayesian solution given here is preferable, particularly for smaller values of n where the posterior has significant skewness. It is

2.2. Bayes theorem example: decay of an excited state
 informative however to consider what happens in the limit of large n . In this limit, we can make use of Stirling's approximation, which states

$$\frac{n^n}{n!} \sim \frac{1}{\sqrt{2\pi n}} e^n. \quad (2.28)$$

Substitution into the posterior yields

$$P(\lambda|\mathcal{D}) \approx \frac{1}{\lambda_0} \sqrt{\frac{n}{2\pi}} \left(\frac{\lambda}{\lambda_0}\right)^n \exp\left[-\frac{n\lambda}{\lambda_0} + n\right]. \quad (2.29)$$

It is now useful to bring the λ^n/λ_0^n term inside the exponential as follows

$$P(\lambda|\mathcal{D}) \approx \frac{1}{\lambda_0} \sqrt{\frac{n}{2\pi}} \exp\left[-n\left(\frac{\lambda}{\lambda_0} - 1 - \ln\left(\frac{\lambda}{\lambda_0}\right)\right)\right]. \quad (2.30)$$

We may also note from figure 2.1 that for $n \gg 1$ the posterior is very narrow, and as such $\lambda/\lambda_0 \approx 1$ in areas of significant probability density. Accordingly we may replace the logarithm in (2.30) with the following second-order Taylor series

$$\ln\left(\frac{\lambda}{\lambda_0}\right) \approx -1 + \frac{\lambda}{\lambda_0} - \frac{1}{2}\left(\frac{\lambda}{\lambda_0} - 1\right)^2. \quad (2.31)$$

Substitution yields

$$P(\lambda|\mathcal{D}) \approx \frac{1}{\lambda_0} \sqrt{\frac{n}{2\pi}} \exp\left[-n\left(\frac{\lambda}{\lambda_0} - 1 + 1 - \frac{\lambda}{\lambda_0} + \frac{1}{2}\left(\frac{\lambda}{\lambda_0} - 1\right)^2\right)\right], \quad (2.32)$$

which simplifies to

$$P(\lambda|\mathcal{D}) \approx \frac{1}{\lambda_0} \sqrt{\frac{n}{2\pi}} \exp\left[-\frac{n}{2\lambda_0^2} (\lambda - \lambda_0)^2\right]. \quad (2.33)$$

We've shown that in the limit of large n the posterior is actually a normal distribution with standard deviation

$$\sigma = \frac{\lambda_0}{\sqrt{n}}. \quad (2.34)$$

It is not unusual for a problem which is well-constrained by a large amount of data to have a normal posterior, especially for a simple case such as this. This can in some sense be considered a 'frequentist' limit, where a Bayesian and frequentist treatment

of the problem yield essentially the same results.

We've shown here that the Bayesian approach shines in poorly-constrained problems or where data is sparse, but as we'll now discuss it is also very effective in tackling complex problems involving many variables.

2.3 Inference of physics model parameters

In the previous section we examined a case involving only one model parameter (the decay rate λ). However, our physics models often have multiple parameters, and furthermore we may only be interested in inferring a sub-set of those parameters. For example if a model contains a background offset or line, typically we are not interested in the values of those background parameters; they are only present because they are necessary for the model to properly reproduce the observations.

Bayesian inference offers an excellent solution to the problem of model parameter estimation. Through a combination of Bayes' theorem and marginalisation we are able to obtain a distribution for only the parameters we do wish to infer by integrating over those we do not. In this section we demonstrate this procedure through the use of another example.

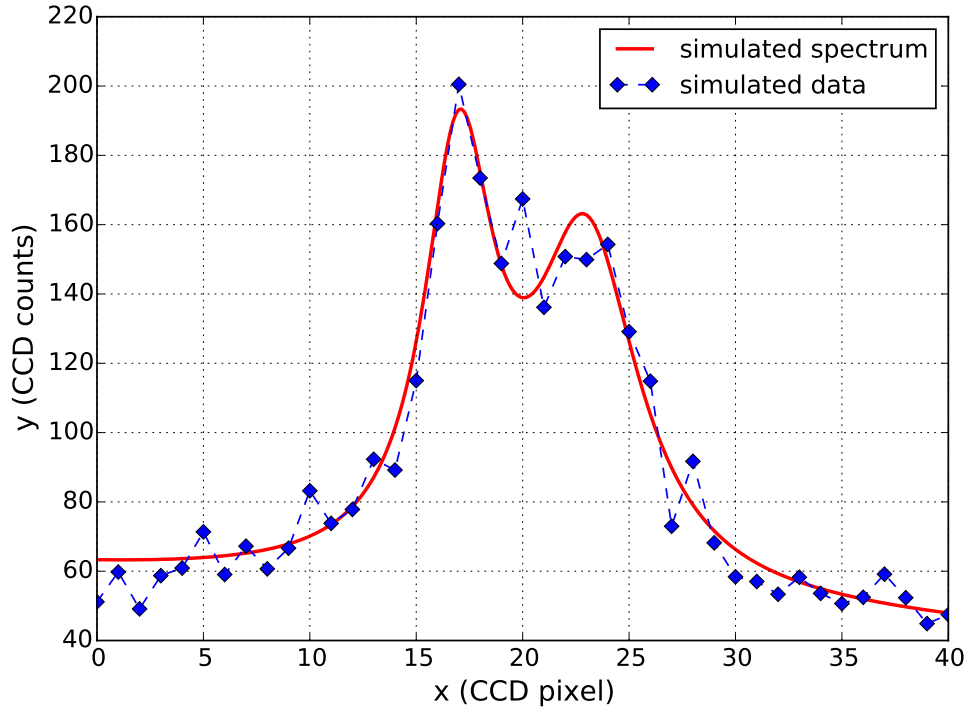
2.3.1 Example: Spectroscopy data analysis

Consider a thought experiment where a spectrometer-CCD system is being used to capture the emission spectrum of a low-temperature plasma. Suppose that we are particularly interested in two closely spaced spectral lines, and in the vicinity of these lines the spectrum is given by

$$S(x, \theta) = \frac{A_1}{1 + \left(\frac{x-c_1}{w_1}\right)^2} + \frac{A_2}{1 + \left(\frac{x-c_2}{w_2}\right)^2} + bx + d, \quad (2.35)$$

Table 2.1: Values used to generate the simulated data shown in figure 2.2.

A_1	A_2	w_1	w_2	c_1	c_2	b	d
120	100	2	3	17	23	60	-0.4

**Figure 2.2:** Plot of the simulated data to be analysed in this example and the spectrum from which it was generated.

where x is the CCD pixel coordinate. It is common practice to represent the set of all parameters in a model with the vector $\underline{\theta}$ (seen as an argument of $S(x, \underline{\theta})$ above). Here we will assume the centre of the lines (c_1 and c_2) are known constants, and as such our parameter vector is $\underline{\theta} = [A_1, A_2, w_1, w_2, b, d]$.

To demonstrate the analysis procedure, a set of simulated data was generated using (2.35). First, a simulated spectrum was produced by calculating $S(x, \underline{\theta})$ using the parameter values given in table 2.1. The simulated data were then generated by assuming the measured values were Poisson distributed with the simulated spectrum serving as the expected counts. Both the simulated spectrum and dataset are shown in figure 2.2.

In section 2.2 we obtained the distribution of our only physics parameter λ given the experimental data. Initially we will seek to do the same here, but as we now have multiple model parameters we require the joint distribution of the parameters $\underline{\theta}$ given the data \mathcal{D} .

2.3.2 The model parameter posterior distribution $P(\underline{\theta}|\mathcal{D})$

Making use of Bayes' theorem we may write the model parameter posterior as

$$P(\underline{\theta}|\mathcal{D}) = \frac{P(\mathcal{D}|\underline{\theta})P(\underline{\theta})}{P(\mathcal{D})}. \quad (2.36)$$

As before, we do not have information from previous experiments regarding $\underline{\theta}$, so our choice of prior should reflect that lack of knowledge. Accordingly, we will take $P(\underline{\theta})$ to be flat - a reasonable choice in such a case. We must now construct the likelihood $P(\mathcal{D}|\underline{\theta})$, which is the probability of all available data given the model parameters. Let y_i be the simulated counts measurement from pixel x_i . We know in this case the distribution of y_i is Poisson (because we sampled from Poisson distributions to generate the data), so the probability of y_i given $\underline{\theta}$ is

$$P(y_i|\underline{\theta}) = \frac{(S(x_i, \underline{\theta}))^{y_i}}{y_i!} \exp[-S(x_i, \underline{\theta})]. \quad (2.37)$$

As the $\{y_i\}$ are mutually conditionally independent we may use the result in (2.13) to write the probability of \mathcal{D} (the whole dataset) given the parameters as

$$P(\mathcal{D}|\underline{\theta}) = \prod_{i=1}^n P(y_i|\underline{\theta}) = \exp \left[\sum_{i=1}^n y_i \ln(S(x_i, \underline{\theta})) - S(x_i, \underline{\theta}) - \ln(y_i!) \right]. \quad (2.38)$$

We could at this stage determine $P(\mathcal{D})$ via the following integral:

$$P(\mathcal{D}) = \int_{-\infty}^{+\infty} \cdots \int_{-\infty}^{+\infty} P(\mathcal{D}|\underline{\theta})P(\underline{\theta}) \, d\underline{\theta}, \quad (2.39)$$

however this step is often omitted when conducting real data analysis. This is because in general we only require *relative* values of probability density rather than absolute values in order to draw conclusions from our results. Consequently, $P(\underline{\theta}|\mathcal{D})$ need only be determined up to a normalisation constant. Given that $P(\underline{\theta}|\mathcal{D}) \propto P(\mathcal{D}|\underline{\theta})$ (for a flat prior) we may decline to evaluate the above integral and simply write

$$P(\underline{\theta}|\mathcal{D}) \propto \exp \left[\sum_{i=1}^n y_i \ln(S(x_i, \underline{\theta})) - S(x_i, \underline{\theta}) - \ln(y_i!) \right]. \quad (2.40)$$

Interpreting the posterior can be difficult if there are more than a few parameters. For example, when we determined $P(\lambda|\mathcal{D})$ in section 2.2 we could simply plot the posterior as there was only one parameter. In our current example there are six parameters total, and as there is no useful way to plot a six-dimensional probability distribution an alternative approach is needed.

One option is to obtain a single-value estimate of all parameters by finding the $\underline{\theta}$ which maximises $P(\underline{\theta}|\mathcal{D})$:

$$\hat{\underline{\theta}} = \arg \max_{\underline{\theta}} [P(\underline{\theta}|\mathcal{D})]. \quad (2.41)$$

$\hat{\underline{\theta}}$ is the *maximum a posteriori* estimate (often called the MAP estimate) of the model parameters, and is typically determined using a global optimisation algorithm.

2.3.3 Marginalisation of nuisance parameters

Although we could use the MAP estimate to get a value for each parameter, is often the case that we are only interested in inferring the value of sub-set of the model parameters rather than all of them. We will now split $\underline{\theta}$ into two groups - one we wish to infer which we will call \underline{z} and one we do not which we will call $\underline{\epsilon}$. The distribution we want to obtain is therefore $P(\underline{z}|\mathcal{D})$ rather than $P(\underline{\theta}|\mathcal{D})$. The $\underline{\epsilon}$ are often given the name ‘nuisance parameters’ in the literature, because they are necessary for evaluating the model but we don’t care about their value.

As $P(\underline{\theta}|\mathcal{D}) \equiv P(\underline{z}, \underline{\epsilon}|\mathcal{D})$, we may use marginalisation to remove the dependence of the posterior on $\underline{\epsilon}$ through integration:

$$P(\underline{z}|\mathcal{D}) = \int_{-\infty}^{+\infty} \cdots \int_{-\infty}^{+\infty} P(\underline{z}, \underline{\epsilon}|\mathcal{D}) \, d\underline{\epsilon} \quad (2.42)$$

This technique of marginalising unwanted model parameters is very powerful, and one of the key advantages offered by the Bayesian approach. We may think about the marginalisation procedure as allowing us to give up information regarding the parameters in $\underline{\epsilon}$ in order to improve our information regarding those in \underline{z} .

In the same way we determined a MAP estimate for all parameters in (2.41), we may define a MAP estimate of \underline{z} as

$$\hat{\underline{z}} = \arg \max_{\underline{z}} [P(\underline{z}|\mathcal{D})]. \quad (2.43)$$

We will now discuss an example of applying marginalisation to the simulated spectral data.

2.3.4 Inference of the line widths: $P(w_1, w_2|\mathcal{D})$

Suppose that the objective of our experiment is to determine the widths of the two spectral lines in the data, and we are not interested in the values of the other parameters. Following the procedure described above in section 2.3.3 we can divide the parameters such that $\underline{z} = [w_1, w_2]$ and $\underline{\epsilon} = [A_1, A_2, b, d]$. The posterior for the two widths is then given by

$$P(w_1, w_2|\mathcal{D}) = \int_{-\infty}^{+\infty} \cdots \int_{-\infty}^{+\infty} P(w_1, w_2, \underline{\epsilon}|\mathcal{D}) \, d\underline{\epsilon}. \quad (2.44)$$

$P(w_1, w_2|\mathcal{D})$ was evaluated numerically using the simulated data and the results are summarised in figure 2.3. The MAP estimate for the widths is $w_1 = 2.05$ and $w_2 = 3.29$, and as we would expect, the actual values of $w_1 = 2$ and $w_2 = 3$ lie in the high probability density region (inside the 95% contour) of $P(w_1, w_2|\mathcal{D})$.

It is useful at this point to consider the distributions $P(w_1|\mathcal{D})$ and $P(w_2|\mathcal{D})$ (shown in figure 2.4) which we can obtain by further marginalising $P(w_1, w_2|\mathcal{D})$:

$$P(w_1|\mathcal{D}) = \int_0^{\infty} P(w_1, w_2|\mathcal{D}) \, dw_2, \quad (2.45)$$

$$P(w_2|\mathcal{D}) = \int_0^{\infty} P(w_1, w_2|\mathcal{D}) \, dw_1. \quad (2.46)$$

Given that $P(w_1|\mathcal{D})$ and $P(w_2|\mathcal{D})$ are distributions for the two parameters we are interested in, one might ask “why should we base our conclusions on $P(w_1, w_2|\mathcal{D})$ ”

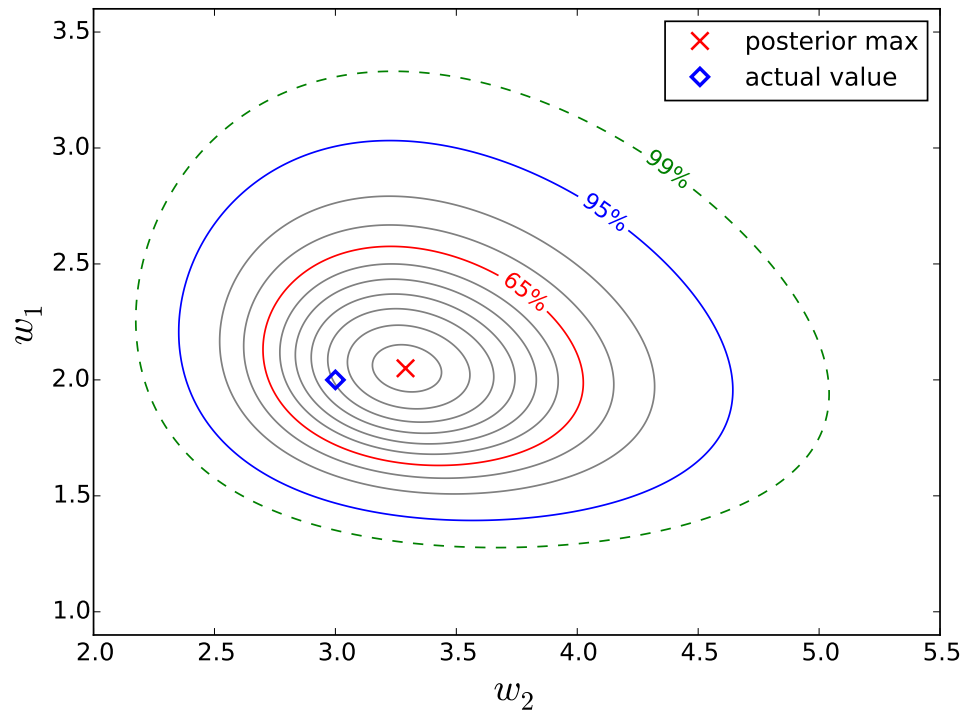


Figure 2.3: A contour plot of $P(w_1, w_2 | \mathcal{D})$ against the peak widths w_1, w_2 using credible regions. Adjacent contours differ in their contained probability by 0.1 (except for the 99% contour). The ‘actual value’ marker indicates the values of w_1 and w_2 from table 2.1.

rather than $P(w_1 | \mathcal{D})$ and $P(w_2 | \mathcal{D})$?”. The answer is that if a conclusion relies on the value of w_1 and w_2 simultaneously, we must use the probability of w_1 and w_2 given the data to inform that conclusion.

2.4 Summary

Gregory [23] gives a concise summary of the merits of Bayesian analysis, saying “It provides an elegantly simple and rational approach for answering, in an optimal way, any scientific question for a given state of information. This contrasts to the recipe or cookbook approach of conventional statistical analysis.” The ‘cookbook approach’ alludes to the fact that conventional statistics has developed separate, and often very varied, strategies for solving any conceivable class of problem. The frequentist approach is therefore to ‘look up’ an appropriate strategy by matching the current problem with one addressed in some statistics reference text.

By contrast, Bayesian probability theory provides a completely general approach to solving problems from first principles in the following way:

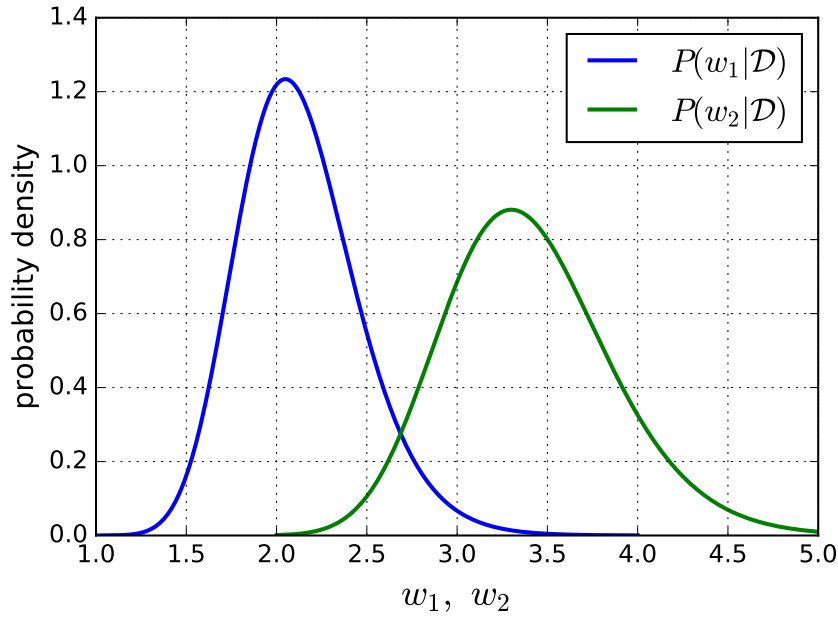


Figure 2.4: Plot of the marginal posterior distributions for the two widths w_1 and w_2 .

- (a) State the problem in terms of the desired posterior distribution.
- (b) Express all prior information regarding the problem as probability distributions.
- (c) Apply the tools described in this chapter (Bayes' theorem, the sum and product rules, marginalisation) to express the desired posterior in terms of known quantities and compute the answer.

In this chapter we've given a brief introduction to Bayesian probability theory and shown through simple examples how it may be used to great effect in data analysis problems. Throughout the rest of this thesis, many of the concepts and techniques discussed here will be used consistently.

Chapter 3

Developing tools for Bayesian analysis

3.1 Introduction

In this chapter we discuss some of the computational challenges associated with Bayesian approaches to data analysis and how they may be dealt with. In particular we investigate improvements to grid-based posterior evaluation in cases where the conventional approach breaks down. Calculation of credible region boundary contour densities is also discussed, along with the use of these boundary contours in presenting inference results.

3.2 Computational challenges of many-parameter inference

In the previous chapter we discussed how multi-dimensional integrals arise naturally in Bayesian data analysis through marginalisation of the nuisance parameters $\underline{\epsilon}$. The dimensionality of the integral which must be evaluated is equal to the number of parameters in $\underline{\epsilon}$, and if this is greater than 5 or 6, conventional approaches to numerical

integration are no longer tractable. In this section we discuss why this is the case, and the conventional solution to the problem.

3.2.1 Limitations of grid-based approaches

When evaluating an integral over many dimensions of a probability distribution we quickly find that grid-based methods become challenging. To understand why, first consider that we must choose the prior for marginalised parameters $P(\underline{\epsilon})$ somewhat conservatively as we do not know *a priori* exactly where in the probability space the regions of significant density are located, or the extent of those regions. In the absence of information from other sources, $P(\underline{\epsilon})$ is often taken as a uniform prior, which sets reasonable upper and lower bounds on the values of the $\underline{\epsilon}$. We will make multiple references during this discussion to the idea of the ‘region of significant density’ - we define this as the region bounded by a contour of constant probability density which encloses *almost* all probability. In other words, the integral of the distribution over the region of significant density is sufficiently close to unity that we would consider the integral to have converged.

The root of the problem is as follows: any hyper-rectangular grid which is sufficiently large to capture all regions of significant density will simultaneously have most of its volume taken up by areas of insignificant density. This may seem counter-intuitive initially, but can be demonstrated clearly by the following example.

Suppose we have a 2D probability space, and the area of significant density is circular with radius R . For discussing shapes with an arbitrary number of dimensions, a filled circle (i.e. one which has area) is referred to as a ‘ball’, or more specifically in this 2D case as a 2-ball. The best-case scenario for evaluating the integral of this probability space on a rectangular grid would be to make the grid the smallest square (or 2-cube) which can contain the 2-ball, i.e. one whose sides are $2R$. If we consider the ‘efficiency’ of this grid to be the ratio of the area of significant density to the total area of the

3.2. Computational challenges of many-parameter inference grid, we find it is $\pi/4 \approx 0.79$. This is fairly good, but consider the volume of the same ball and cube for n dimensions:

$$V_{\text{ball}} = \frac{\pi^{n/2} R^n}{\Gamma(1 + \frac{n}{2})}, \quad V_{\text{cube}} = (2R)^n. \quad (3.1)$$

Their ratio, and therefore the grid efficiency is then

$$\frac{V_{\text{ball}}}{V_{\text{cube}}} = \frac{\pi^{n/2}}{2^n \Gamma(1 + \frac{n}{2})}. \quad (3.2)$$

We need not graph this function to see what will happen as n is increased - the denominator will grow much more rapidly than the numerator causing the efficiency to tend to zero as $n \rightarrow \infty$. Indeed in the jump from 2D to 3D we drop from 79% to 52% efficiency, and by $n = 10$ we reach 0.25%. Even in this ideal case, evaluating the entire grid becomes intolerable for higher dimensionality.

An n -cube of sides $4R$ is a more realistic scenario (although still generous), and in this case the 3D efficiency is just 6.5%. This does not imply that grid-based approaches must be discarded completely, only that calculating an integral by evaluating a multi-dimensional rectangular grid in its entirety is out of the question.

A general solution to this problem requires an integration method which limits evaluations of the posterior distribution such that the majority take place within the regions of significant probability density.

3.2.2 Posterior sampling

The most widely-used alternative to grid-based approaches are Markov-chain Monte-Carlo (MCMC) methods. Rather than trying to map out the posterior in a systematic way, MCMC seeks to generate a representative random sample from the posterior distribution. Consequently, the posterior doesn't need to be explicitly integrated in order to obtain marginal distributions - they are instead generated by projecting the sample onto whichever sub-set of the parameters are desired.

MCMC methods generate a ‘chain’ of locally-correlated samples using a Markov process, where the probability of moving to any chosen new state (i.e. point in the probability space) is set only by the currently occupied state. At a high level MCMC can be viewed as random walk around the probability space where some steps are rejected and re-drawn based on particular criteria. If these criteria are chosen correctly, the walk will produce a representative sample given enough steps. We will not discuss the specifics of how these methods operate, but useful descriptions can be found in Gelman [24], Kruschke [25] and a review by Brooks [26].

3.2.2.1 Convergence

It can be challenging to decide at what point a given chain has sufficiently explored the posterior such that the sample produced can be considered to be representative, and capable of yielding accurate estimates of marginal distributions. A variety of methods for making decisions regarding convergence have been proposed [27, 28], but this remains one of the more difficult aspects of using MCMC.

3.2.2.2 Burn-in

As the starting location of any chain is not guaranteed to lie in an area of the posterior which contains significant density, often chains must ‘crawl’ towards the high-density areas before they can begin to generate a representative sample. For this reason the initial evaluations of the chain, up to some chosen number, are discarded in order to ensure the sample is not biased. These discarded evaluations are called the ‘burn-in’ period of the chain, and while necessary this procedure does decrease computational efficiency.

3.2.2.3 Thinning

After a chain is terminated and the burn-in has been removed the sample is sometimes ‘thinned’, where every n ’th element of the chain is kept and all others are discarded. This is done in order to produce *uncorrelated* samples. Adjacent samples in the chain are correlated with one another, but the extent of the correlation between two elements falls as their separation in the chain is increased. By discarding typically the large majority of the evaluations thinning also has a large impact on computational efficiency, but because of this its usefulness in most situations has been questioned [29].

3.2.2.4 Limits on parallelisation

Because the calculation of each new sample in the chain requires the previous one, the evaluation of a chain is typically limited to a single computational thread. In some cases the calculation of the posterior may itself be parallelised, but even if this is an option it is typically not worthwhile unless the cost of a single evaluation is very high. The workload can instead be distributed by evaluating multiple chains simultaneously each using its own thread. This does however increase the amount of wasted posterior evaluations as every chain must discard its burn-in period, and sets an upper-limit on the number of chains which can be usefully evaluated in parallel.

3.3 Improving grid-based approaches

We now investigate the possibility of an alternative to MCMC methods for problems of relatively low dimensionality based on intelligently evaluating regular grids. We showed earlier that evaluating posterior distributions on many-dimensional rectangular grids is extremely inefficient, because the vast majority of the grid cells contain no significant probability density. To solve this problem, an algorithm is required which can locate areas of significant density in the probability space, and only evaluate grid cells in those regions. For any such algorithm to be of general use, the grid cannot take the form of a multi-dimensional array for two reasons. Firstly, for higher dimensionality problems the resulting total amount of grid cells could not be stored in the working memory, and secondly defining the grid through a fixed array requires that the grid is of finite extent in the probability space, and we must choose this extent *a priori*.

Instead we will define the grid simply by discretising the entire probability space, and store any evaluation of the posterior with the coordinates of that discrete spatial point. This way, the only cells which must be kept in memory are those which have been evaluated and the grid has no defined edges. The algorithm must serve 3 primary functions. First, it must locate the regions of highest probability density in the space, second it must decide what constitutes ‘significant density’, and finally it must evaluate all points in the discretised probability space which are considered significant.

3.3.1 The GridFill algorithm

We now present details of a novel algorithm named ‘GridFill’ which was developed to meet these criteria. GridFill has three core loops which each serve a specific function:

- ‘Find’ - uses a Monte-Carlo search to locate areas of significant density.
- ‘Climb’ - uses discrete-space hill-climbing to find the maxima of significant density regions.
- ‘Fill’ - evaluates all cells which are expected to have a value above a threshold based on a chosen fraction of the global maximum value.

The algorithm makes decisions about which cells to evaluate based on two sources of information - the density values of cells which have already been evaluated and the ‘status’ value of cells. Each cell has an integer status value of 0, 1 or 2 which are used to identify a given cell as having a certain property. All cells initially have status 0, which indicates that they are unevaluated. A status of 1 indicates that the cell has been evaluated and is an ‘interior’ cell, meaning that all its nearest-neighbours (all cells reachable by allowing each of the current cell’s grid coordinates to be altered by a maximum of 1) are also evaluated. A status of 2 indicates that the cell is evaluated and is an ‘edge’ cell, having at least one unevaluated (i.e. status 0) nearest-neighbour.

Aside from the densities and statuses, there are four additional variables used: s and s_{\max} are the current and maximum ‘search count’. Each time the Find loop evaluates a cell s is incremented by one - when s reaches s_{\max} it is assumed that all significant maxima have been located and the Fill loop is initiated. s_{\max} may be chosen by the user to suit a particular problem or set automatically based on the grid dimensions. P_{\max} stores the current maximum density value of all evaluated cells.

The Climb loop uses discrete-space hill-climbing in order to find local maxima. This works by calculating the probability density of all the nearest-neighbours of the current cell and comparing these densities to its own. If no neighbours have a larger density, the current cell is deemed to be a local maximum, else the neighbour with the largest

density becomes the new current cell. This process is repeated until a local maximum is located. This method is likely less efficient than other optimisation algorithms, but has the significant benefit that because all evaluations occur on the grid, none of the evaluations are ‘wasted’.

Each time the Climb loop locates a maxima, its value is compared to P_{\max} , and if required P_{\max} is updated to reflect the new maximum density. The ‘threshold’ τ is the fraction of P_{\max} which is used to distinguish between density values which are deemed to be significant or not (i.e. only density values greater than τP_{\max} are considered significant).

A high-level description of the algorithm is as follows:

- (a) Starting cell is chosen as the centre of the grid (unless specified otherwise).
- (b) Climb loop evaluates cells in the up-hill direction until the first maxima is located. P_{\max} is set equal to the density of the maxima.
- (c) Find loop searches for a new cell which has a value greater than τP_{\max} .
- (d) Once a cell meeting this criteria is found, the Climb loop travels to the local maxima of that cell. If the density of the maxima is greater than P_{\max} , its value is updated.
- (e) Steps (c) & (d) are repeated in order to continually search for significant maxima while $s < s_{\max}$.
- (f) When $s = s_{\max}$ the Fill loop identifies every edge cell whose value is greater than τP_{\max} , then creates a list of the nearest-neighbours of those cells. Any cells in this list which are status zero are then evaluated (then becoming status two).
- (g) Step (f) is repeated until there are no remaining edge cells with value greater than τP_{\max} , at which point the algorithm terminates.

A complete flow-chart description of GridFill is shown in figure 3.1.

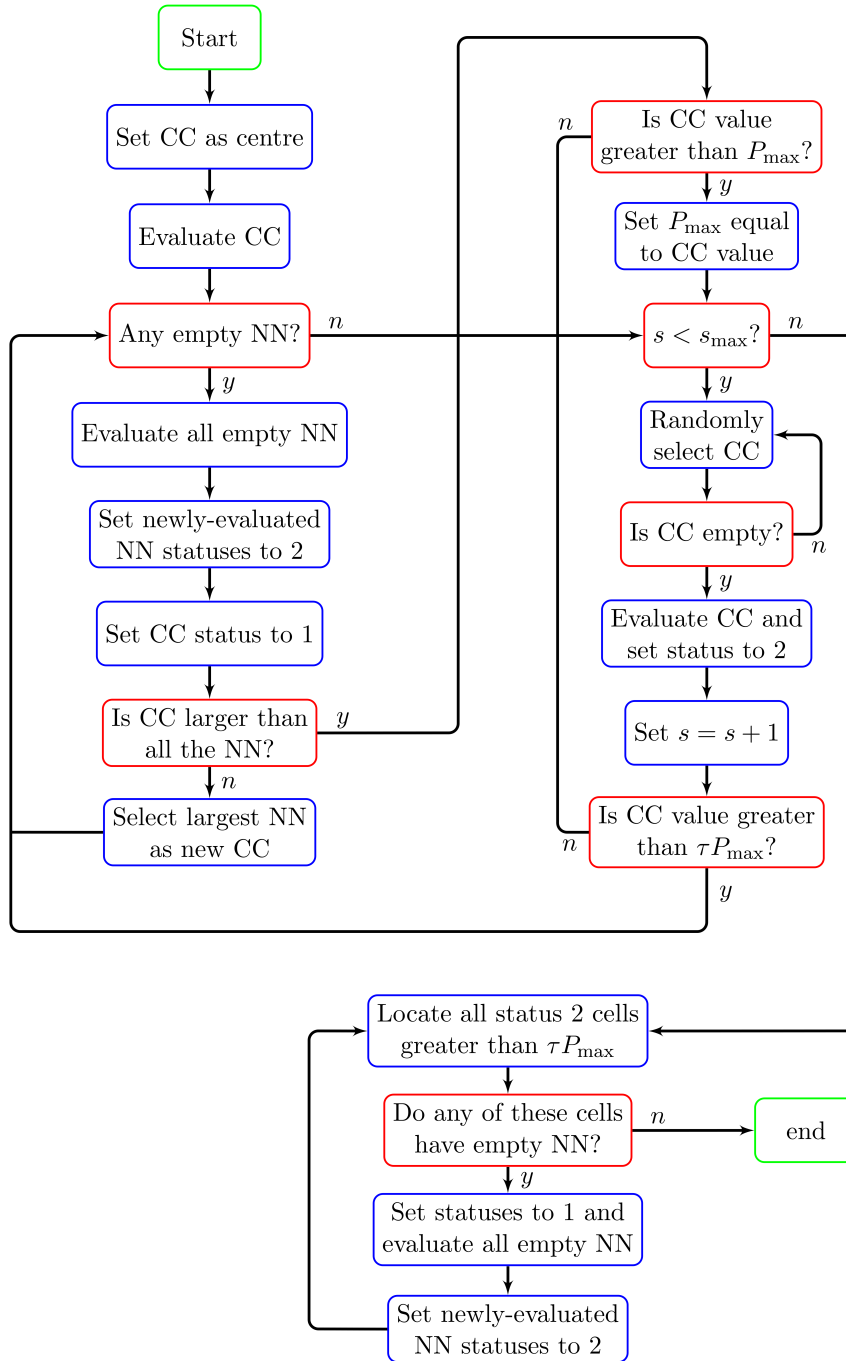


Figure 3.1: Flow diagram for the current version of GridFill. Action and decision nodes are outlined in blue and red respectively. ‘Current cell’ is abbreviated as CC, and ‘nearest-neighbours’ as NN.

3.3.2 Implementation

GridFill has been implemented as a class in Python 3. Early versions were limited to 2D and 3D problems in order to test various approaches to the 3 core program loops (Find, Climb and Fill). The code was later redeveloped to handle problems of arbitrary dimensionality. Containing the algorithm inside a class has proved particularly convenient as it allows GridFill to be applied to any problem without modification. After

the class is initialised, the user requests the ‘to evaluate’ list - this is simply a list of coordinate vectors which correspond to particular points in the discretised probability space. The user evaluates the posterior distribution at each of these points, and passes these values back to the class. GridFill then uses this information to generate a new list of points to be evaluated and the process is repeated in a loop until the algorithm terminates.

Figure 3.2 shows the evaluated areas of a 2D probability space containing four bivariate normal distributions at various stages of the algorithm. The process by which the probability space is mapped out is difficult to illustrate in more than two dimensions, but the progression is effectively the same as that seen in Figure 3.2 regardless of the number of dimensions.

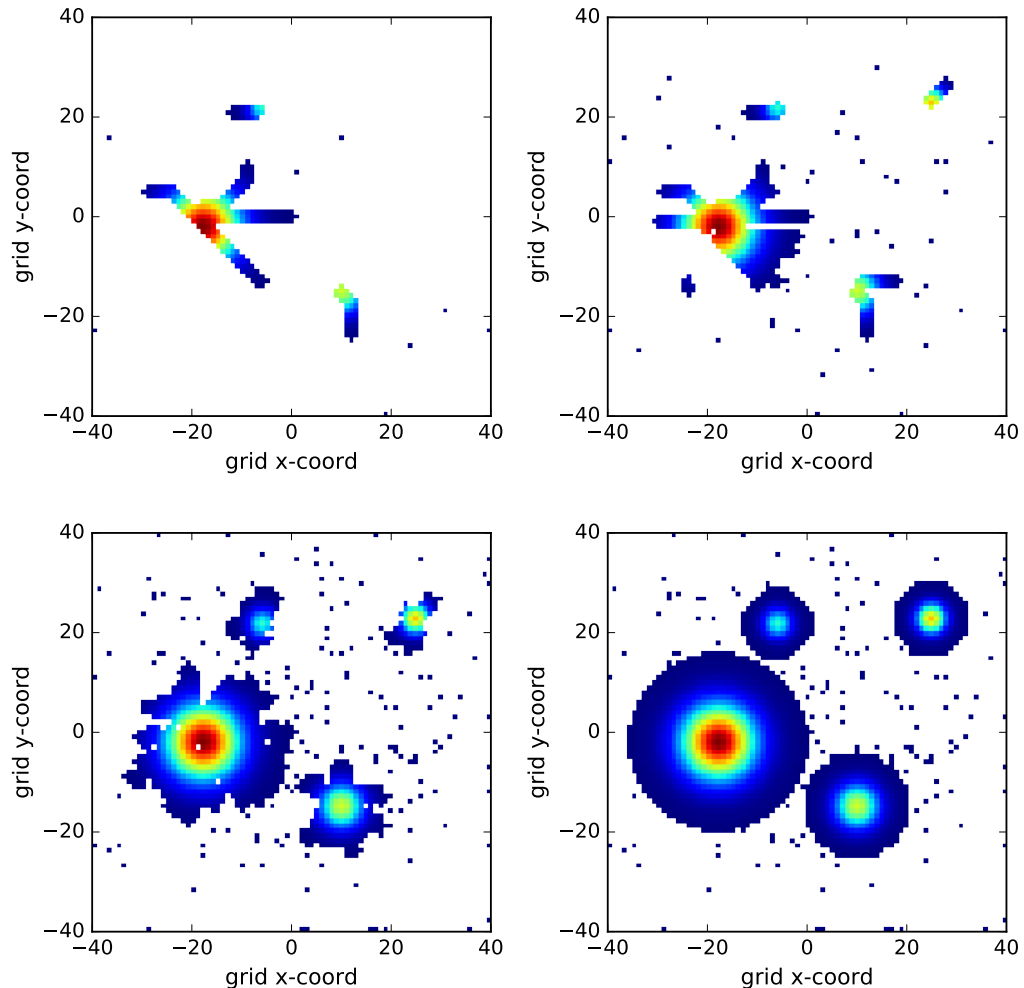


Figure 3.2: Plots of a 2D posterior distribution evaluated using GridFill after various numbers of cell evaluations. The upper-left panel shows the first 250 evaluations of the posterior, and the upper-right and lower-left panels show 750 and 1250 evaluations respectively. The lower-right panel shows the posterior after GridFill has terminated, in this case after ~ 1700 evaluations. The colour of each cell indicates the posterior value at that location.

3.3.3 Performance testing

The total run-time T of the algorithm may be expressed as

$$T = m (\bar{t}_{ev} + \bar{t}_d), \quad (3.3)$$

where m is the total cell evaluations, and \bar{t}_{ev}, \bar{t}_d are the mean evaluation and decision times respectively. We define \bar{t}_{ev} as the average time required to evaluate the posterior distribution for a single cell, and \bar{t}_d as the amount of time GridFill spends deciding which cells to evaluate divided by the total number of evaluations. If we assume that evaluating the same problem on a rectangular grid takes a time $T_0 = m_0 \bar{t}_{ev}$ where m_0 is the total number of elements in the grid, then the speed-up factor given by GridFill is

$$\frac{T}{T_0} = \frac{m}{m_0} \left(1 + \frac{\bar{t}_d}{\bar{t}_{ev}} \right). \quad (3.4)$$

The two ratios m/m_0 and \bar{t}_d/\bar{t}_{ev} are therefore the key factors which determine the performance of the algorithm. To investigate these quantities we will use the following test posterior distribution

$$P(\underline{\theta}|\mathcal{D}) = \frac{A_1}{(\sigma\sqrt{2\pi})^n} \exp \left[- \sum_{i=1}^n \frac{(\theta_i - c_1)^2}{2\sigma^2} \right] + \frac{A_2}{(\sigma\sqrt{2\pi})^n} \exp \left[- \sum_{i=1}^n \frac{(\theta_i - c_2)^2}{2\sigma^2} \right], \quad (3.5)$$

where n is the number of dimensions. The rationale here is that this simple posterior can be marginalised analytically for any of the $\underline{\theta}$, yielding

$$P(\theta_0|\mathcal{D}) = \frac{A_1}{\sigma\sqrt{2\pi}} \exp \left[- \frac{1}{2\sigma^2} (\theta_0 - c_1)^2 \right] + \frac{A_2}{\sigma\sqrt{2\pi}} \exp \left[- \frac{1}{2\sigma^2} (\theta_0 - c_2)^2 \right]. \quad (3.6)$$

This allows direct comparison between the analytically and numerically determined marginal posterior.

GridFill was used to evaluate the test posterior for n between 2 and 7, and the results are summarised in figure 3.3. The computation times quoted in these results were obtained using a Intel Xeon X5470 processor. Firstly we see that in all cases $m < m_0$, but additionally that the ratio m/m_0 , the fractional reduction in total evaluations

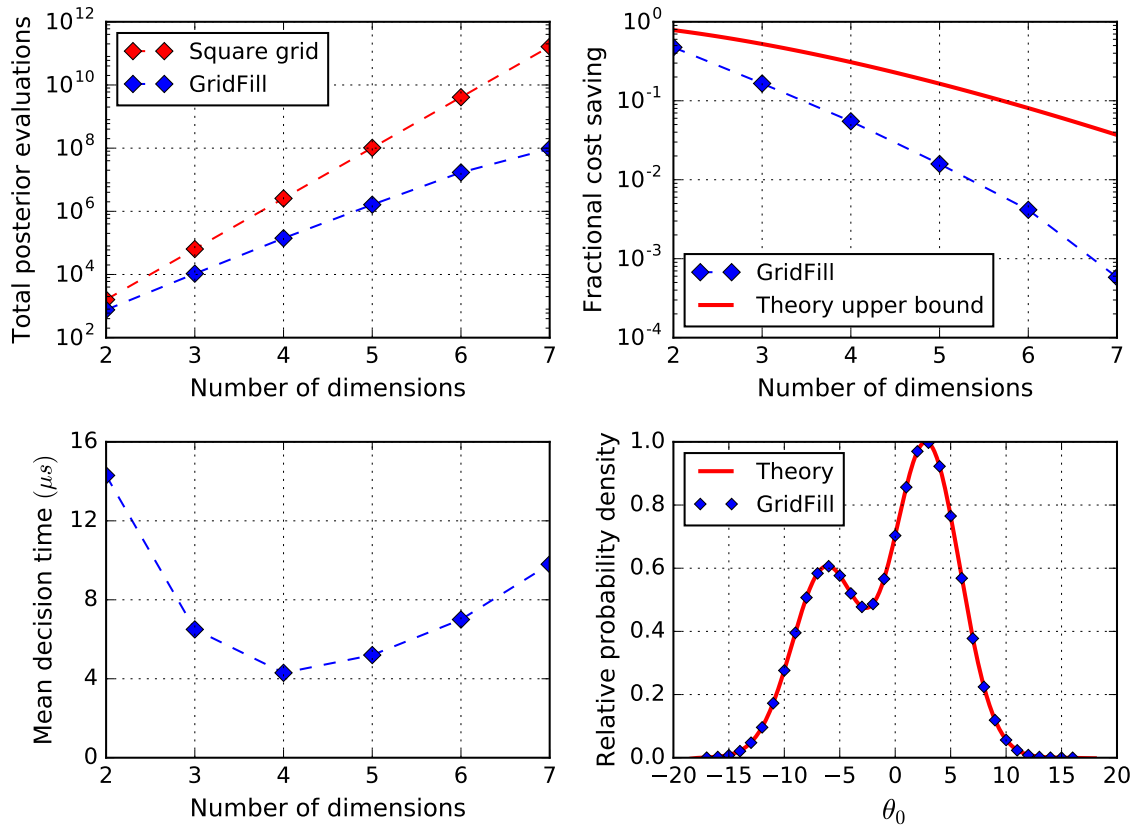


Figure 3.3: Summary of GridFill testing results. (upper-left): The amount of evaluations requested by GridFill prior to termination, and the minimum size any rectangular grid which could hold those evaluations. (upper-right): The fractional reduction in total evaluations (with respect to the ideal rectangular grid), along with the upper-bound predicted in (3.2). (lower-left): The mean decision time \bar{t}_d for each test case. (lower-right): Comparison of the analytically and numerically determined marginal posterior for the $n = 6$ case.

compared with a rectangular grid, falls off quickly with n (super-exponentially, in fact). Due to the symmetry of the test problem, the minimum rectangular grid needed to contain the significant density regions has the same number of points in each dimension regardless of the total number of dimensions. Consequently the size of this grid (shown in red, top-left figure 3.3) is given by L^n for grid length L and dimensionality n , with $L = 40$ in this case. We also find that m/m_0 falls under the theoretical upper-bound set by the ideal case of the minimum n -cube able to encapsulate a given n -ball, the expression for which is given in (3.2).

The calculated values of the mean decision time were initially unintuitive, having a minimum at $n = 4$. After consideration, we found that this occurs because the Find and Climb loops are unavoidably less efficient on a per-cell basis than the Fill loop. For low n , the number of cells evaluated in the Find/Climb loops is comparable to the Fill loop, but as n increases the Fill loop quickly dominates the evaluations causing the

initial fall in \bar{t}_d . However, because the computational complexity of GridFill increases (albeit gently) with both n and m (and that m increases rapidly with n), \bar{t}_d begins to rise again for $n > 4$. In this case $\bar{t}_{ev} \approx 20 \mu s$, and as such variation in the \bar{t}_d/\bar{t}_{ev} term from (3.4) has little impact on the speed-up factor when compared with m/m_0 .

We also note that the numerical marginalisation results from GridFill show excellent agreement with the analytical result in (3.6) for all n tested. Ultimately the accuracy of the numerical results depends the spacing of the probability space discretisation and the threshold value (which was taken to be e^{-7} in these tests).

3.3.4 A note on parallelisation

For greater than 2 dimensions, the overwhelming majority of the posterior evaluations take place during the algorithm’s ‘Fill’ state. Typically, these evaluations are requested in a relatively small number of large batches. Figure 3.4 shows the number of requested posterior evaluations per iteration during the Fill loop for the 5-dimensional test case from the previous section. All of the requested evaluations may be computed indepen-

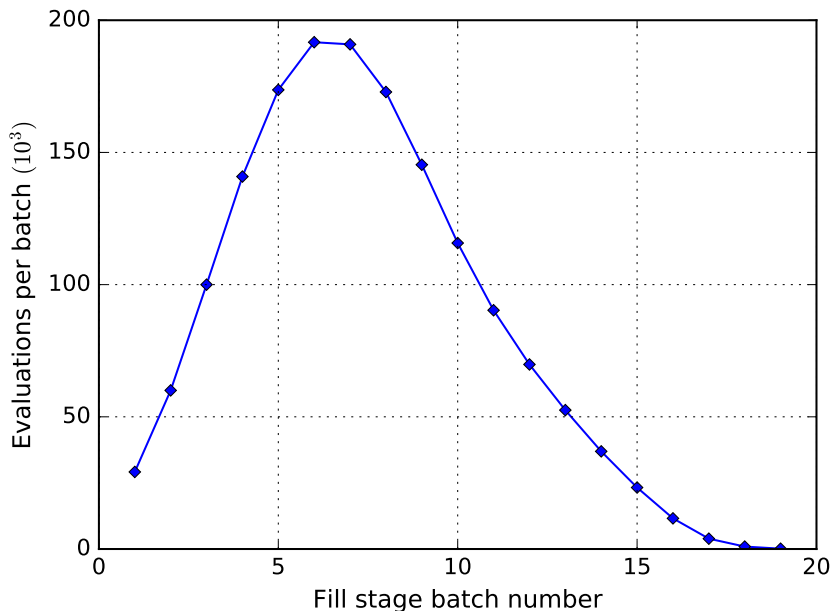


Figure 3.4: Plot of the number of evaluations requested by GridFill per iteration during the Fill loop in a 5D test-case.

dent of one another, meaning that workload of each batch can be distributed across effectively any amount of available CPU cores because there are many thousands of

3.3. Improving grid-based approaches evaluations per batch. In this case the 99.2% of the total evaluations occurred during the Fill loop, making the overall process very parallelisable. Although GridFill is currently implemented in Python, the function which evaluates the posterior may be in another language which is simply called from Python.

This approach was successfully tested using a posterior function implemented in Fortran. The coordinates of requested evaluations were written to file as binary during each GridFill iteration, and then a Fortran executable was called from Python. The Fortran code distributed the evaluations of the posterior at each coordinate over any chosen number of processors using OpenMP.

Distributing the posterior evaluations in this way reduces the mean evaluation time \bar{t}_{ev} , but has no impact on the mean decision time \bar{t}_d . Assuming an ideal scaling where for p processors \bar{t}_{ev} is reduced to \bar{t}_{ev}/p , the parallel running time is

$$T_p = m \left(\frac{\bar{t}_{ev}}{p} + \bar{t}_d \right), \quad (3.7)$$

which implies a speed-up factor of

$$\frac{T}{T_p} = \frac{\bar{t}_{ev} + \bar{t}_d}{p^{-1}\bar{t}_{ev} + \bar{t}_d} \implies \lim_{p \rightarrow \infty} \frac{T}{T_p} = 1 + \frac{\bar{t}_{ev}}{\bar{t}_d}. \quad (3.8)$$

The effectiveness of parallelisation is therefore determined by the ratio \bar{t}_{ev}/\bar{t}_d . Some effort was made to optimise GridFill during the course of its development, which reduced \bar{t}_d significantly, however we expect meaningful further reduction is possible if additional time were dedicated to optimisation. For the test calculations summarised in figure 3.3 we found that $\bar{t}_{ev} \approx 20 \mu s$, meaning $\bar{t}_{ev} > \bar{t}_d$ for all n tested. This is encouraging because the posterior distribution used in the tests was extremely computationally inexpensive when compared to posteriors in physics inference problems, which are typically tens or hundreds of times more expensive. Consequently, in applied cases we can expect that $\bar{t}_{ev} \ll \bar{t}_d$, implying that parallelisation will offer significant performance improvements.

3.3.5 Comparison with MCMC

Although the results presented clearly demonstrate the advantages of GridFill over conventional grid-based approaches, we must also consider how it compares to MCMC methods. GridFill has some desirable properties in this regard: unlike MCMC, all posterior evaluations are kept and contribute towards characterising the posterior, none are ‘thrown away’. Additionally, as GridFill self-terminates when all significant areas of the posterior have been evaluated, it does not suffer from the uncertainty of MCMC methods when deciding whether the chains have converged to a representative sample. Provided that the Monte-Carlo search in the ‘Find’ loop successfully locates all high-density areas, GridFill will yield the same answers any time it is run for the same problem, making it effectively deterministic in comparison to the stochastic nature of MCMC.

In order to make a direct comparison, an implementation of the Metropolis-Hastings algorithm (MHA) and GridFill were applied to the same test problem, specifically a 5-dimensional problem of the type shown in (3.5). The MHA implementation used for these tests has the ability to automatically tune its proposal distribution widths to optimal values, such that the chain explores the posterior as efficiently as possible. To make the comparison, the run-time of GridFill was measured over multiple applications to the test problem - many instances of the MHA were then executed for the same length of time. These results are summarised in figure 3.5.

We find that the MHA produces very unreliable estimates of marginal distributions for chain lengths having a similar execution time to GridFill for this problem. The total number of posterior evaluations required by GridFill for this test was $\sim 2.5 \times 10^5$, with the equivalent MCMC chains having length $\sim 9 \times 10^4$. The error in the GridFill estimate was small, being less than 1% of the peak value everywhere. The test problem examined here was not intentionally chosen to be a failure-case of the Metropolis-Hasting algorithm, but it appears that this is the case. We do not expect that MCMC will perform this poorly versus GridFill over a range of different test cases. As such, further testing on other problems is required - this will be the subject of future work.

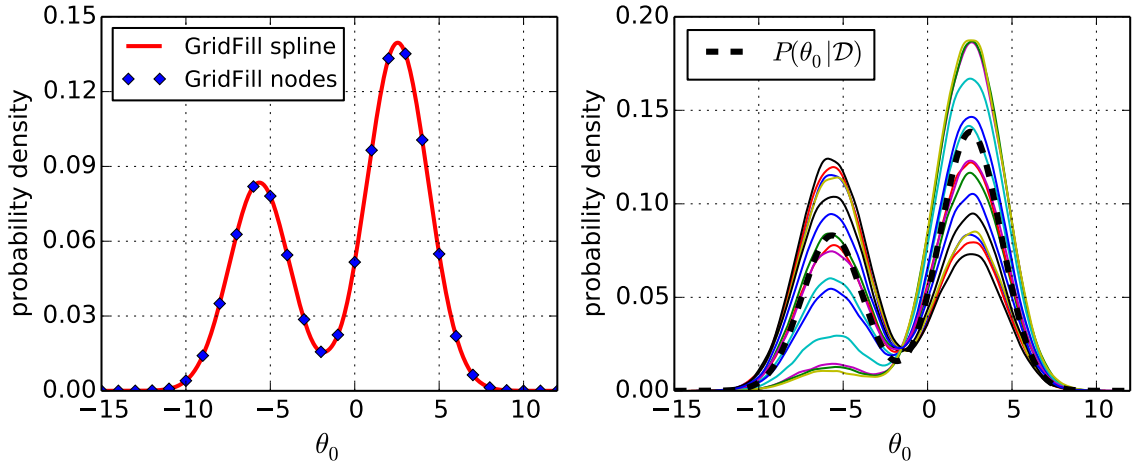


Figure 3.5: Comparison of GridFill and the Metropolis-Hastings algorithm. (left): GridFill estimate of the marginal distribution for a 5D test problem. The difference between the spline estimate and the actual marginal distribution would not be visible at the scale of this graph. (right): MCMC estimates of the marginal distribution. The solid lines show 15 separate estimates obtained using the MHA, with the actual marginal distribution shown as the dashed line.

3.3.6 Future development

Despite the benefits discussed in the previous subsection, as it stands the number of total posterior evaluations required still grows too fast to allow the algorithm to be applied to problems with more than 7 or 8 dimensions meaning MCMC remains the only option in these cases, at least for now. To understand why, we must consider the behaviour of probability distributions in many-dimensional spaces. Provided that the posterior is not periodic in any direction, we can make a few general statements, which are true in most cases:

- (a) Near the mode, the probability density is high and changes rapidly over small length scales.
- (b) Far from the mode, the probability density is low and changes slowly over large length scales.
- (c) For large n , The volume of the probability space containing densities similar to the mode density P_{\max} is much, much smaller than that which contains probabilities similar to the threshold density τP_{\max} .

Chapter 3. Developing tools for Bayesian analysis

From these statements we can make several useful observations. Firstly, to properly characterise the quickly-varying, high-density region near the mode a finely-spaced grid is needed. As the volume of this region is small, this is in itself not a problem. However, if this same finely-spaced grid is also used to map out the low density areas, which have an extremely large volume, the total number of cells required becomes impractical. The implication is clear: the volume of the grid cells *must* vary with the local probability density if this problem is to be solved. This is in fact the key behind the effectiveness of Markov-chain methods - by generating a sample from the posterior, the number of evaluations around a particular density is proportional to that density, ensuring the posterior can be well characterised without extremely large numbers of evaluations.

The next version of GridFill, which is currently in development, will adaptively sparse the grid as the probability density falls. This will be achieved by initially setting the threshold value τ to be much higher than we expect would be ultimately required. GridFill then would run as described in figure 3.1, but once the end condition is met, rather than terminating, GridFill would lower the threshold value and move back into the Fill loop. At each change of threshold, we are able to track the total probability of all cells in the grid, allowing us to set an end condition based on the convergence of the total probability rather than needing to guess the appropriate threshold level a priori.

In addition to the tracking total probability, we will also track the average probability per cell of evaluations carried out between threshold adjustments. The probability per cell can then be used as part of a criterion for deciding when the grid density should be sparsened. After sparsening, the greatly increased volume of each cell will significantly raise the probability per cell initially, but it will continue to fall as the threshold is lowered potentially leading to additional sparsenings. This approach effectively separates the evaluated space into multiple contiguous regions, with each region characterised by an effectively separate grid. When the posterior is integrated in order to calculate marginal distributions, the integrals over each region may be calculated separately and summed together.

3.4. Probabilistic calculation of credible region contour densities
 Even without these proposed improvements, we have still found GridFill to be a useful tool, and it has been used during this thesis to calculate marginal distributions for both the spectroscopy analysis example given in chapter 2 and charge-exchange parameters in chapter 5.

3.4 Probabilistic calculation of credible region contour densities

Credible regions are an important tool for effectively presenting and interpreting probability distributions obtained via Bayesian inference, especially in the case of bivariate distributions. They are the regions of the probability space which contain all values of probability density greater than some bounding value z , and enclose a total probability c which we choose. c is typically chosen as either an ‘n-sigma’ value, which is the probability contained within $\pm n\sigma$ of the mean of the normal distribution, or as a suitably high fraction such as 95%.

Defining credible regions in this manner (sometimes referred to as highest-density regions) ensures both that the region has the smallest possible extent whilst still containing the chosen total probability, and that every value of the parameters inside the region is more probable than all those outside.

Consider an arbitrary multivariate probability distribution $f(\underline{x})$. Let the total probability contained in the region $f(\underline{x}) \leq z$ be F :

$$F(z) = \int \cdots \int_{f(\underline{x}) \leq z} f(\underline{x}) \, d\underline{x}, \quad (3.9)$$

where $0 \leq z \leq \max(f)$. $F(z)$ is in some sense a cumulative distribution of $f(\underline{x})$, but one where the total probability is mapped as a function of the values of $f(\underline{x})$ itself rather than \underline{x} . Let the bounding density of the credible region enclosing a probability c be \hat{z} which may be obtained as the solution to $F(\hat{z}) = 1 - c$. Evaluating $F(z)$ is challenging using grid-based numerical integration techniques as the region $f(\underline{x}) \geq z$

can have a somewhat arbitrarily shaped footprint. Here we show that a semi-continuous probability distribution for the bounding density may be constructed using any set of samples drawn from $f(\underline{x})$.

3.4.1 Constructing the bounding density probability distribution

Suppose we have n samples $\{\underline{x}_k\}$ drawn from $f(\underline{x})$, and each sample has a corresponding probability density $f_k = f(\underline{x}_k)$. Let the $\{f_k\}$ be ordered such that $f_{k-1} < f_k < f_{k+1}$. Consider a probability density value z in the range $[f_k, f_{k+1}]$ - we know that there are k samples with a lower probability density than z and $n - k$ samples with a higher density. The probability that this arrangement occurs is

$$P(f_1, \dots, f_k \leq z < f_{k+1}, \dots, f_n) = F^k(1 - F)^{n-k}. \quad (3.10)$$

Given that $F \in [0, 1]$ we can convert the above into a probability density through division by

$$\int_0^1 F^k(1 - F)^{n-k} dF = \frac{k!(n - k)!}{(n + 1)!}, \quad (3.11)$$

yielding a probability distribution for $F(z)$:

$$P(F|n, k) = \frac{F^k(1 - F)^{n-k}(n + 1)!}{k!(n - k)!}. \quad (3.12)$$

Recall from (3.10) that the value of k defines a range of possible z values, and if we set $F(z) = 1 - c$ the density z becomes the bounding density \hat{z} . We now make this substitution in (3.12) to obtain an expression we will label p_k :

$$p_k = \frac{(1 - c)^k c^{n-k}(n + 1)!}{k!(n - k)!}. \quad (3.13)$$

For \hat{z} in the range $[f_k, f_{k+1}]$ we may say that $P(\hat{z}|c) \propto p_k$. Given that we know $0 \leq \hat{z} \leq \max(f)$, it is at this point convenient to add two extra elements to the $\{f_k\}$:

$$f_0 = 0, \quad f_{n+1} = \max(f). \quad (3.14)$$

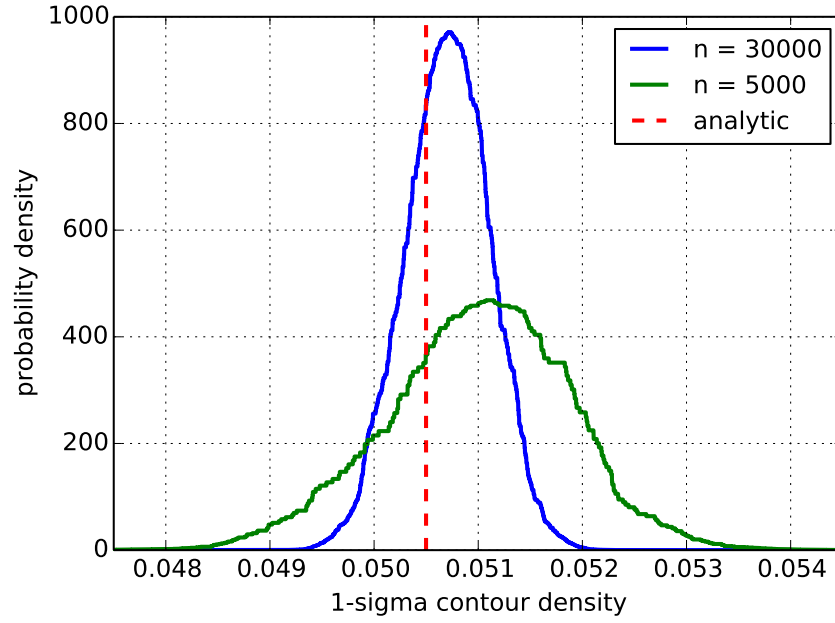


Figure 3.6: Two evaluations of the 1-sigma bounding density probability distribution for two separate samples drawn from a circular bivariate normal distribution with unit variance. The dashed line shows the exact analytical value of the 1-sigma bounding density.

This allows the distribution $P(\hat{z}|c)$ to be defined in a piecewise manner as follows

$$P(\hat{z}|c) = \begin{cases} p_0/\lambda & : f_0 < \hat{z} < f_1 \\ p_1/\lambda & : f_1 < \hat{z} < f_2 \\ \vdots & \\ p_n/\lambda & : f_n < \hat{z} < f_{n+1} \end{cases}, \quad (3.15)$$

where λ is a normalisation constant given by

$$\lambda = \sum_{k=0}^n p_k (f_{k+1} - f_k). \quad (3.16)$$

We now have the density of \hat{z} everywhere in $[f_0, f_{n+1}]$ which, because of our additions in (3.14), is the full domain $[0, \max(f)]$. The mode can be easily obtained as the region

$$f_m < \arg \max_{\hat{z}} P(\hat{z}|c) < f_{m+1}, \quad m = \left\lfloor \frac{1-c}{n} \right\rfloor. \quad (3.17)$$

Figure 3.6 shows $P(\hat{z}|c)$ evaluated for two separate sets of samples drawn from the

following circular bivariate normal distribution:

$$f(\mathbf{x}) = \frac{1}{2\pi\sqrt{|\Sigma|}} \exp\left[-\frac{1}{2}\mathbf{x}^\top \Sigma \mathbf{x}\right], \quad \Sigma = \begin{bmatrix} 1 & 0 \\ 0 & 1 \end{bmatrix}, \quad \mathbf{x} = \begin{bmatrix} x \\ y \end{bmatrix}. \quad (3.18)$$

The bounding densities can be obtained analytically for this distribution as

$$c = \iint_{f(\mathbf{x}) \geq \hat{z}} f(\mathbf{x}) \, d\mathbf{x} \implies \hat{z} = \frac{1-c}{2\pi}. \quad (3.19)$$

Taking the 1-sigma probability of $c = 0.6827$ gives the bounding density as $z = 0.0505$, which as expected falls within the high probability regions of $P(\hat{z}|c)$ for both sets of samples.

3.4.2 Mean, variance and error scaling

Calculating the moments of $P(\hat{z}|c)$ is trivial given that the probability density is constant between each set of samples $[f_k, f_{k+1}]$, so $P(\hat{z}|c)$ has no explicit \hat{z} dependence. The mean is therefore a weighted sum of the integrals of \hat{z} over each $[f_k, f_{k+1}]$ interval:

$$\mu = \int_{f_0}^{f_{n+1}} \hat{z} P(\hat{z}|c) \, d\hat{z} = \frac{1}{\lambda} \sum_{k=0}^n p_k \int_{f_k}^{f_{k+1}} \hat{z} \, d\hat{z} = \frac{1}{2\lambda} \sum_{k=0}^n p_k (f_{k+1}^2 - f_k^2). \quad (3.20)$$

In the same way the variance is simply

$$\text{Var}[\hat{z}] = \frac{1}{\lambda} \left(\sum_{k=0}^n p_k \int_{f_k}^{f_{k+1}} \hat{z}^2 \, d\hat{z} \right) - \mu^2 = \frac{1}{3\lambda} \left(\sum_{k=0}^n p_k (f_{k+1}^3 - f_k^3) \right) - \mu^2. \quad (3.21)$$

Clearly, because $P(\hat{z}|c)$ is constructed from a random sample the mean and variance themselves have some distribution of possible values prior to the drawing of the sample. This is not to suggest that the expression in (3.21) is an approximation - the calculated variance is exact for a given sample. The distribution of possible values arising from different samples reflects that each sample carries different information contributing toward our knowledge of \hat{z} . This is illustrated in figure 3.7 - variances calculated from different samples of the same size have a distribution of values, but the expected value

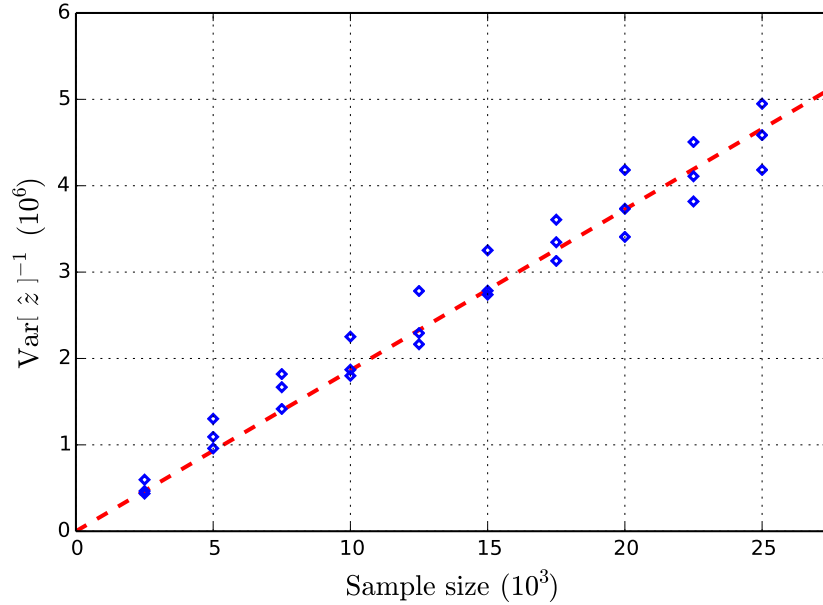


Figure 3.7: Each point represents an independent sample drawn from (3.18). The variance of the bounding density calculated using (3.21) is here seen to be inversely proportional to the sample size n .

of this distribution is inversely proportional to the sample size n . This aligns with our expectation from Monte-Carlo techniques that the error (i.e. the standard deviation) should fall as one over the root of the sample size, which is indeed what we see:

$$\sqrt{\text{Var}[\hat{z}]} \propto \frac{1}{\sqrt{n}}. \quad (3.22)$$

The ability to calculate the variance exactly is useful because it allows the sample size to be increased until the uncertainty in the contour density falls to the desired level. The tolerance required can be determined from the fact that the separation between the modes of the distributions for adjacent contours must be much larger than the standard deviation of either distribution.

3.4.3 Effective presentation of inference results

Bivariate distributions are often presented in a fashion similar to that in figure 3.8. Colour plots such as this can be useful for gaining qualitative appreciation for the structure of the distribution, but do a poor job of giving quantitative information about the probability of the result falling in particular regions of the parameter space.

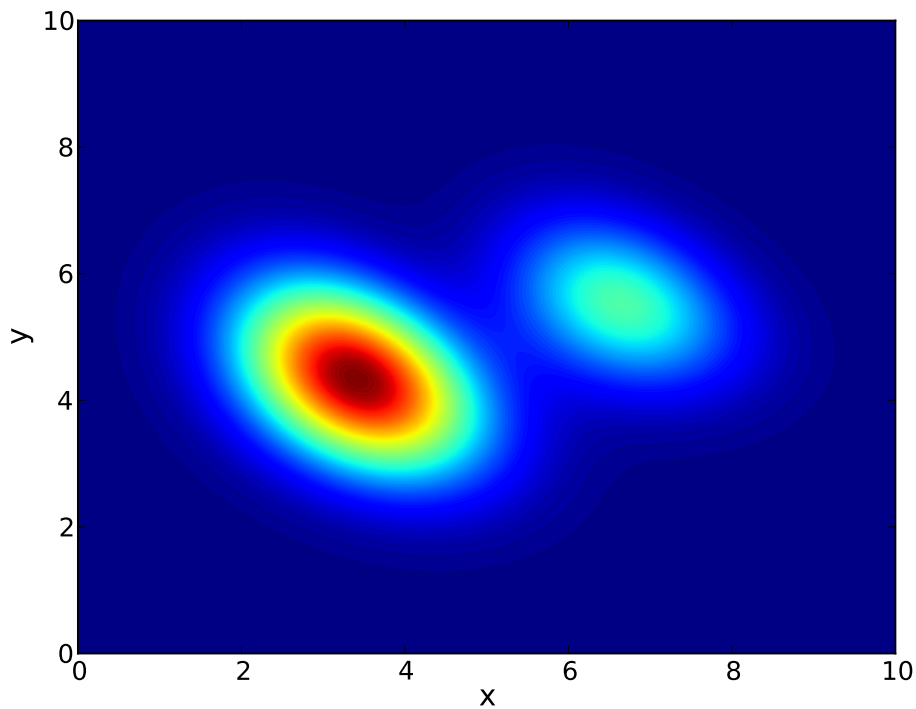


Figure 3.8: Example of a typical colour contour plot used to show the structure of a bivariate probability distribution. The distribution shown here is used only for the purpose of discussing plotting techniques.

Boundary contours of credible regions may be added to colour plots to alleviate this problem.

However, we assert that optimal way to present results of this type is to contour exclusively using credible regions. Normally in contour plots the levels for each contour are selected based only on probability densities - for example by picking a maximum and minimum density and generating a number of uniformly-spaced levels to fill that range. In this case the jump between adjacent contours represents a fixed change in probability density. Our suggestion is to choose the contour levels such that the jump between adjacent contours represents a fixed change in total contained probability.

The distribution shown in figure 3.8 has been re-plotted in figure 3.9 using the suggested method. Every contour (other than that at 99%) has a total contained probability which differs from its neighbours by 0.1. Contouring in this way gives much clearer quantitative information to the reader, and additionally gives a sense of the gradients of contained probability in the parameter space, rather than gradients in local probability density.

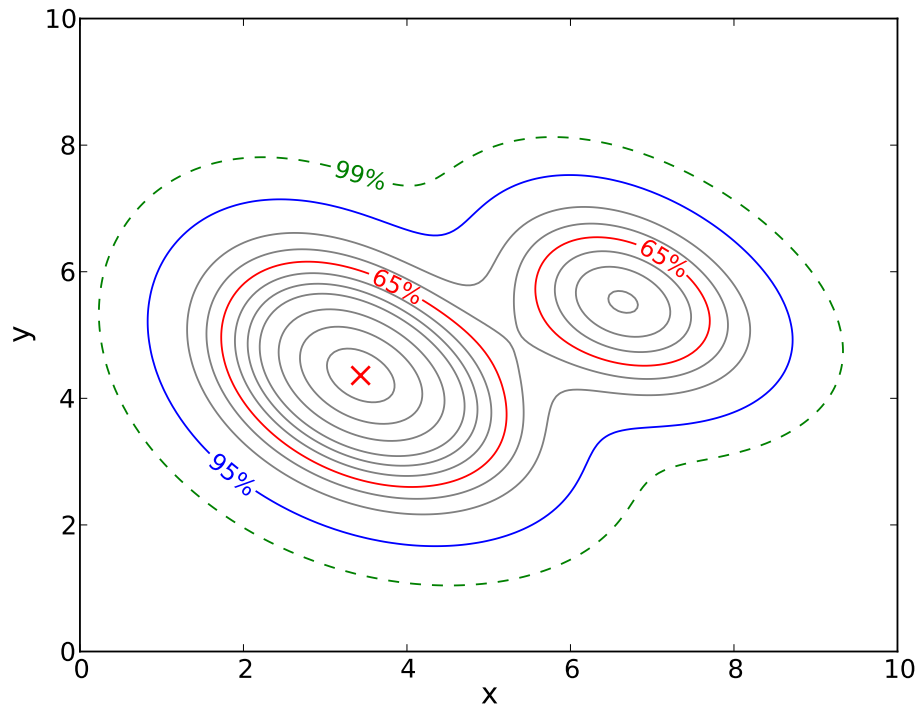


Figure 3.9: The distribution shown in figure 3.8 is plotted here using only credible region boundary contours. The solid contours run from 5% to 95% contained probability with gaps of 10%. The contours at 65% and 95% are highlighted as they are closely analogous to the one and two sigma contours. The cross marker shows the location of the global maximum (i.e. the mode).

3.5 Summary

Calculation of marginal distributions in Bayesian data analysis often necessitates the evaluation of many-dimensional integrals over the posterior. In section 3.2 we demonstrated theoretically that conventional grid-based approaches to evaluating such integrals for a high number of dimensions n are extremely inefficient, with only a tiny fraction of the grid cells containing any significant probability density. A brief overview of Markov-chain Monte-Carlo methods was given, which are currently the most widely-used solution to the problems of high- n integration.

In section 3.3 we investigated whether grid-based approaches could be improved to offer a viable alternative for certain classes of integration problem. This led to the development of the GridFill algorithm, which determines what areas of a probability space contain significant probability density and evaluates only these areas. Discussions of GridFill's design and implementation were presented, and the performance of the

Chapter 3. Developing tools for Bayesian analysis

algorithm was assessed for various n using a test-case which could be scaled to any chosen number of dimensions. The results showed that GridFill performs drastically better than a conventional grid, and that it is undoubtedly a useful tool for lower- n marginalisation problems. The issue of GridFill's lack of applicability to higher- n problems was discussed at length, and a modification to the algorithm was proposed, which we expect to greatly improve performance for large n . Future work on GridFill will focus on implementing these improvements, and further quantitative comparison with MCMC methods.

In section 3.4 the usefulness of credible regions in interpreting results in Bayesian inference was discussed. The calculation of the probability density of the contour which forms the boundary of a credible region is challenging using grid-based approaches, but is made much easier with a Monte-Carlo approach. We showed that a semi-continuous probability distribution for the boundary density for a region containing any chosen amount of total probability may be constructed using any sample drawn from the distribution. This allows the uncertainty in the calculation of the boundary density to be determined exactly, so that the sample size may be increased until the uncertainty falls to desired levels. Finally, we discussed the presentation of 2D inference results, and proposed a standardised approach where distributions are visualised using the boundary contours of a series of credible regions containing a set of fixed probabilities.

Chapter 4

Probabilistic noise-correction of discrete Fourier transform coefficients

4.1 Introduction

Advancing our understanding of magnetic confinement fusion has often necessitated progressively more challenging measurements and complex diagnostic systems. The ability of our instruments to make such measurements can be limited by a poor signal-to-noise ratio (SNR). As a result, the use of signal processing techniques to extract information from noisy data has become an important part of modern magnetic confinement research.

This work was motivated by an experiment on the KSTAR tokamak in South Korea in which electron temperature measurements required careful signal analysis. KSTAR possesses an electron-cyclotron emission imaging (ECEI) diagnostic capable of measuring fluctuations in electron temperature in a 2D plane with excellent spatiotemporal resolution [30]. The nature of the emission process causes the temperature as measured over an integration time to fluctuate randomly about the true value, resulting in thermal Gaussian noise.

The experiment aimed to measure two physics parameters, Δ' and w_c , which determine the stability and evolution of neo-classical tearing modes [17, 31]. In particular, w_c is predicted to subtly affect the spatial profile of the electron temperature in the vicinity of a magnetic island [32]. The thermal noise present in the measurements makes distinguishing these subtle features very challenging, and prompted an investigation into the removal of random noise from measured signals. An example of the data in question is shown in figure 4.1, where the level of noise compared with the oscillation amplitude can be seen clearly.

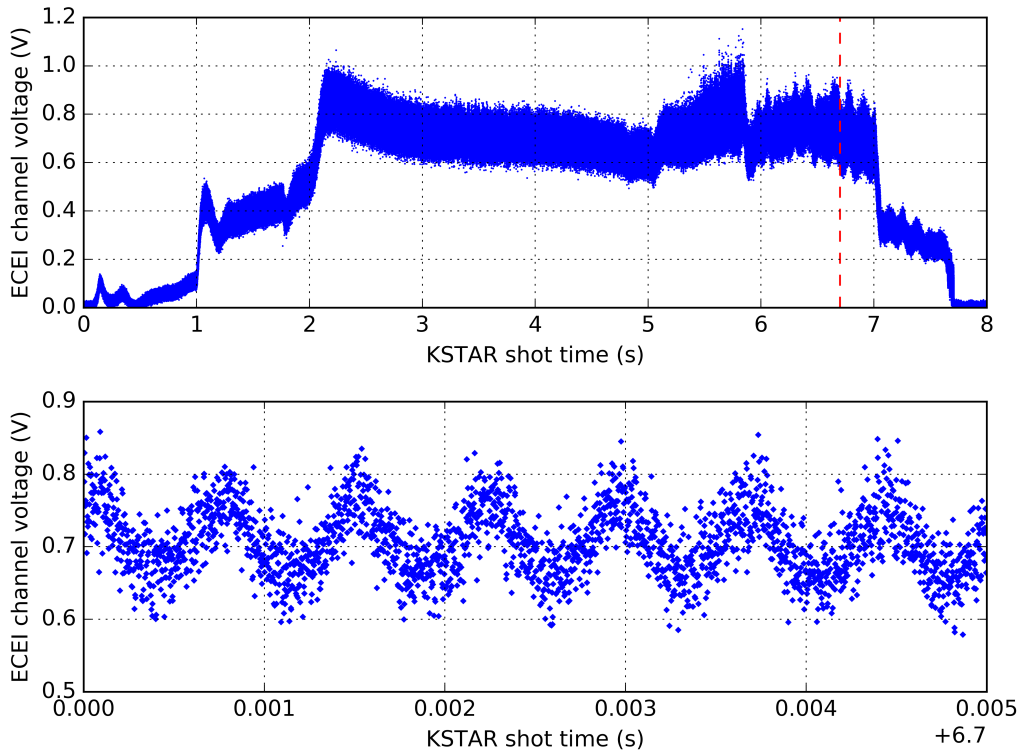


Figure 4.1: Plot of KSTAR ECEI channel #91 from shot #6123. The upper panel shows the variation of the channel across the entire shot, with the dashed line indicating the starting point of the lower panel, which shows the temperature oscillations. The ECEI channel voltage here is used as a proxy for the electron temperature.

In particular we focused on the discrete Fourier transform (DFT), which is commonly used to analyse the frequency-space information of measured signals. In the experiment, all relevant information was known to reside within a 0.25 – 10 kHz frequency band such that band-pass filtering could be used to remove the majority of the noise. However, this approach does not address the noise which remains within the pass-band. Given the difficulty of the measurement in question, finding a means to correct for the noise in the pass band would be highly beneficial.

In this chapter we demonstrate that probability concepts can be used to derive a correction to DFT coefficients which results in a reduction in the overall noise level of a signal after an inverse-transform. This allows for a partial removal of the noise contained in the pass-band, which under normal circumstances remains untreated. Previous work in which probability theory has been applied to the DFT is often based on the use of some assumed model for the signal of interest [33]. The approach described here seeks to be more general by assuming only that the ‘true’ signal which we wish to estimate is deterministic, and the noise by which it is obscured is random. This allows the signal to be separated into random and non-random components, in turn allowing the construction of probability distributions for the deterministic signal.

In section 4.2 we discuss the effect of the forward-DFT on the random noise component of the signal and its implications for deriving a noise-correction. Section 4.3 introduces a noise-correction to the Fourier magnitude and explores the efficacy of such a correction theoretically, as well as addressing the possibility of a correction to the Fourier phase. Section 4.4 discusses various mathematical approaches to estimating the prior distribution, which is required for the calculation of the magnitude correction. In section 4.5 an example calculation of the correction is presented. In Section 4.6 simulated datasets are used to investigate the performance of the magnitude correction with respect to reducing the level of random noise. In section 4.7 the correction technique is applied to the KSTAR ECEI data which motivated this work. Finally, conclusions and further work are discussed in section 4.8.

4.2 Random noise in the Fourier domain

Consider a series $G \in \mathbb{R}$ having N elements, whose discrete Fourier transform (DFT) is given by

$$z_k = \mathcal{F}\{G\}_k = \frac{1}{N} \sum_{n=0}^{N-1} G_n \exp\left(-i \frac{2\pi kn}{N}\right). \quad (4.1)$$

Let $G_n = \bar{G}_n + \mathcal{E}_n$ where \bar{G}_n is a deterministic series which we wish to estimate, and \mathcal{E}_n is a stochastic variable which represents the presence of random noise in G_n . Due

Chapter 4. Probabilistic noise-correction of discrete Fourier transform coefficients
to the linearity of the DFT we may write $\mathcal{F}\{G\} = \mathcal{F}\{\bar{G}\} + \mathcal{F}\{\mathcal{E}\}$. Considering the
transform of \mathcal{E} separately we have:

$$\mathcal{F}\{\mathcal{E}\}_k = \frac{1}{N} \sum_{n=0}^{N-1} \mathcal{E}_n \cos\left(\frac{2\pi kn}{N}\right) - i \frac{1}{N} \sum_{n=0}^{N-1} \mathcal{E}_n \sin\left(\frac{2\pi kn}{N}\right). \quad (4.2)$$

The terms inside the summations in (4.2) are themselves random variables due to
the presence of \mathcal{E}_n , so for sufficiently large N (and certain constraints on \mathcal{E}_n) the
central limit theorem [34] ensures that both the real and imaginary parts of $\mathcal{F}\{\mathcal{E}\}_k$
are normally distributed with variance σ^2 . Defining $\mathcal{F}\{G\}_k = z_k = x_k + iy_k$ and
 $\mathcal{F}\{\bar{G}\}_k = \bar{z}_k = \bar{x}_k + i\bar{y}_k$ allows the probability distributions for x and y to be expressed
as

$$\begin{aligned} P(x|\bar{x}, \sigma) &= \mathcal{N}(\bar{x}, \sigma^2) = \frac{1}{\sigma\sqrt{2\pi}} \exp\left[-\frac{(x - \bar{x})^2}{2\sigma^2}\right], \\ P(y|\bar{y}, \sigma) &= \mathcal{N}(\bar{y}, \sigma^2) = \frac{1}{\sigma\sqrt{2\pi}} \exp\left[-\frac{(y - \bar{y})^2}{2\sigma^2}\right]. \end{aligned} \quad (4.3)$$

The noise distribution in the Fourier-domain is therefore independent of that in the
time-domain provided the aforementioned conditions are met. This effect is illustrated
in figure 4.2, where noise generated from two non-gaussian distributions is shown to
agree with the normal distributions in (4.3) after a discrete Fourier-transform.

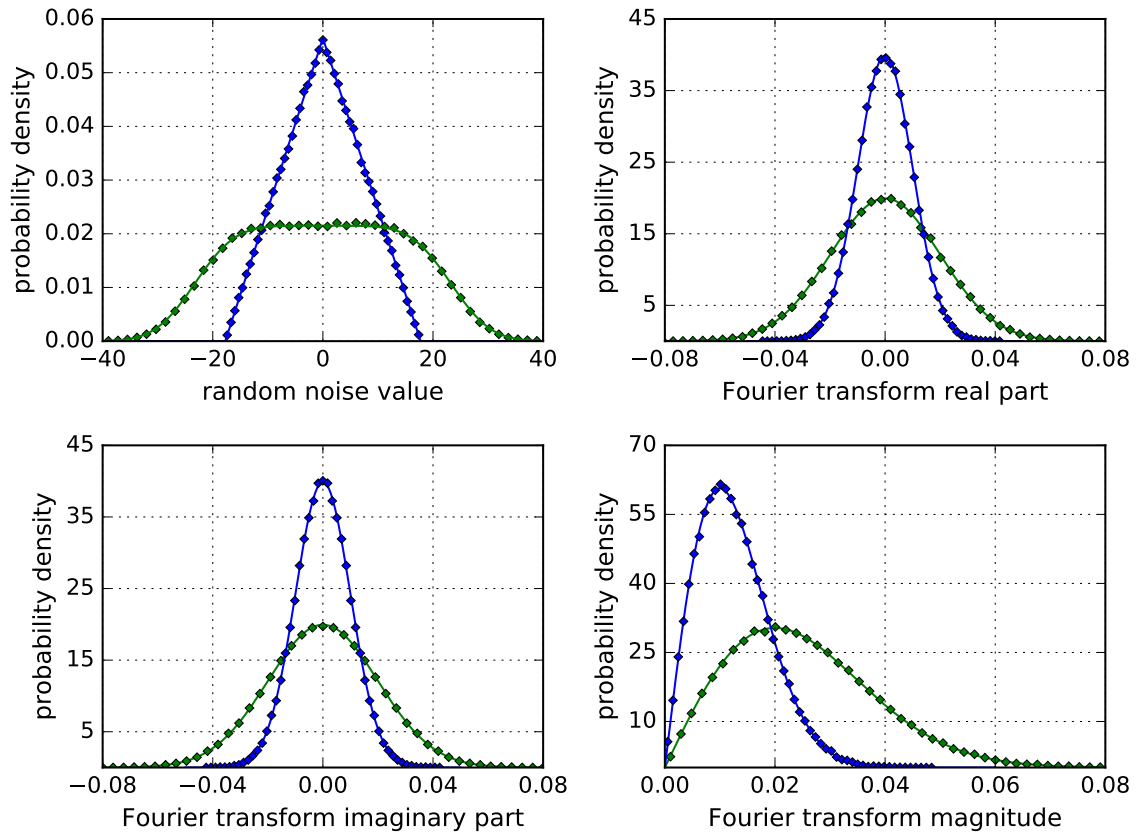


Figure 4.2: The top-left panel shows histograms of two samples of size 10^5 drawn from a triangle distribution and the convolution of a uniform distribution and a normal distribution. The DFT of these samples was calculated, and histograms of the real/imaginary parts and the magnitude are shown in the other panels. The points are the probability densities determined from histograms, and the lines are analytical predictions made using equations (4.3), (4.7) and (4.15).

4.2.1 Relating \mathcal{E}_n to the Fourier domain noise level σ

We may relate the Fourier-domain noise standard-deviation σ to that in the original series by making use of Parseval's theorem, which in this context states that

$$\frac{1}{N} \sum_{n=0}^{N-1} \mathcal{E}_n^2 = \sum_{k=0}^{N-1} |\mathcal{F}\{\mathcal{E}\}_k|^2. \quad (4.4)$$

Using $\mathcal{F}\{\mathcal{E}\}_k = (x_k - \bar{x}_k) + i(y_k - \bar{y}_k)$ we may instead write

$$\frac{1}{N} \sum_{n=0}^{N-1} \mathcal{E}_n^2 = \sum_{k=0}^{N-1} (x_k - \bar{x}_k)^2 + \sum_{k=0}^{N-1} (y_k - \bar{y}_k)^2. \quad (4.5)$$

The probability distributions in (4.3) imply that

$$\lim_{N \rightarrow \infty} \frac{1}{N} \sum_{k=0}^{N-1} (x_k - \bar{x}_k)^2 = \lim_{N \rightarrow \infty} \frac{1}{N} \sum_{k=0}^{N-1} (y_k - \bar{y}_k)^2 = \sigma^2, \quad (4.6)$$

so again assuming N is acceptably large, (4.5) may be re-written as

$$\sigma^2 \simeq \frac{1}{2N^2} \sum_{n=0}^{N-1} \mathcal{E}_n^2. \quad (4.7)$$

This relationship between the noise level in the original series and the Fourier domain will be used later when predicting the performance of noise-corrections.

4.2.2 Inference of \bar{z}_k

Bayes' theorem may be applied to the real and imaginary parts' distributions individually to obtain

$$P(\bar{x}|x, \sigma) = \frac{P(x|\bar{x}, \sigma) P(\bar{x})}{P(x)}, \quad (4.8)$$

$$P(\bar{y}|y, \sigma) = \frac{P(y|\bar{y}, \sigma) P(\bar{y})}{P(y)}. \quad (4.9)$$

Additionally, the independence of x and y allows us to write their joint distribution as

$$P(x, y|\bar{x}, \bar{y}, \sigma) = P(x|\bar{x}, \sigma) P(y|\bar{y}, \sigma), \quad (4.10)$$

the joint probability distribution for \bar{x} and \bar{y} is therefore

$$P(\bar{x}, \bar{y}|x, y, \sigma) = \frac{P(x, y|\bar{x}, \bar{y}, \sigma) P(\bar{x}, \bar{y})}{P(x, y)}. \quad (4.11)$$

Simultaneous inference of \bar{x} and \bar{y} is only equivalent to inferring them individually as in (4.8) and (4.9) on the assumption that $P(\bar{x}, \bar{y}) = P(\bar{x}) P(\bar{y})$. There is no reason to expect that this is true in general, and as such deriving a correction based on $P(\bar{x}, \bar{y}|x, y, \sigma)$ is preferable.

It is crucial to note that because $P(x|\bar{x}, \sigma)$ and $P(y|\bar{y}, \sigma)$ are normal distributions, any correction based on $P(\bar{x}, \bar{y}|x, y, \sigma)$ is entirely determined by the choice of prior $P(\bar{x}, \bar{y})$. This is because if an uninformative (flat) prior is chosen, $P(\bar{x}, \bar{y}|x, y, \sigma)$ is bivariate normal centred on x, y . In this case, the optimal estimate of (\bar{x}, \bar{y}) is simply (x, y) - i.e. there is no correction whatsoever.

4.2.3 The $P(\bar{x}, \bar{y})$ prior distribution

One might assume that because \bar{x} and \bar{y} are properties of the unknown true series \bar{G} we have no information from which to estimate $P(\bar{x}, \bar{y})$. This is not the case, which we can demonstrate by first constructing the joint distribution

$$P(x, y, \bar{x}, \bar{y}, \sigma) = P(x, y|\bar{x}, \bar{y}, \sigma) P(\bar{x}, \bar{y}) P(\sigma). \quad (4.12)$$

We cannot obtain $P(\bar{x}, \bar{y})$ by marginalising x, y and σ from the above, as the following circular result is obtained:

$$\begin{aligned} P(\bar{x}, \bar{y}) &= \iiint_{\Omega} P(x, y, \bar{x}, \bar{y}, \sigma) dx dy d\sigma \\ &= P(\bar{x}, \bar{y}) \int_{-\infty}^{\infty} P(\sigma) \left(\int_{-\infty}^{\infty} \int_{-\infty}^{\infty} P(x, y|\bar{x}, \bar{y}, \sigma) dx dy \right) d\sigma = P(\bar{x}, \bar{y}). \end{aligned} \quad (4.13)$$

We can, however, obtain $P(x, y)$ by integrating over \bar{x} , \bar{y} and σ :

$$P(x, y) = \int_{-\infty}^{\infty} P(\sigma) \left(\int_{-\infty}^{\infty} \int_{-\infty}^{\infty} P(x, y | \bar{x}, \bar{y}, \sigma) P(\bar{x}, \bar{y}) d\bar{x} d\bar{y} \right) d\sigma \quad (4.14)$$

We assume that $P(x, y)$ is a function which is representative of the local densities of the set of measured x_k and y_k , and as such we have information from which we can estimate it. Typically $P(\sigma)$ may also be obtained from the measured signal, which will be discussed in detail later. In principle, all quantities in (4.14) other than $P(\bar{x}, \bar{y})$ are known - this is a deconvolution problem with $P(\bar{x}, \bar{y})$ as the solution.

4.2.4 Challenges of correcting z_k

We have demonstrated that a measured series does carry sufficient information to make a Bayesian noise-correction to discrete Fourier transform coefficients. However, obtaining $P(\bar{x}, \bar{y})$ as a solution to the inverse problem in (4.14) is difficult for several reasons. Firstly, 2-dimensional inverse problems are challenging in their own right - In general there will be infinitely many forms of $P(\bar{x}, \bar{y})$ which satisfy (4.14), and as such the problem often requires additional constraints to produce physically sensible answers. Additionally, any solution for $P(\bar{x}, \bar{y})$ will be based on an inevitably imperfect estimate of $P(x, y)$ from the finite sample given by the x_k and y_k .

We could instead make the assumption that $P(\bar{x}, \bar{y}) = P(\bar{x})P(\bar{y})$, and infer \bar{x} and \bar{y} separately, thereby reducing the 2D inverse problem to two separate 1D inverse problems. Although more manageable, these corrections share the same issues as the simultaneous inference approach - they are based entirely on the estimated priors. In the following section, we will show that progress can be made by considering the same problem in polar coordinates.

4.3 Deriving a magnitude correction

In this section the distributions for the measured Fourier magnitude and phase are used to investigate the correction problem in polar coordinates. Initially we consider only a correction to the magnitude - the phase is discussed later.

4.3.1 Distribution of the Fourier magnitude

Consider that z is a circular bivariate normal random variable, so called because it comprises of two normally-distributed parts with identical variance. The probability distribution for the magnitude of a circular normal variable (with non-zero mean), in this case $|z|$, is given by the Rice distribution [35]:

$$P(|z||s, \sigma) = \frac{|z|}{\sigma^2} \exp \left[-\frac{s^2 + |z|^2}{2\sigma^2} \right] I_0 \left(\frac{|z|s}{\sigma^2} \right), \quad (4.15)$$

where s is the unperturbed magnitude

$$s = \sqrt{\bar{x}^2 + \bar{y}^2} \quad (4.16)$$

and $I_0(u)$ is the modified Bessel function of the first kind of zeroth order, for which the general form is

$$I_\nu(u) = \sum_{m=0}^{\infty} \frac{1}{m! \Gamma(m + 1 + \nu)} \left(\frac{u}{2} \right)^{2m + \nu}. \quad (4.17)$$

It is convenient for now to assume that σ is known to sufficient accuracy that we may treat it as a constant (this assumption can be retracted later), and define the normalised measured magnitude $R = |z|/\sigma$ and the normalised true magnitude $S = s/\sigma$. The probability of R given S can now be obtained by multiplying $P(|z||s, \sigma)$ by $dz/dR = \sigma$:

$$P(R|S) = R \exp \left[-\frac{S^2 + R^2}{2} \right] I_0(RS). \quad (4.18)$$

For a given S we therefore have complete information regarding the probability of any R . Suppose that rather than a singular value of S we have some set of values $\{S_k\}$,

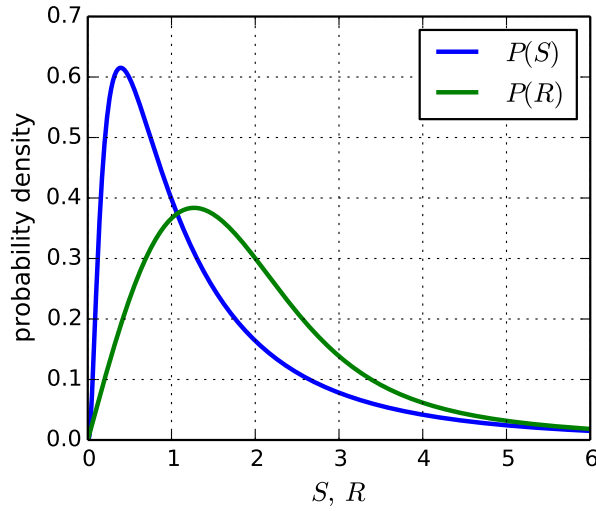


Figure 4.3: Plot of $P(R)$ resulting from a given $P(S)$. Here $P(S)$ is taken to be a log-normal distribution with parameters $\mu = 0.1$ and $\sigma = 1$.

and the local density of this set can be represented by some density function $P(S)$. We are not required to assume that the $\{S_k\}$ are an uncorrelated sample drawn from $P(S)$, only that $P(S)$ is a good representation of the local density. Making use of the product rule we may now write

$$P(S, R) = P(S|R)P(R) = P(R|S)P(S). \quad (4.19)$$

Integrating the above joint distribution over S or R yields $P(R)$ and $P(S)$ respectively, giving the following pair of relations:

$$P(R) = \int_0^\infty P(R|S)P(S) \, dS, \quad (4.20)$$

$$P(S) = \int_0^\infty P(S|R)P(R) \, dR. \quad (4.21)$$

As $P(R|S)$ is known analytically, we see in (4.20) that our definition of $P(S)$ also defines a corresponding $P(R)$, which is a function representative of the local density of the set of $\{R_k\}$ values. As before, we need not assume that the $\{R_k\}$ are uncorrelated, or a sample drawn from $P(R)$. An example of this process is given in figure 4.3, where the $P(R)$ resulting from a log-normal $P(S)$ is shown.

4.3.2 Correcting the magnitudes

From a Bayesian perspective, the measured magnitudes $|z_k|$ are fixed constants and the s_k are random variables representing the distribution of possible true magnitude values. We now introduce a ‘correction factor’ τ :

$$\tau = \frac{s}{|z|} = \frac{S}{R}. \quad (4.22)$$

Consider the magnitude of the quantity $z\tau$, noting that $\tau \in \mathbb{R}$ and hence $\tau = \tau^*$:

$$|z\tau| = \sqrt{\tau\tau^*zz^*} = \tau\sqrt{x^2 + y^2} = \frac{s}{|z|}|z| = s. \quad (4.23)$$

The error in the magnitude could therefore be corrected by replacing z_k with $\tau_k z_k$ in the inverse-DFT if the τ_k were known. Let J_n be the result of the inverse-transform where this hypothetical correction is used:

$$J_n = \sum_{k=0}^{N-1} \tau_k z_k \exp\left(\frac{i2\pi kn}{N}\right). \quad (4.24)$$

In reality the τ_k are not known constants but random variables, making J_n a sum of N random variables. Assuming the CLT holds for the τ_k , in the limit of large N the distribution of J_n will approach a Gaussian:

$$\lim_{N \rightarrow \infty} J_n \sim \mathcal{N}(E[J_n], \text{Var}[J_n]). \quad (4.25)$$

If we wish we obtain a single-value estimate for each of the values in the true series \bar{G} we may use the expectation of J_n , which given that it is normally distributed is also the mode. This is convenient because the linearity of expectation allows us to write

$$\hat{G}_n = E[J_n] = \sum_{k=0}^{N-1} E\left[\tau_k z_k \exp\left(\frac{i2\pi kn}{N}\right)\right] = \sum_{k=0}^{N-1} E[\tau_k] z_k \exp\left(\frac{i2\pi kn}{N}\right), \quad (4.26)$$

where \hat{G}_n is the magnitude-corrected series. To obtain \hat{G}_n we therefore require a general expression for $E[\tau]$. Noting that the R_k are derived from the measured signal and are

therefore known constants, and that $\tau = S/R$ we may write

$$\mathbb{E}[\tau] = \frac{\mathbb{E}[S]}{R}. \quad (4.27)$$

The expectation of S may be obtained via integration as

$$\mathbb{E}[S] = \int_0^\infty SP(S|R) \, dS. \quad (4.28)$$

$P(S|R)$ has no analytic form as it is determined entirely by $P(R|S)$ and $P(S)$ via Bayes' theorem:

$$P(S|R) = \frac{P(R|S)P(S)}{P(R)} = \frac{P(R|S)P(S)}{\int_0^\infty P(R|S)P(S) \, dS}. \quad (4.29)$$

Using the above we obtain

$$\mathbb{E}[\tau] = \frac{1}{R} \int_0^\infty \frac{SP(R|S)P(S)}{P(R)} \, dS. \quad (4.30)$$

This expression allows us to calculate the necessary corrections for all Fourier magnitudes. In an applied case where the $\{R_k\}$ are known constants we are able to estimate $P(R)$, but we cannot use the same approach to estimate $P(S)$ because the $\{S_k\}$ are not known. It is also not possible to obtain $P(S)$ via (4.21) due to the presence of the $P(S|R)$ term.

We can, however, obtain an estimate of $P(S)$ as the solution of an inverse problem defined by (4.20) given that $P(R|S)$ is known and $P(R)$ may be estimated from our data. Much of the remainder of this chapter is dedicated to investigating this inverse problem. In the course of these discussions we refer to $P(S)$ as the 'prior' and $P(R)$ as the 'evidence' on account of their placement within Bayes' theorem in (4.29). It should be noted however that while $P(S)$ may be referred to as the prior in the context of (4.29), it does not represent our 'prior knowledge' of the correction problem as a whole, and so would not be considered a prior in a philosophical sense.

We now investigate some of the properties of $\mathbb{E}[\tau]$ using simple analytic models for the prior distribution.

4.3.3 Analytical result for a uniform prior: $P(S) \propto 1$

In the simple (although generally unrealistic) case of a uniform prior where all values of S are equally likely, i.e. $P(S) \propto 1$, an analytical solution exists for $E[\tau]$. In this case, $P(S)$ vanishes from (4.29) yielding:

$$P(S|R) = \sqrt{\frac{2}{\pi}} \exp\left[-\frac{1}{2}\left(\frac{R^2}{2} + S^2\right)\right] \frac{I_0(RS)}{I_0\left(\frac{1}{4}R^2\right)}. \quad (4.31)$$

It is worth noting that the distribution for τ can be easily determined by substitution of $S = \tau R$ and multiplying by $dS/d\tau = R$:

$$P(\tau|R) = R\sqrt{\frac{2}{\pi}} \exp\left[-\frac{R^2}{2}\left(\frac{1}{2} + \tau^2\right)\right] \frac{I_0(R^2\tau)}{I_0\left(\frac{1}{4}R^2\right)}. \quad (4.32)$$

$E[\tau]$ may now be obtained either via finding $E[S]$ as in (4.30) or by integrating $P(\tau|R)$ directly (they are entirely equivalent):

$$E[\tau] = \int_0^\infty \tau P(\tau|R) d\tau = \frac{1}{R} \sqrt{\frac{2}{\pi}} \exp\left[\frac{1}{4}R^2\right] I_0^{-1}\left(\frac{1}{4}R^2\right). \quad (4.33)$$

In the limit of large R , $E[\tau]$ becomes:

$$\lim_{R \rightarrow \infty} E[\tau] = 1. \quad (4.34)$$

This limiting behaviour is certainly expected for physically sensible priors, as a coefficient with an infinitely large signal-to-noise ratio should remain unchanged by the correction because it is unaffected by the noise. It is clear from figure 4.4 that in the limit of vanishing R , $E[\tau]$ approaches infinity. This behaviour may be initially unintuitive, but can be easily understood by considering $E[S]$ in the same limit:

$$\lim_{R \rightarrow 0} E[S] = \sqrt{\frac{2}{\pi}}. \quad (4.35)$$

As $E[S]$ approaches a constant rather than zero, the correction must tend towards an infinite size in order to account for the vanishing size of R .

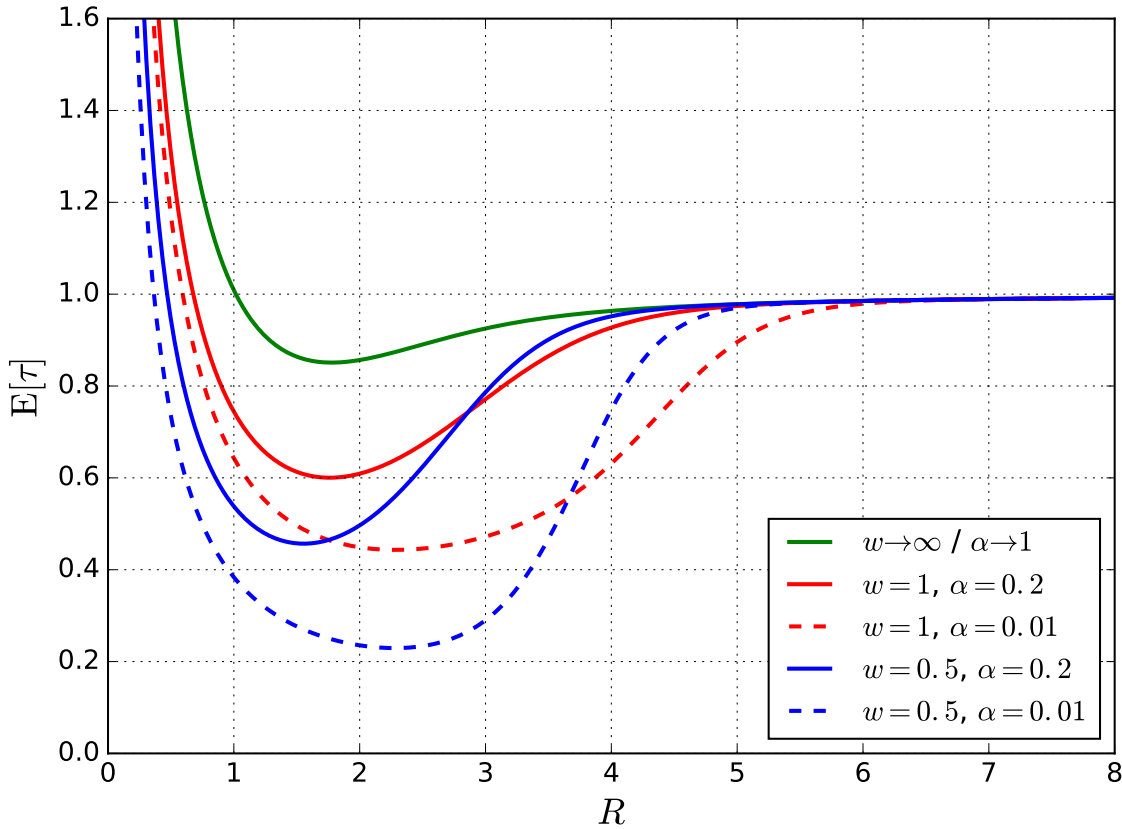


Figure 4.4: Plots of analytical results for $E[\tau]$ using a flat prior and a half-normal prior plus a constant. It can be seen that all the curves approach unity as $R \rightarrow \infty$. This is true for all cases in which $\alpha > 0$.

4.3.4 Analytical result for a half-normal prior

Although we know in actuality that $P(S)$ must equal zero in the limit that $S \rightarrow 0$, a half-normal distribution plus a constant is a simple model for which $E[\tau]$ may be obtained analytically. It is convenient to parametrise the prior in the following way:

$$P(S) \propto \alpha + \frac{(1-\alpha)}{w} \exp\left[-\frac{S^2}{2w^2}\right], \quad (4.36)$$

where $0 \leq \alpha \leq 1$ and $w > 0$. The resulting expectation of τ is

$$E[\tau] = \frac{1}{R} \sqrt{\frac{2}{\pi}} \frac{\exp\left[\frac{1}{2}R^2\right] + \gamma^2 \left(\frac{1-\alpha}{\alpha w}\right) \exp\left[\frac{1}{2}R^2\gamma^2\right]}{\exp\left[\frac{1}{4}R^2\right] I_0\left(\frac{1}{4}R^2\right) + \gamma \left(\frac{1-\alpha}{\alpha w}\right) \exp\left[\frac{1}{4}R^2\gamma^2\right] I_0\left(\frac{1}{4}R^2\gamma^2\right)}, \quad (4.37)$$

where

$$\gamma = \frac{w}{\sqrt{1+w^2}}. \quad (4.38)$$

Plots of (4.37) for various w, α are shown in figure 4.4. As expected, when $w \rightarrow \infty$ or $\alpha \rightarrow 1$ we recover the result for a flat prior:

$$\lim_{w \rightarrow \infty} \mathbb{E}[\tau] = \lim_{\alpha \rightarrow 1} \mathbb{E}[\tau] = \frac{1}{R} \sqrt{\frac{2}{\pi}} \frac{\exp\left[\frac{1}{4}R^2\right]}{I_0\left(\frac{1}{4}R^2\right)}. \quad (4.39)$$

4.3.5 Residual error after magnitude correction

To understand the nature of the noise that remains after applying the $\mathbb{E}[\tau]$ magnitude correction, we must investigate how effective \hat{G}_n is as an estimator of \bar{G}_n . To do so, we must consider a fixed set of (\bar{x}_k, \bar{y}_k) giving rise to a distribution of possible (x_k, y_k) values. Assuming again that \hat{G}_n is purely real, we may write:

$$\hat{G}_n = \sum_{k=0}^{N-1} \mathbb{E}[\tau_k] (x_k \cos(\omega kn) - y_k \sin(\omega kn)). \quad (4.40)$$

Using the distributions for (x_k, y_k) given in (4.3) we may determine the distribution of \hat{G}_n . Starting by treating the sine and cosine terms separately we have:

$$\begin{aligned} \mathbb{E}[\tau_k] x_k \cos(\omega kn) &\sim \mathcal{N}\left(\mathbb{E}[\tau_k] \bar{x}_k \cos(\omega kn), \mathbb{E}[\tau_k]^2 \sigma^2 \cos^2(\omega kn)\right), \\ \mathbb{E}[\tau_k] y_k \sin(\omega kn) &\sim \mathcal{N}\left(\mathbb{E}[\tau_k] \bar{y}_k \sin(\omega kn), \mathbb{E}[\tau_k]^2 \sigma^2 \sin^2(\omega kn)\right). \end{aligned} \quad (4.41)$$

Accounting for the sum over both terms gives the distribution for \hat{G}_n as

$$\hat{G}_n \sim \mathcal{N}\left(\sum_{k=0}^{N-1} \mathbb{E}[\tau_k] [\bar{x}_k \cos(\omega kn) - \bar{y}_k \sin(\omega kn)], \sigma^2 \sum_{k=0}^{N-1} \mathbb{E}[\tau_k]^2\right), \quad (4.42)$$

and we may therefore note that

$$\mathbb{E}[\hat{G}_n] = \sum_{k=0}^{N-1} \mathbb{E}[\tau_k] [\bar{x}_k \cos(\omega kn) - \bar{y}_k \sin(\omega kn)], \quad (4.43)$$

$$\text{Var}[\hat{G}_n] = \sigma^2 \sum_{k=0}^{N-1} \mathbb{E}[\tau_k]^2. \quad (4.44)$$

A standard measure of performance for an estimator is the mean-squared error:

$$\text{MSE} [\hat{G}_n] = \text{Var} [\hat{G}_n] + \text{Bias} [\hat{G}_n]^2, \quad (4.45)$$

where the bias of an estimator is given by the difference between the expectation value and the true value:

$$\begin{aligned} \text{Bias} [\hat{G}_n] &= \text{E} [\hat{G}_n] - \bar{G}_n \\ &= \sum_{k=0}^{N-1} (\text{E} [\tau_k] - 1) [\bar{x}_k \cos(\omega kn) - \bar{y}_k \sin(\omega kn)]. \end{aligned} \quad (4.46)$$

In full, the mean-squared error is

$$\text{MSE} [\hat{G}_n] = \left(\sum_{k=0}^{N-1} (\text{E} [\tau_k] - 1) [\bar{x}_k \cos(\omega kn) - \bar{y}_k \sin(\omega kn)] \right)^2 + \sigma^2 \sum_{k=0}^{N-1} \text{E} [\tau_k]^2. \quad (4.47)$$

As seen above, the MSE of \hat{G}_n has a dependence on n , so will be different for each element of the corrected series. To quantify the average level of noise remaining in \hat{G}_n , we define the ‘initial’ and ‘corrected’ noise levels δ_i and δ_c :

$$\delta_i = \sqrt{\frac{1}{N} \sum_{n=0}^{N-1} (G_n - \bar{G}_n)^2} = \sqrt{\frac{1}{N} \sum_{n=0}^{N-1} \mathcal{E}_n^2}, \quad (4.48)$$

$$\delta_c = \sqrt{\frac{1}{N} \sum_{n=0}^{N-1} (\hat{G}_n - \bar{G}_n)^2}. \quad (4.49)$$

To theoretically predict the value of δ_c we may replace $(\hat{G}_n - \bar{G}_n)^2$ with $\text{MSE} [\hat{G}_n]$ using (4.47). This allows us to write

$$\delta_c^2 = \sigma^2 \sum_{k=0}^{N-1} \text{E} [\tau_k]^2 + \frac{1}{N} \sum_{n=0}^{N-1} \left(\sum_{k=0}^{N-1} (\text{E} [\tau_k] - 1) [\bar{x}_k \cos(\omega kn) - \bar{y}_k \sin(\omega kn)] \right)^2. \quad (4.50)$$

Comparing (4.7) with the definition of δ_i in (4.48) we see that

$$\sigma \simeq \frac{\delta_i}{\sqrt{2N}}. \quad (4.51)$$

4.3. Deriving a magnitude correction

The noise reduction factor δ_c/δ_i is a useful figure of merit which captures the fractional reduction in the root-mean-squared error of the series due to the correction. δ_c/δ_i may now be expressed as

$$\frac{\delta_c}{\delta_i} = \sqrt{\frac{1}{2N} \sum_{k=0}^{N-1} \text{E}[\tau_k]^2 + \frac{1}{\delta_i^2 N} \sum_{n=0}^{N-1} \left(\sum_{k=0}^{N-1} (\text{E}[\tau_k] - 1) [\bar{x}_k \cos(\omega kn) - \bar{y}_k \sin(\omega kn)] \right)^2}. \quad (4.52)$$

The second term in (4.52) contains both \bar{x}_n and \bar{y}_n , so in an applied case where the true signal is unknown this term cannot be calculated. The first term depends only upon the measured signal, so may be calculated freely. As both terms are positive-definite, the first term provides a calculable lower-bound on the value of δ_c/δ_i :

$$\frac{\delta_c}{\delta_i} \geq \sqrt{\frac{1}{2N} \sum_{k=0}^{N-1} \text{E}[\tau_k]^2}. \quad (4.53)$$

4.3.6 On the possibility of phase-correction

For measured phase ϕ and true phase $\bar{\phi}$ given by

$$\phi = \arctan\left(\frac{y}{x}\right), \quad \bar{\phi} = \arctan\left(\frac{\bar{y}}{\bar{x}}\right), \quad (4.54)$$

there exists an expression for the distribution of ϕ given $\bar{\phi}$ and S [36], which is

$$P(\phi|\bar{\phi}, S) = \frac{1}{2\pi} \exp\left(\frac{-S^2}{2}\right) \left[1 + \frac{\sqrt{\pi}}{2} Q \exp[Q^2] (1 + \text{erf}(Q)) \right], \quad (4.55)$$

where

$$Q = \frac{S \cos(\phi - \bar{\phi})}{\sqrt{2}}. \quad (4.56)$$

Unlike the measured normalised magnitude R , which depends only on the true normalised magnitude S , the distribution of the measured phase depends both on $\bar{\phi}$ and S . Consequently, a correction to the phase cannot be obtained via the solution of a 1D inverse problem in the same way that is possible for the magnitude. For example,

a correction could be obtained by constructing $P(\bar{\phi}|\phi)$ as follows:

$$P(\bar{\phi}|\phi) = \int_0^\infty P(\bar{\phi}, S|\phi) dS = \frac{1}{P(\phi)} \int_0^\infty P(\phi|\bar{\phi}, S)P(\bar{\phi}, S) dS. \quad (4.57)$$

This requires $P(\bar{\phi}, S)$ which can only be obtained by solving the full 2D inverse problem

$$P(R, \phi) = \int_0^\infty \int_0^\infty P(R, \phi|S, \bar{\phi})P(S, \bar{\phi}) dS d\bar{\phi}, \quad (4.58)$$

where $P(R, \phi|S, \bar{\phi}) = P(\phi|\bar{\phi}, S)P(R|S)$. Due to this, we will consider only corrections to the magnitude in this chapter.

4.4 Estimating the prior distribution $P(S)$

As discussed in the previous section, in order to calculate the correction function $E[\tau]$ we require $P(S)$, which can be obtained as solution to the following inverse problem:

$$P(R) = \int_0^\infty P(R|S)P(S) dS. \quad (4.59)$$

In this section, we investigate the properties of this inverse problem and various approaches to solving it.

4.4.1 Properties of $P(S)$

Before considering the inverse problem any further, it is important to discuss what properties we expect $P(S)$ to have as this will affect our approach. We now introduce data from a low-noise 44 kHz audio signal consisting of $2^{17} \approx 10^5$ points. This data will be used later for testing and benchmarking the magnitude correction, but here is used to gain insight into $P(S)$. The analysis of this data is summarised in figure 4.5. The top-left plot in the figure shows the magnitude spectrum for the data. The cumulative distribution of the measured magnitudes $F(|z|)$ is shown in the top-right plot. We see that the CDF rises extremely sharply near zero, but quickly flattens and

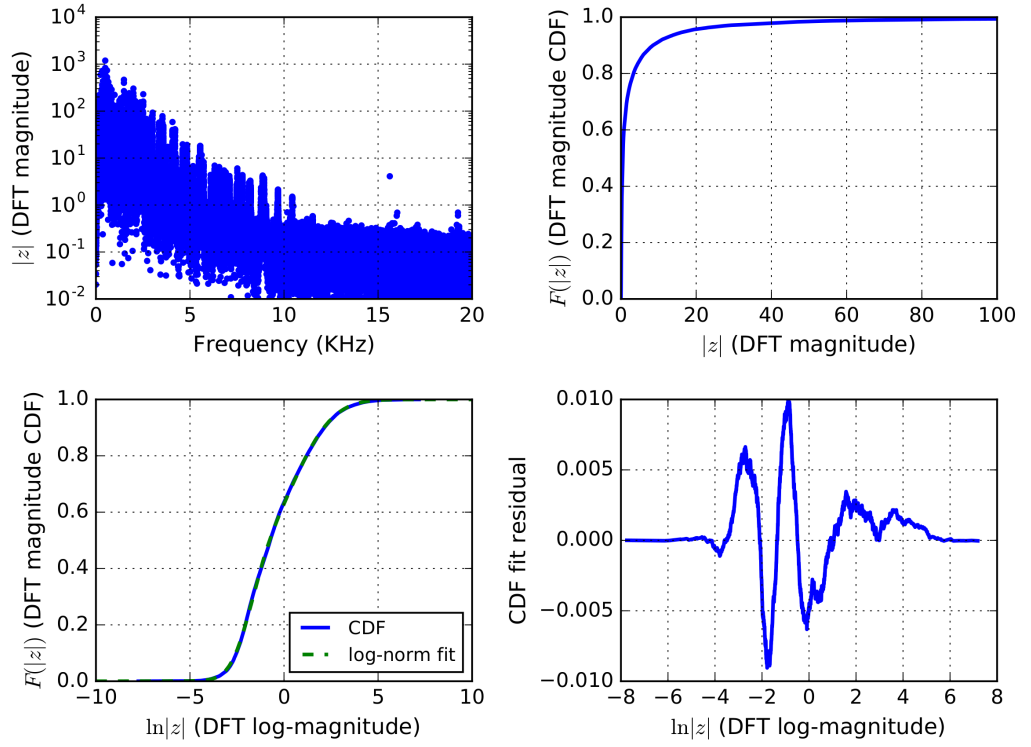


Figure 4.5: Summary of the audio test signal data. Top-left: DFT magnitude spectrum of the test signal. Top-right: cumulative distribution of the DFT magnitudes. Bottom-left: Cumulative distribution of the log-magnitude, plotted with a fit of the data using the sum of two normal distributions. Bottom-right: residual of the fit in the bottom-left plot.

approaches 1 slowly - this corresponds to an extremely skewed PDF. Looking at $F(|z|)$ with respect to $\ln |z|$ (the bottom-left plot) yields a much clearer picture - we recognise that $F(\ln |z|)$ is roughly the normal distribution CDF, and as such $P(|z|)$ is roughly log-normal. In fact, $P(|z|)$ is in this case represented extremely well by the sum of two log-normal distributions as shown by the fit residual (bottom-right plot).

Given that the level of noise in the data is relatively low, we will assume that for the purposes of studying the inverse problem the log-normal distribution is a reasonable model for $P(S)$, such that

$$P(S) = \frac{1}{Sw\sqrt{2\pi}} \exp \left[-\frac{1}{2} \left(\frac{\ln S - \mu}{w} \right)^2 \right]. \quad (4.60)$$

In order to properly choose the parameters for the log-normal model, we need to examine what a given prior implies about the level of noise in the signal. Let \mathcal{U} be the

ratio of the RMS noise to the RMS true signal:

$$\mathcal{U} = \sqrt{\left(\sum_{n=0}^{N-1} \mathcal{E}_n^2\right) / \left(\sum_{n=0}^{N-1} \bar{G}_n^2\right)}. \quad (4.61)$$

\mathcal{U} will be used as a metric for the noise level in the data. It is possible to establish a link between \mathcal{U} and $P(S)$ in the following way. First, using Parseval's theorem we may write

$$\frac{1}{N} \sum_{n=0}^{N-1} \bar{G}_n^2 = \sum_{k=0}^{N-1} |\mathcal{F}\{\bar{G}\}_k|^2 = \sum_{k=0}^{N-1} s_k^2. \quad (4.62)$$

Given that we have assumed the density of the $S_k = s_k/\sigma$ is represented by $P(S)$, the mean of the squares of the S_k is approximately

$$\frac{1}{N\sigma^2} \sum_{k=0}^{N-1} s_k^2 \approx \int_0^\infty S^2 P(S) \, dS. \quad (4.63)$$

Comparing (4.62) and (4.63) we see that

$$\sqrt{\frac{1}{N} \sum_{n=0}^{N-1} \bar{G}_n^2} \approx \sigma \sqrt{N \int_0^\infty S^2 P(S) \, dS}. \quad (4.64)$$

In (4.7) we established that

$$\sqrt{\frac{1}{N} \sum_{n=0}^{N-1} \mathcal{E}_n^2} \approx \sigma \sqrt{2N}, \quad (4.65)$$

so taking the ratio of (4.65) and (4.64) we obtain

$$\mathcal{U} = \sqrt{\left(\sum_{n=0}^{N-1} \mathcal{E}_n^2\right) / \left(\sum_{n=0}^{N-1} \bar{G}_n^2\right)} \approx \left(\frac{1}{2} \int_0^\infty S^2 P(S) \, dS\right)^{-\frac{1}{2}}. \quad (4.66)$$

Taking $P(S)$ to be log-normal as in (4.60) we find that

$$\int_0^\infty S^2 P(S) \, dS = e^{2(\mu+w^2)} \quad (4.67)$$

and as such

$$\mathcal{U} = \sqrt{2} e^{-(\mu+w^2)}. \quad (4.68)$$

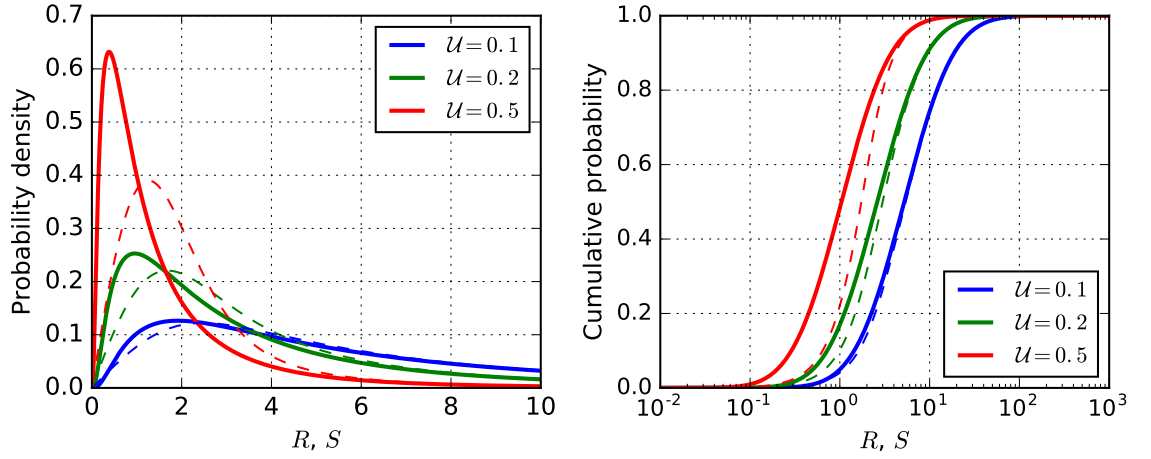


Figure 4.6: Plots of the re-parameterised log-normal distribution in (4.69) for $w = 1$ and various \mathcal{U} . The solid lines show $P(S)$ and the dashed lines show $P(R)$.

The skewness of the log-normal distribution is a monotonically increasing function of w only, as such w dictates the ‘shape’ of the log-normal distribution and μ the scale. Solving the above for μ and making the substitution back into (4.60) we obtain

$$P(S) \approx \frac{1}{wS\sqrt{2\pi}} \exp \left[-\frac{1}{2} \left(\frac{1}{w} \ln \left(\frac{SU}{\sqrt{2}} \right) + w \right)^2 \right]. \quad (4.69)$$

Plots of (4.69) for $w = 1$ (comparable to that found in the example data) and various \mathcal{U} are shown in figure 4.6. The figure also shows the corresponding $P(R)$ distributions calculated numerically using (4.20). As expected, we see for low \mathcal{U} values that $P(R)$ is very similar to $P(S)$, but the differences are significant for larger \mathcal{U} . The log-normal model developed here will be used to inform and test approaches to estimating $P(S)$ in the rest of the chapter.

4.4.2 Modifying the inverse problem

Before discussing methods to solve the inverse problem, we first examine various ways in which the problem can be modified. Consider that because $P(S)$ has no dependence on R , we may apply any linear operator which acts on R to both sides of (4.20) and $P(S)$ will be unaffected. Let $F(R)$ be the cumulative distribution function of $P(R)$ such that

$$F(R) = \int_0^R P(R') \, dR'. \quad (4.70)$$

Applying the above integral to both sides of (4.20) we obtain

$$F(R) = \int_0^R P(R') dR' = \int_0^\infty \left(\int_0^R P(R'|S) dR' \right) P(S) dS = \int_0^\infty F(R|S)P(S) dS. \quad (4.71)$$

This is a new inverse problem, still with $P(S)$ as its solution, but now the transform kernel is the cumulative distribution of $P(R|S)$ rather than $P(R|S)$ itself. This new form may be advantageous because rather than needing to estimate $P(R)$ from the $\{R_k\}$ sample, we need only estimate $F(R)$. A cumulative distribution can be estimated much more robustly than its corresponding probability distribution for a given sample. Hence by modifying the problem in this way, the term we are forced to estimate will contain less errors. This can be extremely important in inverse problems, as small variations or errors in the input function can produce large differences in the estimate of $P(S)$. It is worth noting that we could integrate or differentiate (4.20) with respect to R any number of times and still retain an integral equation for $P(S)$, giving rise to an infinite set of potential inverse problems - however given the aforementioned advantages of working with cumulative distributions we suggest that (4.71) is a good choice.

Another type of modification can be made to the problem by applying integration by parts to (4.20), which yields

$$\int_0^\infty P(R|S)P(S) dS = \left[P(R|S) \int P(S) dS \right]_0^\infty - \int_0^\infty \left(\frac{\partial}{\partial S} P(R|S) \right) \left(\int P(S) dS \right) dS. \quad (4.72)$$

Consider that $\int P(S) dS$ can differ from $F(S)$ by only a constant. Making the substitution $\int P(S) dS = F(S) + b$ for some constant b into the above yields

$$\int_0^\infty P(R|S)P(S) dS = \left[P(R|S)F(S) \right]_0^\infty + b \left[P(R|S) \right]_0^\infty - \int_0^\infty \left(\frac{\partial}{\partial S} P(R|S) \right) F(S) dS - b \left[\int \left(\frac{\partial}{\partial S} P(R|S) \right) dS \right]_0^\infty. \quad (4.73)$$

Given that

$$\left[\int \left(\frac{\partial}{\partial S} P(R|S) \right) dS \right]_0^\infty = \left[P(R|S) \right]_0^\infty, \quad (4.74)$$

the two terms containing the constant b in (4.73) cancel to give

$$\int_0^\infty P(R|S)P(S) \, dS = \left[P(R|S)F(S) \right]_0^\infty - \int_0^\infty \left(\frac{\partial}{\partial S} P(R|S) \right) F(S) \, dS. \quad (4.75)$$

Additionally, because $\lim_{S \rightarrow \infty} P(R|S) = 0$ and $\lim_{S \rightarrow 0} F(S) = 0$ it follows that

$$\left[P(R|S)F(S) \right]_0^\infty = 0, \quad (4.76)$$

and as such

$$P(R) = \int_0^\infty \left(-\frac{\partial}{\partial S} P(R|S) \right) F(S) \, dS. \quad (4.77)$$

We've now modified the problem such that the solution is $F(S)$ rather than $P(S)$. This could be advantageous because a CDF has several useful properties which can be used to constrain solutions. For example, the values of a CDF must lie in the interval $[0, 1]$ everywhere, and the first derivative must be non-negative everywhere. Integration by parts can also be used to obtain a further inverse problem where the solution is the derivative of $P(S)$, but this is not desirable so we do not derive it here.

Now consider applying the cumulative integral in (4.70) to both sides of (4.77) to obtain

$$\int_0^R P(R') \, dR' = \int_0^\infty \left(-\frac{\partial}{\partial S} \int_0^R P(R'|S) \, dR' \right) F(S) \, dS. \quad (4.78)$$

Define the modified transform kernel as

$$K(R, S) = \int_0^R R' \exp \left[-\frac{S^2 + R'^2}{2} \right] (SI_0(R'S) - R'I_1(R'S)) \, dR', \quad (4.79)$$

so that the transform can be expressed in the standard form

$$F(R) = \int_0^\infty K(R, S)F(S) \, dS. \quad (4.80)$$

This combination of the two previous modifications produces an inverse problem where both $P(R)$ and $P(S)$ are replaced with their cumulative counterparts $F(R)$ and $F(S)$.

There is one further alteration that can be made: we noted in section 4.4.1 that the

Chapter 4. Probabilistic noise-correction of discrete Fourier transform coefficients
 cumulative distributions of $\ln R$ and $\ln S$ are better behaved than $F(R)$ and $F(S)$. Let \tilde{R} and \tilde{S} be scaled versions of R and S :

$$\tilde{S} = \ln(S), \quad \tilde{R} = \ln(R). \quad (4.81)$$

By substitution we may write the inverse problem in terms of $F(\tilde{R})$ and $F(\tilde{S})$ as

$$F(\tilde{R}) = \int_{-\infty}^{\infty} K(\tilde{R}, \tilde{S}) F(\tilde{S}) \, d\tilde{S}, \quad (4.82)$$

where

$$K(\tilde{R}, \tilde{S}) = \int_{-\infty}^{\tilde{R}} \exp \left[2\tilde{R} + \tilde{S} - \frac{e^{2\tilde{S}} + e^{2\tilde{R}}}{2} \right] \left(e^{\tilde{S}} I_0 \left(e^{\tilde{R} + \tilde{S}} \right) - e^{\tilde{R}} I_1 \left(e^{\tilde{R} + \tilde{S}} \right) \right) \, d\tilde{R}. \quad (4.83)$$

In the remainder of this section we develop multiple approaches to solving the various possible inverse problems derived here.

4.4.3 Bayesian iterative procedure for estimating $P(S)$

We previously remarked that (4.21) was not useful for determining $P(S)$ - this is true in its current form, the reason being that $P(S|R)$ (the inverse transform kernel) is not known. Here we consider the result of using an approximation for $P(S|R)$. By making use of (4.19) and (4.20) we may write:

$$P(S|R) = \frac{P(R|S)P(S)}{\int_0^{\infty} P(R|S)P(S) \, dS}. \quad (4.84)$$

Substituting the above into (4.21) allows us to express $P(S)$ as:

$$P(S) = \int_0^{\infty} \left(\frac{P(R|S)P(S)}{\int_0^{\infty} P(R|S)P(S) \, dS} \right) P(R) \, dR. \quad (4.85)$$

Now define a function f_0 obtained by omitting $P(S)$ from the RHS of (4.85):

$$f_0 = \int_0^{\infty} \left(\frac{P(R|S)}{\int_0^{\infty} P(R|S) \, dS} \right) P(R) \, dR \approx P(S). \quad (4.86)$$

4.4. Estimating the prior distribution $P(S)$

Although this new expression is not equal to $P(S)$, it is at least calculable as all the terms are known. We have effectively approximated $P(S)$ to be a flat prior, but despite this the expression still carries information regarding the true $P(S)$ in the form of $P(R)$. f_0 therefore represents an initial guess at the form of $P(S)$ in the absence of any other information. We now assume that f_0 better approximates $P(S)$ than the uniform prior which was used to generate it, such that we may obtain a better approximation by replacing $P(S)$ in the RHS of (4.85) with f_0 rather than omitting it completely:

$$f_1 = \hat{Q}f_0 = f_0 \int_0^\infty \frac{P(R|S)P(R)}{\int_0^\infty P(R|S)f_0 dS} dR. \quad (4.87)$$

The operator \hat{Q} may then be recursively applied to f_0 producing successively better approximations of $P(S)$:

$$f_n = \hat{Q}^n f_0, \quad f_{n+1} = \hat{Q}f_n. \quad (4.88)$$

The fractional difference between successive approximations is given by

$$\begin{aligned} \frac{f_{n+1} - f_n}{f_n} &= f_n^{-1} (\hat{Q} - 1) f_n \\ &= \int_0^\infty \frac{P(R|S)P(R)}{\int_0^\infty P(R|S)f_n dS} dR - 1. \end{aligned} \quad (4.89)$$

This implies that if the approximation converges such that $f_{n+1} - f_n = 0$, then f_n must satisfy (4.20), and as such:

$$f_{n+1} = f_n \implies P(R) = \int_0^\infty P(R|S)f_n dS. \quad (4.90)$$

$P(S)$ may not uniquely satisfy (4.20), so convergence does not necessarily imply that $f_n = P(S)$:

$$\int_0^\infty P(R|S)f_n dS = \int_0^\infty P(R|S)P(S) dS \not\Rightarrow f_n = P(S). \quad (4.91)$$

Despite this, (4.20) is still a fairly strong constraint on the form of $P(S)$, so if f_0 is sufficiently similar to $P(S)$ we can expect a converged f_n to provide a good approximation to $P(S)$.

4.4.3.1 Testing the iterative procedure

To study the convergence properties of the algorithm we will use the prior model developed in section 4.4.1:

$$P(S) = \frac{1}{wS\sqrt{2\pi}} \exp \left[-\frac{1}{2} \left(\frac{1}{w} \ln \left(\frac{SU}{\sqrt{2}} \right) + w \right)^2 \right]. \quad (4.92)$$

This will be used to calculate $P(R)$ numerically, after which the iterative procedure will be used to recover an approximation of $P(S)$. To quantify the convergence and performance of the method we make use of the Kullback–Leibler divergence

$$\text{KL}(f(x), g(x)) = \int_{-\infty}^{\infty} f(x) \ln \left(\frac{f(x)}{g(x)} \right) dx, \quad (4.93)$$

which is a commonly used metric for the similarity between two probability distributions. To examine convergence we calculate

$$\text{KL}(f_n, f_{n-1}) = \int_0^{\infty} f_n \ln \left(\frac{f_n}{f_{n-1}} \right) dS, \quad (4.94)$$

and to examine performance we calculate

$$\text{KL}(P(S), f_n) = \int_0^{\infty} P(S) \ln \left(\frac{P(S)}{f_n} \right) dS. \quad (4.95)$$

Calculations of f_n , $\text{KL}(f_n, f_{n-1})$ and $\text{KL}(P(S), f_n)$ up to $n = 40$ using the test prior in (4.92) are summarised in figure 4.7. We see that for both values of \mathcal{U} that f_n does converge, yielding distributions which satisfy the forward transform. However, $f_{\infty} \neq P(S)$, confirming our expectation that $P(S)$ is not a unique solution of (4.20). Despite this, in both cases $f_{\infty} \approx P(S)$ and is a better approximation than assuming $P(S)$ is numerically equal to $P(R)$, i.e. that

$$P(S) \approx \int_0^{\infty} \delta(S - R) P(R) dR. \quad (4.96)$$

Although we do note that in the limit of $\mathcal{U} \rightarrow 0$ the above is true exactly:

$$P(S) = \lim_{\mathcal{U} \rightarrow 0} \int_0^{\infty} \delta(S - R) P(R) dR. \quad (4.97)$$

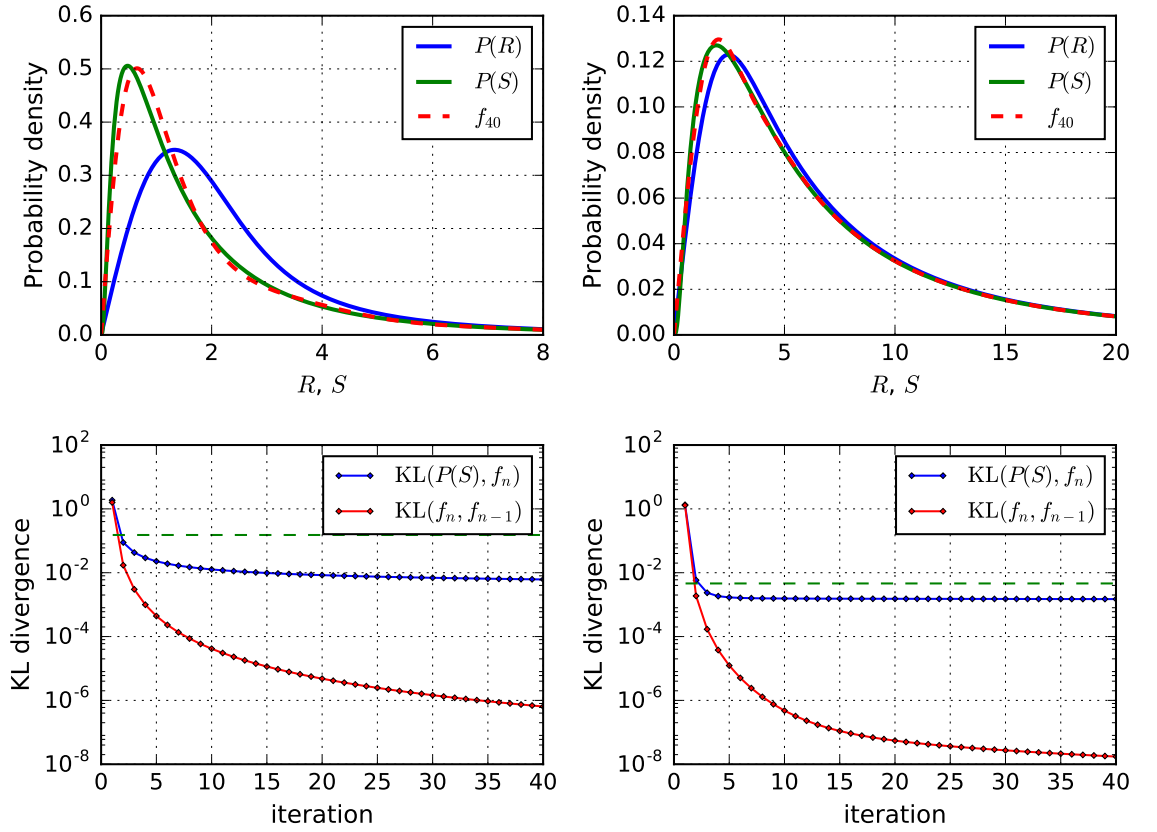


Figure 4.7: The top-left and top-right plots show $P(S)$, $P(R)$ and f_{40} for $\mathcal{U} = 0.4$ and $\mathcal{U} = 0.1$ respectively. The bottom-left and bottom-right plots show the corresponding KL-divergences given in (4.95) and (4.94). The dashed line shows the KL-divergence obtained by approximating that $P(S) = P(R)$.

In summary, this approach performs well and is promising - at least for the smooth $P(S)$ functions used in testing. For this reason it is likely best to estimate $P(S)$ as a sum of well-behaved distributions as shown in figure 4.5.

4.4.4 Linearisation of integral transforms

The type of inverse problem we must address is an integral transform, also sometimes referred to as an integral equation or a Fredholm equation of the first kind. The general form is

$$g(x) = \int_{-\infty}^{\infty} K(x, y) f(y) dy, \quad (4.98)$$

where $g(x)$ is known and we wish to solve for $f(y)$. Here we demonstrate that such an equation may be approximated as a linear system which can, in principle, be solved

Chapter 4. Probabilistic noise-correction of discrete Fourier transform coefficients directly. We begin by expressing $f(y)$ and $g(x)$ as linear combinations of some set of basis functions $\phi_i(x)$

$$f(y) = \sum_i c_i \phi_i(y), \quad g(x) = \sum_j b_j \phi_j(x), \quad (4.99)$$

which are orthonormal with respect to an inner product $\langle \phi_i, \phi_j \rangle$:

$$\langle \phi_i, \phi_j \rangle \equiv \int_{\Omega} \phi_i(x) \phi_j(x) W(x) dx = \delta_{ij}, \quad (4.100)$$

where $W(x)$ is a weighting function and Ω is the domain on which the basis is orthonormal. As $g(x)$ is known, the coefficients b_j may be obtained through the inner product

$$\langle g(x), \phi_j \rangle = \int_{\Omega} g(x) \phi_j(x) W(x) dx = \sum_k b_k \int_{\Omega} \phi_k(x) \phi_j(x) W(x) dx = \sum_k b_k \delta_{kj} = b_j \quad (4.101)$$

Now replace $f(y)$ and $g(x)$ in the integral equation from (4.98) with their new series representations in (4.99) to give

$$\begin{aligned} \sum_j b_j \phi_j(x) &= \int_{\Omega} K(x, y) \left(\sum_i c_i \phi_i(y) \right) dy \\ &= \sum_i c_i \left(\int_{\Omega} K(x, y) \phi_i(y) dy \right). \end{aligned} \quad (4.102)$$

We see that the RHS is equal to a weighted sum of the integral transform operating on each of the basis functions. Let the result of this transform be Φ_i such that

$$\Phi_i(x) = \int_{\Omega} K(x, y) \phi_i(y) dy. \quad (4.103)$$

As Φ_i is a function of x only we are free to express it in terms of the basis:

$$\Phi_i = \sum_q A_{qi} \phi_q(x), \quad (4.104)$$

where the coefficients A_{qi} are given by

$$A_{qi} = \langle \Phi_i, \phi_q \rangle = \int_{\Omega} \Phi_i(x) \phi_q(x) W(x) dx \quad (4.105)$$

4.4. Estimating the prior distribution $P(S)$

The value of A_{qi} depends only on the transform and the choice of basis, and is therefore independent of $f(y)$ and $g(x)$. We may now express (4.102) as

$$\sum_j b_j \phi_j(x) = \sum_i c_i \sum_q A_{qi} \phi_q(x). \quad (4.106)$$

We seek a linear relationship between the coefficients b_j and c_j . As the LHS of (4.106) is just a sum over the basis, the b_j may be extracted by using the inner product $\langle g(x), \phi_j \rangle$ as shown in (4.101). Taking the inner product of (4.106) and simplifying we obtain

$$\left\langle \left(\sum_j b_j \phi_j \right), \phi_\ell \right\rangle = \left\langle \left(\sum_i c_i \sum_q A_{qi} \phi_q \right), \phi_\ell \right\rangle \quad (4.107)$$

$$\int_\Omega W(x) \left(\sum_j b_j \phi_j(x) \right) \phi_\ell(x) dx = \int_\Omega W(x) \left(\sum_i c_i \sum_q A_{qi} \phi_q(x) \right) \phi_\ell(x) dx \quad (4.108)$$

$$\sum_j b_j \left(\int_\Omega W(x) \phi_j(x) \phi_\ell(x) dx \right) = \sum_i c_i \sum_q A_{qi} \left(\int_\Omega W(x) \phi_q(x) \phi_\ell(x) dx \right) \quad (4.109)$$

$$\sum_j b_j \langle \phi_j, \phi_\ell \rangle = \sum_i c_i \sum_q A_{qi} \langle \phi_q, \phi_\ell \rangle \quad (4.110)$$

$$\sum_j b_j \delta_{j\ell} = \sum_i c_i \sum_q A_{qi} \delta_{q\ell} \quad (4.111)$$

$$b_\ell = \sum_i c_i A_{\ell i}, \quad (4.112)$$

and as ℓ is a dummy index we may write

$$b_j = \sum_i c_i A_{ji}. \quad (4.113)$$

In practice we must truncate the sum of basis functions in (4.99) to some order M in order to carry out calculations:

$$f(y) = \sum_i^M c_i \phi_i(y), \quad g(x) = \sum_j^M b_j \phi_j(x), \quad (4.114)$$

allowing the following matrices to be defined:

$$\mathbf{b} = \begin{bmatrix} b_1 \\ b_2 \\ \vdots \\ b_M \end{bmatrix}, \quad \mathbf{c} = \begin{bmatrix} c_1 \\ c_2 \\ \vdots \\ c_M \end{bmatrix}, \quad \mathbf{A} = \begin{bmatrix} A_{1,1} & A_{1,2} & \cdots & A_{1,M} \\ A_{2,1} & A_{2,2} & \cdots & A_{2,M} \\ \vdots & \vdots & \ddots & \vdots \\ A_{M,1} & A_{M,2} & \cdots & A_{M,M} \end{bmatrix}. \quad (4.115)$$

The integral transform can now be represented as the following system of linear equations

$$\mathbf{b} = \mathbf{A}\mathbf{c}. \quad (4.116)$$

The simplest solution would be to find the inverse of \mathbf{A} such that $\mathbf{c} = \mathbf{A}^{-1}\mathbf{b}$, however in general this approach does not produce an accurate solution for \mathbf{c} . This occurs for a variety of reasons - firstly there is almost certainly not a unique \mathbf{c} which satisfies (4.116) for a given \mathbf{b} , but rather infinitely many solutions making this an ill-posed problem. Additionally, integral transforms tend to have a ‘smoothing’ effect on functions, which in the context of the linear system reduces the size of the higher-order coefficients significantly. Reversing this process requires potentially very small coefficients in \mathbf{b} being scaled up by large factors. Consequently, small numerical inaccuracies in the values of \mathbf{b} can result in extreme changes in the values of \mathbf{c} . Next we discuss the choice of basis functions and how the inverse problem can be constrained to improve the estimation of \mathbf{c} .

4.4.5 Chebyshev representation and prior constraints

The Chebyshev polynomials $T_n(x)$ form an orthonormal basis with respect to

$$\int_{-1}^1 T_n(x)T_m(x)W_m(x) dx = \delta_{nm}, \quad (4.117)$$

where

$$W_m(x) = \frac{h_m}{\pi\sqrt{1-x^2}}, \quad h_m = \begin{cases} 2 & m > 0 \\ 1 & m = 0 \end{cases}. \quad (4.118)$$

4.4. Estimating the prior distribution $P(S)$

Chebyshev polynomials are widely used as a basis set for numerical calculations on account of their fast convergence, i.e. that a Chebyshev series approximation of a function can achieve high accuracy with a small number of terms relative to other bases. Although the $T_n(x)$ are orthogonal on $[-1, 1]$, they can be scaled to represent functions on any chosen domain. In this case a scale factor ν is used such that the domain of $F(\tilde{S})$ and $F(\tilde{R})$ is limited to $[-\nu, \nu]$. Accordingly their Chebyshev series representations are given by

$$F(\tilde{S}) = \sum_{n=0}^{M-1} c_n T_n(\tilde{S}/\nu), \quad F(\tilde{R}) = \sum_{n=0}^{M-1} b_n T_n(\tilde{R}/\nu). \quad (4.119)$$

On account of the modifications made to the inverse problem in section 4.4.2 we have ensured that $F(\tilde{S})$ has the following properties:

$$0 \leq F(\tilde{S}) \leq 1, \quad \frac{\partial}{\partial \tilde{S}} F(\tilde{S}) \geq 0, \quad \lim_{\tilde{S} \rightarrow -\nu} F(\tilde{S}) \approx 0, \quad \lim_{\tilde{S} \rightarrow \nu} F(\tilde{S}) \approx 1. \quad (4.120)$$

Making use of the fact that

$$T_n(1) = 1, \quad T_n(-1) = (-1)^n \quad (4.121)$$

we can derive the following constrains on \mathbf{c} :

$$\lim_{\tilde{S} \rightarrow -\nu} F(\tilde{S}) = \sum_{n=0}^M c_n T_n(-1) = \sum_{n=0}^M c_n (-1)^n \approx 0, \quad (4.122)$$

$$\lim_{\tilde{S} \rightarrow \nu} F(\tilde{S}) = \sum_{n=0}^M c_n T_n(1) = \sum_{n=0}^M c_n \approx 1. \quad (4.123)$$

Referring to the right-hand plot in figure 4.6 we see that $F(\tilde{S})$ is very flat for extreme values of \tilde{S} . On this basis we can reasonably expect the first and second derivative of $F(\tilde{S})$ to be small at ν and $-\nu$, i.e. that

$$\frac{\partial}{\partial \tilde{S}} F(\tilde{S}) \Big|_{\tilde{S}=-\nu} \approx \frac{\partial}{\partial \tilde{S}} F(\tilde{S}) \Big|_{\tilde{S}=\nu} \approx \frac{\partial^2}{\partial \tilde{S}^2} F(\tilde{S}) \Big|_{\tilde{S}=-\nu} \approx \frac{\partial^2}{\partial \tilde{S}^2} F(\tilde{S}) \Big|_{\tilde{S}=\nu} \approx 0. \quad (4.124)$$

The derivative of $T_n(x)$ is given by

$$\frac{\partial}{\partial x} T_n(x) = n U_{n-1}(x), \quad (4.125)$$

Chapter 4. Probabilistic noise-correction of discrete Fourier transform coefficients where $U_n(x)$ are the Chebyshev polynomials of the second kind ($T_n(x)$ being the first kind). The derivative of $F(\tilde{S})$ is therefore

$$\frac{\partial}{\partial \tilde{S}} F(\tilde{S}) = \sum_{n=0}^M c_n \frac{\partial}{\partial \tilde{S}} T_n(\tilde{S}/\nu) \propto \sum_{n=0}^M c_n n U_{n-1}(\tilde{S}/\nu). \quad (4.126)$$

The $U_n(x)$ have the property that

$$U_{n-1}(1) = n, \quad U_{n-1}(-1) = n(-1)^{n-1}, \quad (4.127)$$

from which we can obtain the following constraints

$$\sum_{n=0}^M n^2 c_n (-1)^{n-1} \approx 0, \quad \sum_{n=0}^M n^2 c_n \approx 0. \quad (4.128)$$

The second derivative of $T_n(x)$ at $x = \pm 1$ can be shown to be

$$\left. \frac{\partial^2}{\partial x^2} T_n(x) \right|_{x=-1} = (-1)^n \frac{(n^4 - n^2)}{3}, \quad \left. \frac{\partial^2}{\partial x^2} T_n(x) \right|_{x=1} = \frac{(n^4 - n^2)}{3}. \quad (4.129)$$

These results yield the final pair of constraints as

$$\sum_{n=0}^{M-1} c_n (-1)^n \frac{(n^4 - n^2)}{3} \approx 0, \quad \sum_{n=0}^{M-1} c_n \frac{(n^4 - n^2)}{3} \approx 0. \quad (4.130)$$

We will now show that it is possible to enforce all of these constraints in a probabilistically motivated way whilst keeping the problem directly soluble for \mathbf{c} . To do so we will construct an approximation of the posterior for \mathbf{c} using only normal distributions. To begin, consider that on account of small numerical errors in \mathbf{b} , we expect that $\mathbf{Ac} \approx \mathbf{b}$ rather than being exactly equal. We will approximate that the uncertainties in all elements of \mathbf{b} are normally distributed, such that the probability of \mathbf{b} given \mathbf{c} is

$$P(\mathbf{b}|\mathbf{c}) \propto \exp \left[-\frac{|\mathbf{Ac} - \mathbf{b}|^2}{2\sigma_b^2} \right]. \quad (4.131)$$

A simplified prior for \mathbf{c} may be constructed using the previously derived constraints for cumulative distributions. First, define a series of length- M column vectors \mathbf{q}_i whose

elements are given by

$$\begin{aligned} (\mathbf{q}_1)_n &= 1, & (\mathbf{q}_2)_n &= (-1)^n, & (\mathbf{q}_3)_n &= n^2 \\ (\mathbf{q}_4)_n &= n^2(-1)^{n-1}, & (\mathbf{q}_5)_n &= \frac{1}{3}(n^4 - n^2), & (\mathbf{q}_6)_n &= \frac{1}{3}(n^4 - n^2)(-1)^n. \end{aligned} \quad (4.132)$$

This allows the summation constraints to be expressed via matrix multiplication as

$$\begin{aligned} \mathbf{q}_1^\top \mathbf{c} &= \sum_{n=0}^{M-1} c_n, & \mathbf{q}_2^\top \mathbf{c} &= \sum_{n=0}^{M-1} c_n (-1)^n, \\ \mathbf{q}_3^\top \mathbf{c} &= \sum_{n=0}^{M-1} n^2 c_n, & \mathbf{q}_4^\top \mathbf{c} &= \sum_{n=0}^{M-1} n^2 c_n (-1)^{n-1}, \\ \mathbf{q}_5^\top \mathbf{c} &= \sum_{n=0}^{M-1} \frac{1}{3} c_n (n^4 - n^2), & \mathbf{q}_6^\top \mathbf{c} &= \sum_{n=0}^{M-1} \frac{1}{3} c_n (n^4 - n^2) (-1)^n. \end{aligned} \quad (4.133)$$

As before, we will approximate that the uncertainty in each constraint is normal so that the prior is given by

$$P(\mathbf{c}) \propto \exp \left[-\frac{|\mathbf{q}_1^\top \mathbf{c} - 1|^2}{2\sigma_1^2} - \sum_{n=2}^6 \frac{|\mathbf{q}_n^\top \mathbf{c}|^2}{2\sigma_n^2} \right]. \quad (4.134)$$

The posterior for \mathbf{c} can then be obtained via Bayes' theorem as $P(\mathbf{c}|\mathbf{b}) \propto P(\mathbf{b}|\mathbf{c})P(\mathbf{c})$:

$$P(\mathbf{c}|\mathbf{b}) \propto \exp \left[-\frac{|\mathbf{A}\mathbf{c} - \mathbf{b}|^2}{2\sigma_b^2} - \frac{|\mathbf{q}_1^\top \mathbf{c} - 1|^2}{2\sigma_1^2} - \sum_{n=2}^6 \frac{|\mathbf{q}_n^\top \mathbf{c}|^2}{2\sigma_n^2} \right]. \quad (4.135)$$

The objective is now to determine the vector $\hat{\mathbf{c}}$ which maximises the posterior. This can be done easily by differentiating the natural log of the posterior to find its maximum:

$$\frac{\partial}{\partial \mathbf{c}} \ln P(\mathbf{c}|\mathbf{b}) \propto -\frac{\partial}{\partial \mathbf{c}} \left(\frac{|\mathbf{A}\mathbf{c} - \mathbf{b}|^2}{2\sigma_b^2} + \frac{|\mathbf{q}_1^\top \mathbf{c} - 1|^2}{2\sigma_1^2} + \sum_{n=2}^6 \frac{|\mathbf{q}_n^\top \mathbf{c}|^2}{2\sigma_n^2} \right). \quad (4.136)$$

Carrying out the differentiation and setting the expression equal to zero yields

$$\frac{\mathbf{A}^\top (\mathbf{A}\hat{\mathbf{c}} - \mathbf{b})}{2\sigma_b^2} + \frac{\mathbf{q}_1 (\mathbf{q}_1^\top \hat{\mathbf{c}} - 1)}{2\sigma_1^2} + \sum_{n=2}^6 \frac{\mathbf{q}_n \mathbf{q}_n^\top \hat{\mathbf{c}}}{2\sigma_n^2} = 0, \quad (4.137)$$

which may be solved for $\hat{\mathbf{c}}$ to obtain

$$\hat{\mathbf{c}} = \arg \max_{\mathbf{c}} \left[P(\mathbf{c}|\mathbf{b}) \right] = \left(\frac{\mathbf{A}^\top \mathbf{A}}{\sigma_b^2} + \sum_{n=1}^6 \frac{\mathbf{q}_n \mathbf{q}_n^\top}{\sigma_n^2} \right)^{-1} \left(\frac{\mathbf{A}^\top \mathbf{b}}{\sigma_b^2} + \frac{\mathbf{q}_1}{\sigma_1^2} \right). \quad (4.138)$$

Finally let $\hat{F}(\tilde{S})$ be the estimate of $F(\tilde{S})$ given by

$$\hat{F}(\tilde{S}) = \sum_{n=0}^{M-1} \hat{c}_n T_n(\tilde{S}/\nu) \quad (4.139)$$

In order to test this method $P(S)$ was taken to be the modified log-normal distribution defined in section 4.4.1 (making $F(\tilde{S})$ a cumulative normal distribution). $F(\tilde{R})$ was calculated numerically then used to obtain the coefficients \mathbf{b} , which were used to obtain $\hat{\mathbf{c}}$. The resulting $\hat{F}(\tilde{S})$ is shown in the left-hand plot of figure 4.8.

We see that although the series shows the correct behaviour at the two ends of the domain, the accuracy of the estimate everywhere else is very poor. This is to be expected, because the prior only constrains the value of $F(\tilde{S})$ and its first derivative at $-\nu$ and ν - it does nothing to limit the total absolute value of the coefficients.

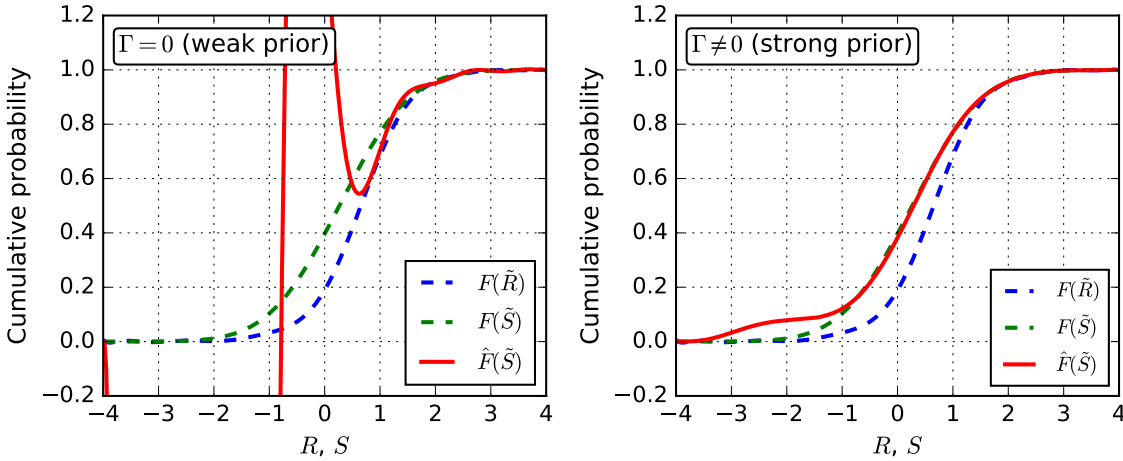


Figure 4.8: Results of estimating $F(\tilde{S})$ using the maximum of two versions of an approximate posterior for \mathbf{c} . For this test $P(S)$ was taken to be the modified log-normal distribution in (4.69) with parameters $\mathcal{U} = 0.4$ and $w = 1$. The errors used for the priors were $\sigma_n = 0.005$ for all n , and $\sigma_c = 0.75$.

To address this, we can impose an assumption that because $F(\tilde{S})$ and $F(\tilde{R})$ are similar in form, \mathbf{c} should not deviate significantly from \mathbf{b} . Ideally we would set a prior for each c_i that is flat in a region around b_i and zero elsewhere, but for now we will continue to use normal distributions in order to preserve the analytic solution for $\hat{\mathbf{c}}$.

The strengthened version of the prior is

$$P(\mathbf{c}) \propto \exp \left[-\frac{|\mathbf{\Gamma}(\mathbf{c} - \mathbf{b})|^2}{2\sigma_c^2} - \frac{|\mathbf{q}_1^\top \mathbf{c} - 1|^2}{2\sigma_1^2} - \sum_{n=2}^6 \frac{|\mathbf{q}_n^\top \mathbf{c}|^2}{2\sigma_n^2} \right], \quad (4.140)$$

4.4. Estimating the prior distribution $P(S)$ where $\mathbf{\Gamma}$ is a diagonal $M \times M$ matrix with $\Gamma_{nn} = \sqrt{n}$. $\mathbf{\Gamma}$ serves to scale σ_c^2 (how much we expect \mathbf{c} to deviate from \mathbf{b}) to smaller values for higher-order coefficients to account for the fact that their magnitude falls off with n . Repeating the derivation of $\hat{\mathbf{c}}$ from earlier we find that

$$\hat{\mathbf{c}} = \left(\frac{\mathbf{A}^\top \mathbf{A}}{\sigma_b^2} + \frac{\mathbf{\Gamma}^\top \mathbf{\Gamma}}{\sigma_c^2} + \sum_{n=1}^6 \frac{\mathbf{q}_n \mathbf{q}_n^\top}{\sigma_n^2} \right)^{-1} \left(\frac{\mathbf{A}^\top \mathbf{b}}{\sigma_b^2} + \frac{(\mathbf{\Gamma}^\top \mathbf{\Gamma}) \mathbf{b}}{\sigma_c^2} + \frac{\mathbf{q}_1}{\sigma_1^2} \right). \quad (4.141)$$

The results obtained using the strengthened prior are shown in the right-hand plot of figure 4.8. We see that there is a dramatic improvement in performance over the weaker prior, particularly for $\tilde{S} > 0$ where the estimation is very good. In this case the ratio of the mean absolute difference of \mathbf{c} and $\hat{\mathbf{c}}$ to the mean absolute value of \mathbf{c} was around 7%.

Although these results are promising, the simplified prior used to obtain them introduces an unwanted bias into $\hat{\mathbf{c}}$. We now investigate whether using $\hat{\mathbf{c}}$ as an initial guess, an improved solution can be obtained from a non-linear optimisation problem resulting from a switch to a less-biasing prior in which we are not limited to using only normal distributions.

4.4.6 Estimating \mathbf{c} via non-linear optimisation

We observed in the previous section that inclusion of the $|\mathbf{\Gamma}(\mathbf{c} - \mathbf{b})|^2$ term in the prior was necessary for obtaining physically sensible solutions. This term does however introduce an unwanted bias into the posterior distribution, so we now seek to replace it with a new term which enforces the inequality constraints given in (4.120) without introducing bias. To do so we evaluate the series and its first derivative at a range of points across the domain of orthonormality. Accordingly define a series of points x_n with length L that spans $[-\nu, \nu]$:

$$x_n = \nu \left(2 \left(\frac{n-1}{L-1} \right) - 1 \right). \quad (4.142)$$

Now define the following matrices

$$\mathbf{T} = \begin{bmatrix} T_0(x_1/\nu) & \cdots & T_{M-1}(x_1/\nu) \\ \vdots & \ddots & \vdots \\ T_0(x_L/\nu) & \cdots & T_{M-1}(x_L/\nu) \end{bmatrix}, \quad \mathbf{U} = \begin{bmatrix} 0 & \cdots & (M-1)U_{M-2}(x_1/\nu) \\ \vdots & \ddots & \vdots \\ 0 & \cdots & (M-1)U_{M-2}(x_L/\nu) \end{bmatrix}. \quad (4.143)$$

This allows the calculation of $F(\tilde{S})$ and $F'(\tilde{S})$ (the first derivative) as the following matrix products:

$$\mathbf{T}\mathbf{c} = \begin{bmatrix} \sum_{n=0}^{M-1} c_n T_n(x_1/\nu) \\ \sum_{n=0}^{M-1} c_n T_n(x_2/\nu) \\ \vdots \\ \sum_{n=0}^{M-1} c_n T_n(x_L/\nu) \end{bmatrix} = \begin{bmatrix} F_{\tilde{S}}(x_1) \\ F_{\tilde{S}}(x_2) \\ \vdots \\ F_{\tilde{S}}(x_L) \end{bmatrix}, \quad (4.144)$$

$$\mathbf{U}\mathbf{c} = \begin{bmatrix} \sum_{n=0}^{M-1} n c_n U_{n-1}(x_1/\nu) \\ \sum_{n=0}^{M-1} n c_n U_{n-1}(x_L/\nu) \\ \vdots \\ \sum_{n=0}^{M-1} n c_n U_{n-1}(x_L/\nu) \end{bmatrix} = \begin{bmatrix} F'_{\tilde{S}}(x_1) \\ F'_{\tilde{S}}(x_2) \\ \vdots \\ F'_{\tilde{S}}(x_L) \end{bmatrix}. \quad (4.145)$$

Because we are using a finite Chebyshev series we cannot completely exclude all \mathbf{c} which violate the inequality conditions in (4.120). Instead define a new term \mathcal{H} which is zero provided that the inequalities are satisfied at all x_n and quadratic otherwise:

$$\mathcal{H} = \sum_{i=1}^L \frac{1}{2\sigma_T^2} \left\{ \begin{array}{ll} (\mathbf{T}\mathbf{c})_i^2 & : 0 > (\mathbf{T}\mathbf{c})_i \\ 0 & : 0 \leq (\mathbf{T}\mathbf{c})_i \leq 1 \\ ((\mathbf{T}\mathbf{c})_i - 1)^2 & : 1 < (\mathbf{T}\mathbf{c})_i \end{array} \right\} + \frac{1}{2\sigma_U^2} \left\{ \begin{array}{ll} (\mathbf{U}\mathbf{c})_i^2 & : 0 > (\mathbf{U}\mathbf{c})_i \\ 0 & : 0 \leq (\mathbf{U}\mathbf{c})_i \end{array} \right\}. \quad (4.146)$$

Including $e^{-\mathcal{H}}$ as a multiplicative factor in the prior now allows the posterior to be expressed as

$$P(\mathbf{c}|\mathbf{b}) \propto \exp[-(\mathcal{L} + \mathcal{H})] \quad (4.147)$$

where

$$\mathcal{L} = \frac{|\mathbf{A}\mathbf{c} - \mathbf{b}|^2}{2\sigma_b^2} + \frac{|\mathbf{q}_1^\top \mathbf{c} - 1|^2}{2\sigma_1^2} + \sum_{n=2}^6 \frac{|\mathbf{q}_n^\top \mathbf{c}|^2}{2\sigma_n^2}. \quad (4.148)$$

By multiplying out the squares and dropping terms with no dependence on \mathbf{c} , it can be shown that

$$\mathcal{L} = \mathbf{c}^\top (\mathbf{A}^* \mathbf{c} - \mathbf{b}^*) \quad (4.149)$$

where

$$\mathbf{A}^* = \frac{\mathbf{A}^\top \mathbf{A}}{2\sigma_b^2} + \sum_{n=1}^6 \frac{\mathbf{q}_n \mathbf{q}_n^\top}{2\sigma_n^2}, \quad \mathbf{b}^* = \frac{\mathbf{A}^\top \mathbf{b}}{\sigma_b^2} + \frac{\mathbf{q}_1}{\sigma_1^2}. \quad (4.150)$$

This form drastically reduces the number of matrix operations needed to calculate \mathcal{L} , and as \mathbf{A}^* and \mathbf{b}^* have no \mathbf{c} dependence they may be pre-calculated and stored.

Additionally, rather than determining only the maximum of the posterior for \mathbf{c} as before, we will generate a sample from the posterior using Markov-chain Monte-Carlo techniques in order to extract uncertainties on the reconstruction of $F(\tilde{S})$ and subsequently $E[\tau]$. A purpose-written Gibbs sampler was used to generate a Markov chain of length 2.2×10^6 , and the sample with the largest associated posterior probability was taken as the MAP estimate. To determine uncertainties, the first 2×10^5 samples were discarded as burn-in and the remaining were thinned by a factor of 20 yielding an uncorrelated sample of size 10^5 . Of those, the 5% with the lowest associated posterior probabilities were discarded, leaving only samples lying in the 95% credibility region. Both $F(\tilde{S})$ and $E[\tau]$ were computed for each of these samples in order to produce a 95% credibility envelope - these results are shown in figure 4.9.

We see that although $F(\tilde{S})$ lies outside of the error estimate for some negative values of \tilde{S} , $E[\tau]$ is well inside the error estimate and lies close to the MAP estimate. This is not surprising due to the fact that $\tilde{S} = \ln S$, and that $P(R|S) \rightarrow 0$ as $R, S \rightarrow 0$. Thus negative values of \tilde{S} correspond to small values of S where $P(R|S)$ is near zero, and therefore make only a small contribution toward the calculated values of $E[\tau]$.

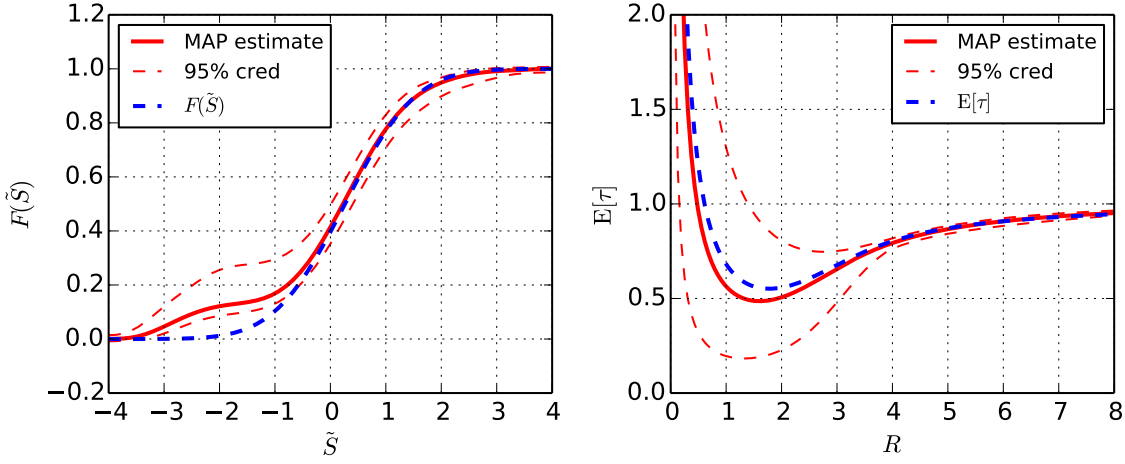


Figure 4.9: Summary of results from Markov chain Monte-Carlo sampling of the posterior for \mathbf{c} . The left plot compares the MCMC estimate of $F(\tilde{S})$ with its true values, and the right-hand plot compares the MCMC estimate of $E[\tau]$ with its true values.

A long chain was necessary in order for the MCMC estimate to properly converge, likely due to the shape of the posterior surface being extremely complex. This arises due to the multiple constraints expressed as summations over the \mathbf{c} . It is generally not possible to change only one or two elements of \mathbf{c} in such a way that these constraints continue to be met as before. Instead precise simultaneous changes to most, if not all, elements of \mathbf{c} are needed to move to a new solution which meets the constraints. This requires the Markov chain to make very small steps, and consequently require many steps in order to fully explore the posterior. The computational cost of the large number of required steps is offset significantly however by the low cost each posterior evaluation, due mainly to the mostly linear nature of the calculation.

4.4.7 Prior-evidence equivalence approximation

We noted in section 4.4.3.1 that for small values of \mathcal{U}

$$P(S) \approx \int_0^\infty \delta(S - R)P(R) dR = \hat{P}(S) \quad (4.151)$$

In this section we examine how the validity of using $\hat{P}(S)$ shown above as an approximation of $P(S)$ changes as a function of \mathcal{U} . As we've been referring to $P(S)$ as the prior, the corresponding nomenclature for $P(R)$ would be the 'evidence' - as such we

4.4. Estimating the prior distribution $P(S)$ will refer to $\hat{P}(S)$ as the prior-evidence equivalence approximation. The magnitude correction effectively replaces each value of R with $E[S]$, where

$$E[S] = \int_0^\infty \frac{SP(R|S)P(S)}{\int_0^\infty P(R|S)P(S) dS} dS. \quad (4.152)$$

The absolute size of the correction to R is therefore $|R - E[S]|$, and the average absolute correction size can be obtained through integration as

$$\int_0^\infty P(R) |E[S] - R| dR. \quad (4.153)$$

Let $\hat{E}[S]$ be the approximate expectation of S obtained by replacing $P(S)$ with $\hat{P}(S)$ in (4.152). The mean absolute error in the correction is therefore

$$\int_0^\infty P(R) |E[S] - \hat{E}[S]| dR. \quad (4.154)$$

We may now define the mean absolute fractional correction error as the ratio of (4.154) to (4.153):

$$\text{MAFCE} = \left(\int_0^\infty P(R) |E[S] - \hat{E}[S]| dR \right) / \left(\int_0^\infty P(R) |E[S] - R| dR \right) \quad (4.155)$$

If the MAFCE is small, then making the prior-evidence equivalence approximation will still result in a reduction of the noise, although most likely a less significant reduction. Calculations of the MAFCE for the log-normal test prior as a function of \mathcal{U} and w are shown in figure 4.10. As expected we see that for small values of \mathcal{U} the MAFCE tends toward zero, but also that its behaviour can be strongly dependent on the shape of the prior, which is altered here by varying w .

4.4.8 Comparison of prior estimation techniques

The test cases used to develop the various techniques for estimating the prior $P(S)$ in this section are not sufficient to properly understand their effectiveness. To do so a full calculation of the correction factors using an estimated prior is required. Only then can we see how inaccuracies in the estimate of $P(S)$ translate to errors in the correction

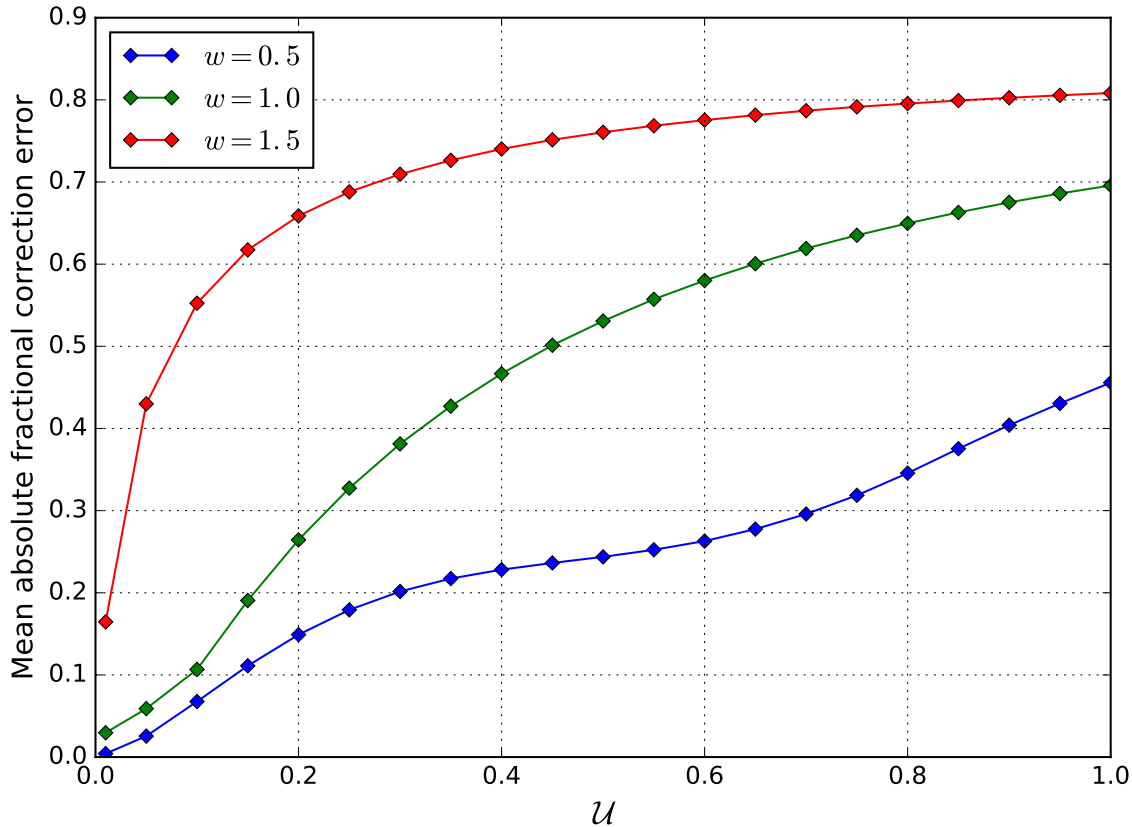


Figure 4.10: Plots of the mean absolute fractional correction error defined in (4.155) for the log-normal test prior (from (4.69)) as a function of U and w .

factors and presumably a loss in correction performance. Testing on real data is also important to demonstrate that the estimation techniques produce acceptable results when $P(R)$ is not smooth and unimodal. The testing necessary to quantitatively compare the prior estimation techniques is presented later in this chapter.

4.5 Demonstration of magnitude correction method

Now we bring together the work in previous sections to demonstrate the complete procedure and calculations necessary in order to obtain a noise-corrected signal. The data to which the correction will be applied is the audio signal introduced in section 4.4.1.

4.5.1 Inference of σ

We have thus far assumed that σ is a known constant, but in reality it must be inferred from the measured signal. The best way to determine σ is by analysing an area of the frequency space which contains little or no power from the true signal, assuming such a region exists. We could assume that the true Fourier magnitude s in the Rice distribution is zero, in which case we obtain the Rayleigh distribution. This yields an analytic posterior for σ (assuming a flat prior).

Although there are typically regions of the frequency space where the true signal power is small compared to the noise power, it is unlikely that there will be a region where it is zero. Instead we suggest selecting a set of $|z_k|$ values from the region with the lowest power density (because the noise power is constant with frequency this is necessarily the area which has the least true signal power) and assume that over this region the true signal power can be approximated as some constant ρ . Letting \mathcal{D} represent the chosen set of $|z_k|$, the likelihood is a product of Rice distributions:

$$P(\mathcal{D}|\rho, \sigma) = \prod_k P(|z_k||\rho, \sigma) = \prod_k \frac{|z_k|}{\sigma^2} \exp\left[-\frac{\rho^2 + |z_k|^2}{2\sigma^2}\right] I_0\left(\frac{|z_k|\rho}{\sigma^2}\right). \quad (4.156)$$

The joint distribution for σ and ρ is given by Bayes' theorem as

$$P(\sigma, \rho|\mathcal{D}) = \frac{P(\mathcal{D}|\rho, \sigma)P(\rho, \sigma)}{P(\mathcal{D})}, \quad (4.157)$$

and the marginal distribution for σ can then be obtained by integration as follows

$$P(\sigma|\mathcal{D}) = \int_0^\infty P(\sigma, \rho|\mathcal{D}) d\rho = \frac{1}{P(\mathcal{D})} \int_0^\infty P(\mathcal{D}|\rho, \sigma)P(\rho, \sigma) d\rho. \quad (4.158)$$

To infer σ for this demonstration, $|z_k|$ values from were taken from the region of the frequency space between 17 kHz and 18 kHz (visible in figure 4.5) and the prior $P(\sigma, \rho)$ was taken to be flat. The calculated joint posterior $P(\sigma, \rho|\mathcal{D})$ is shown in the left-hand plot of figure 4.11 and the marginal distribution $P(\sigma|\mathcal{D})$ in the right-hand plot. We see that there exists a non-trivial amount of probability density in the region where

Chapter 4. Probabilistic noise-correction of discrete Fourier transform coefficients $\rho > 0$, which then influences the shape of $P(\sigma|\mathcal{D})$ - a feature which would have been missed if ρ was assumed to be zero.

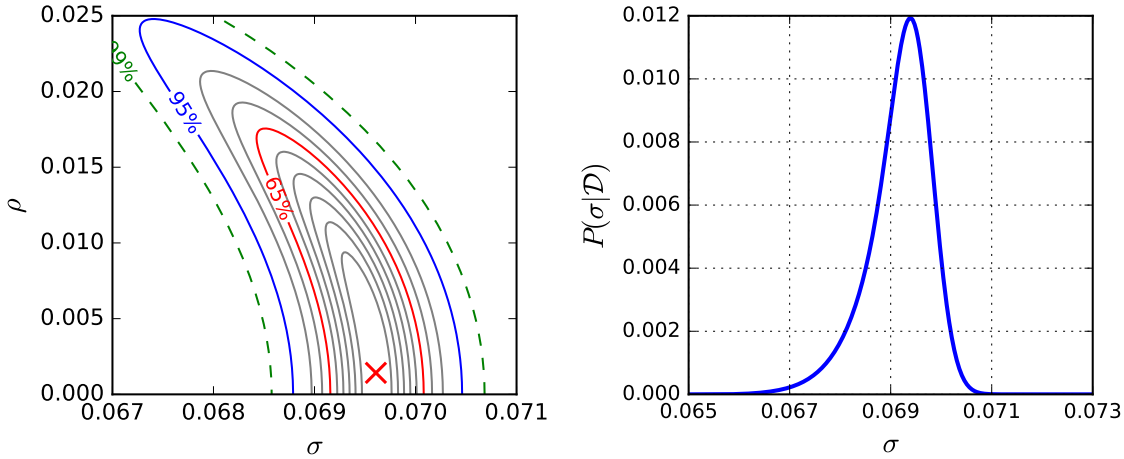


Figure 4.11: (left): Plot of the joint posterior $P(\sigma, \rho|\mathcal{D})$ calculated for the test data. The global maximum is marked with a cross, and the distribution is described using credible region contouring. (right): Plot of the marginal distribution $P(\sigma|\mathcal{D})$ obtained from integrating over the posterior in the left plot.

If the uncertainty in σ is very small we can for simplicities sake use the mode of $P(\sigma|\mathcal{D})$ as a single-value estimate and treat it as a known constant. However for a less well-determined σ we may wish to calculate the correction factors $E[\tau]$ in a way which accounts for this uncertainty. This can be achieved by calculating $E[s]/|z|$ rather than $E[S]/R$, which may be expressed as

$$\begin{aligned}
 E[\tau] &= \frac{E[s]}{|z|} = \frac{1}{|z|} \int_0^\infty s P(s|\mathcal{D}, |z|) ds \\
 &= \frac{1}{|z| P(|z|)} \int_0^\infty s \left(\int_0^\infty P(|z||s, \sigma) P(s|\sigma) P(\sigma|\mathcal{D}) d\sigma \right) ds.
 \end{aligned}
 \tag{4.159}$$

Note however that this contains the term $P(s|\sigma)$, which to calculate requires that we obtain many estimates of the prior distribution as a function of σ . Doing so requires that the prior estimation process is automatic (i.e. no manual analysis is involved), robust and computationally inexpensive. Through a combination of the techniques developed in section 4.4 it should be possible to develop an algorithm which meets these criteria - this is beyond the scope of this thesis but may be the subject of further work. In light of this, we will continue by using the single-value estimate $\hat{\sigma} = 0.694$, taken from the mode of the marginal distribution shown in figure 4.11.

4.5.2 Selecting the pass-band region of frequency space

We noted in the introduction to this chapter that one of the motivations for this work was to address the problem of noise remaining in the pass-band after the application of a frequency-based filter. Here we discuss probabilistic approach to selecting which areas of the frequency space can be filtered out and which are to be magnitude-corrected. As mentioned in the previous section, in an area where there is no true signal power the measured magnitudes have the following Rayleigh distribution

$$P(|z||\sigma) = \frac{|z|}{\sigma^2} \exp\left[-\frac{|z|^2}{2\sigma^2}\right]. \quad (4.160)$$

Now suppose we were to calculate the likelihood that the $|z_k|$ are Rayleigh-distributed in a given window of frequency space defined by $f_0 \pm \delta f$. Letting the set of magnitudes in this window be represented by \mathcal{W} we may write

$$P(\mathcal{W}|\sigma) = \prod_k P(|z_k||\sigma). \quad (4.161)$$

The conditionality on σ can be removed by using $P(\sigma|\mathcal{D})$ (which we calculated in the previous section) and marginalisation as follows.

$$P(\mathcal{W}) = \int_0^\infty P(\mathcal{W}, \sigma|\mathcal{D}) d\sigma = \int_0^\infty P(\mathcal{W}|\sigma)P(\sigma|\mathcal{D}) d\sigma. \quad (4.162)$$

By considering how $P(\mathcal{W})$ varies with f_0 we can identify which regions of the probability space are not well described by the Rayleigh distribution, indicating that these areas should not be filtered out because they contain meaningful amounts of true signal magnitude. A plot of $\ln(P(\mathcal{W}))$ versus f_0 for the test data is given in figure 4.12. We see that the likelihood starts to fall very rapidly at around 11 kHz, so a cut-off of 12 kHz was chosen for the low-pass filter to ensure no useful signal information was discarded. The distribution of the R_k can now be estimated from the non-zero magnitudes remaining in the pass-band in order to obtain the correction factors.

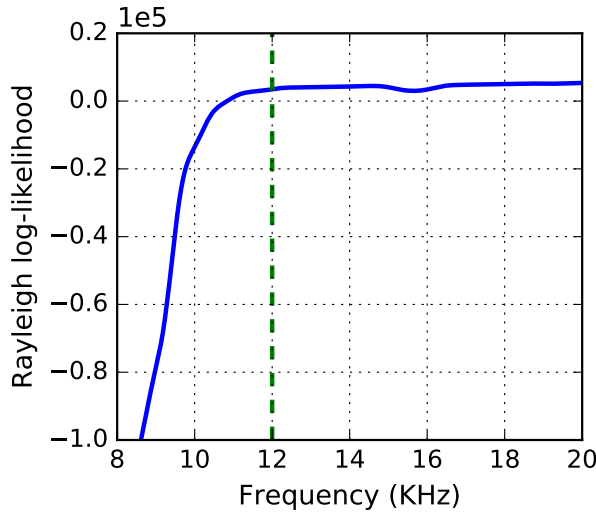


Figure 4.12: Plot of the likelihood $P(\mathcal{W})$ from (4.162) as a function of the window central frequency f_0 . The window width used here is 1 kHz. The dashed line indicates the chosen cut-off for the low-pass filter based on the results.

4.5.3 Calculating the correction factors

Results from estimating the prior and the subsequent calculation of the correction factors $E[\tau_k]$ are shown in figure 4.13. Following our observation in section 4.4.1 that the PDF of the Fourier magnitudes is represented particularly well by a sum of log-normal distributions, a continuous estimate of $P(\tilde{R})$ was obtained by fitting a sum of normal distributions to the sample of \tilde{R} . The residual plot for the fit given in the results demonstrates that this approach is highly effective, the largest deviation between the fit and the data being only ~ 0.002 . This accuracy was obtained using a total of eight normal distributions, but the majority of these added only small refinements - we found that a maximum deviation of ~ 0.003 could be achieved using only three normal distributions.

The analytic representation of $P(\tilde{R})$ was then used to generate an estimate of $P(\tilde{S})$ using the iterative Bayesian approach developed in section 4.4.3. The estimate converged after around 30 iterations, confirming that it satisfies the forward transform integral equation. We found that the estimated prior produced a correction function $E[\tau]$ with the expected limiting behaviour that was derived using simple analytic prior models in sections 4.3.3 and 4.3.4 - namely that $E[S]/R \rightarrow 1$ as $R \rightarrow \infty$ and $\frac{\partial}{\partial R} E[S] \rightarrow 0$ as $R \rightarrow 0$. The fact that $E[S]$ has a non-zero minimum value limits the distribution of

4.5. Demonstration of magnitude correction method corrected magnitudes to have zero density below this value. We see the consequences of this in the lower-right plot of figure 4.13, where the distribution of the log-magnitudes after the correction has a sharp, skewed peak because all magnitudes with a value lower than the minimum in $E[S]$ have been moved to or above the minimum.

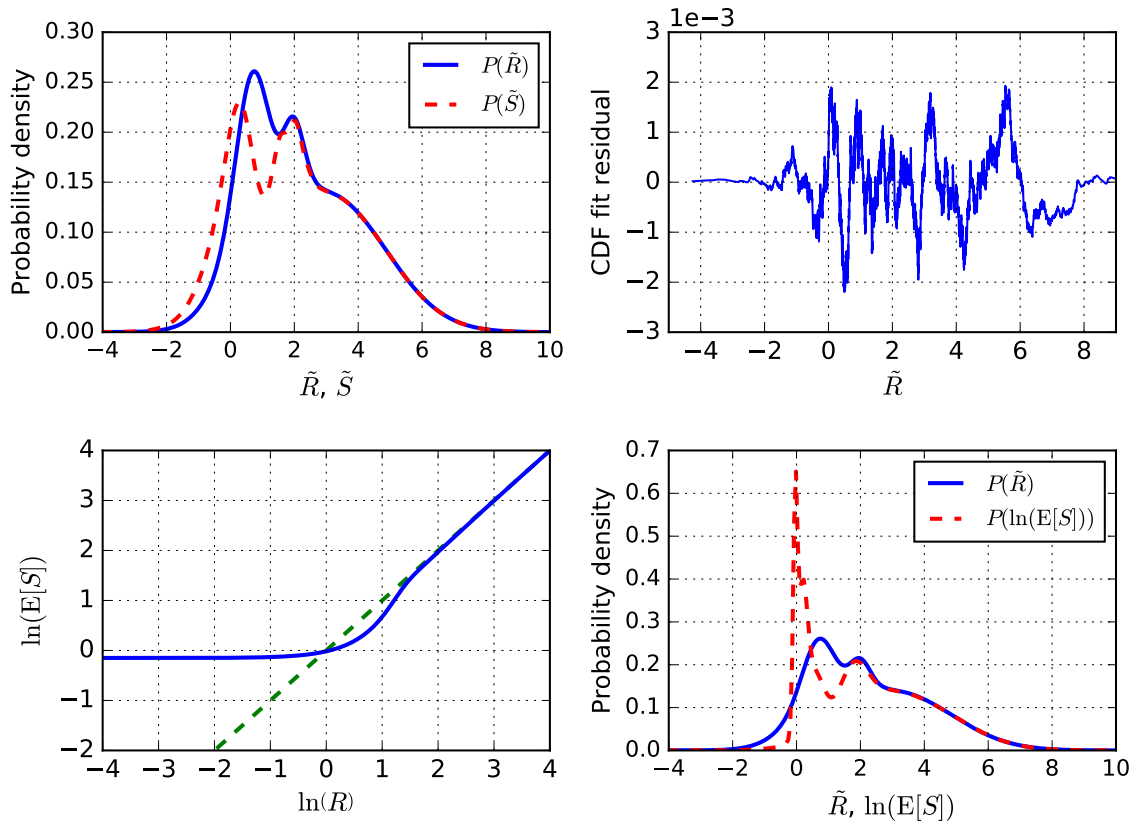


Figure 4.13: (top-left): The $P(\tilde{R})$ measured directly from the test data and the corresponding estimate of $P(\tilde{S})$ obtained using the iterative approach described in section 4.4.3. (top-right): The difference between the sample estimate of the CDF for \tilde{R} and the fit using a series of normal distribution CDFs. (bottom-left): $E[S]$ calculated using the estimated prior. (bottom-right): Comparison between the corrected and un-corrected Fourier magnitude distributions.

4.5.4 Demonstration of reduction in magnitude errors

In order to demonstrate that this correction procedure does in fact result in an overall reduction in the error of the Fourier magnitudes we present the results shown in figure 4.14. Gaussian noise was added to the audio test data, with the resulting signal having a noise-level of $\mathcal{U} = 0.5$. The original and noisy signals yielded a set of s_k and $|z_k|$ values respectively, allowing the calculation of the corresponding correction factors $\tau_k = s_k/|z_k|$. These τ_k are shown in the left-hand plot, along with the corresponding

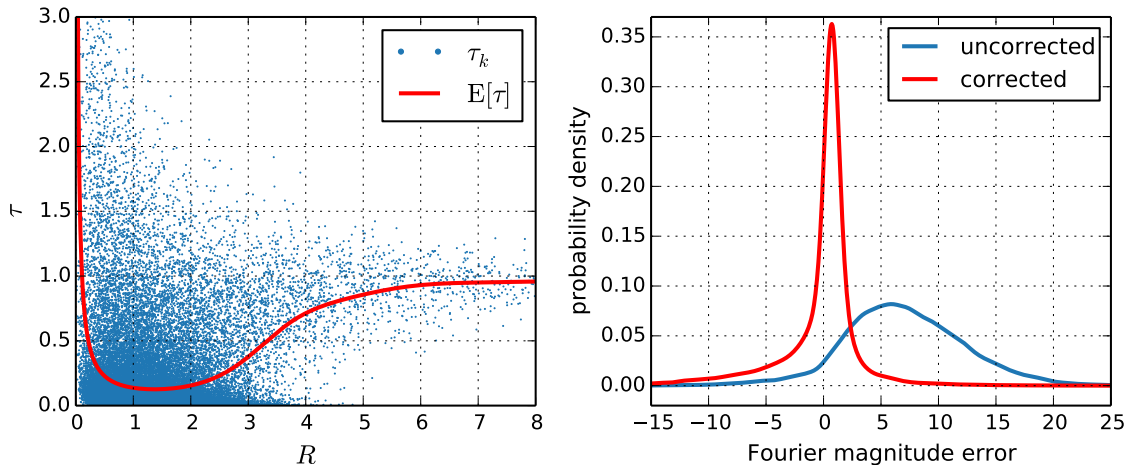


Figure 4.14: (left): Point-plot of the correction factors τ_k for the test data with added Gaussian noise, with the corresponding correction curve $E[\tau]$ overlaid. (right): Probability distributions for the ‘uncorrected’ magnitude errors $|z_k| - s_k$ and ‘corrected’ errors $E[\tau_k]|z_k| - s_k$.

curve of $E[\tau]$ calculated as part of the correction procedure. This plot is a useful visualisation of *why* this method reduces the overall magnitude error - the average distance between the τ_k and the $E[\tau]$ is lower than that between the τ_k and the $\tau = 1$ line, which would correspond to no correction.

The ‘error’ in the measured magnitudes $|z_k|$ introduced by the noise is given by the difference $|z_k| - s_k$. The corresponding error in the corrected magnitudes is therefore given by $E[\tau_k]|z_k| - s_k$. By comparing the distribution of the magnitude errors before and after correction, shown the right-hand plot, we are able to quantify the effect of the correction. For this particular case, we find that the mean of the corrected errors is much closer to zero with $\mu = -0.24$ versus the uncorrected mean of $\mu = 6.98$. The square-root of the raw second moment provides a useful quantification of the overall level of error in the magnitudes. In the uncorrected case we find a value of $\sqrt{\mu_2} = 8.76$ and one of $\sqrt{\mu_2} = 3.73$ in the corrected case - a 57% reduction.

4.6 Correction performance testing

In this section we investigate the performance of the magnitude correction technique by applying it to a variety of simulated datasets. These datasets were generated using the audio signal that was the subject of the demonstration correction in the previous

4.6. Correction performance testing section. This signal was low-pass filtered with the cut-off at 12 kHz and stored to be used as the true series \bar{G}_n . Various ‘measured’ signals were then generated by adding different levels of Gaussian noise to the true signal.

Initially we examine the ideal case where the correction is calculated using the exact (usually unknown) prior $P(S)$. Performance resulting from estimated priors is discussed later in this section.

4.6.1 Investigating ideal correction performance

In section 4.3.5 we defined the following initial and corrected noise levels (δ_i and δ_c respectively) as

$$\delta_i = \sqrt{\frac{1}{N} \sum_{n=0}^{N-1} (G_n - \bar{G}_n)^2} = \sqrt{\frac{1}{N} \sum_{n=0}^{N-1} \mathcal{E}_n^2}, \quad \delta_c = \sqrt{\frac{1}{N} \sum_{n=0}^{N-1} (\hat{G}_n - \bar{G}_n)^2}. \quad (4.163)$$

As we have taken the noise series \mathcal{E}_n to be normally distributed with zero mean, the initial noise δ_i is an estimator of the time-domain standard deviation because it is equal to the root-mean-square value of the $\{\mathcal{E}_n\}$. In all testing we found that the difference between the true and corrected signals $\hat{G}_n - \bar{G}_n$ was also normally distributed, which supports the assumption of CLT validity made in equation (4.25). Additionally this means that δ_c is an estimator of the *corrected* time-domain standard deviation. The ‘fractional noise reduction’ δ_c/δ_i will be used throughout this section as a metric for the performance of the correction technique.

It is also important to study how δ_c/δ_i varies with \mathcal{U} , the level of noise in the signal. Comparing the definitions of δ_i above and \mathcal{U} from (4.61) we see they are related as follows

$$\mathcal{U} = \delta_i \left(\frac{1}{N} \sum_{n=0}^{N-1} \bar{G}_n^2 \right)^{-\frac{1}{2}}. \quad (4.164)$$

The fractional noise reduction was calculated as a function of \mathcal{U} for 200 separate simulated datasets (generated using different sets of Gaussian noise) and the results are given in figure 4.15. The noise reduction was calculated for the magnitude correction and a low-pass filter, and then for the low-pass filter only. We see that in the limit

Chapter 4. Probabilistic noise-correction of discrete Fourier transform coefficients where $\mathcal{U} \rightarrow 0$ the additional noise reduction from the magnitude correction vanishes leaving only that from the low-pass filter. The variation in δ_c/δ_i over the different simulated datasets was found to be normal distributed but with a small standard deviation, as shown by the right-hand plot. This is to be expected given the relatively large number data points (2^{17}) in the audio signal, which should ensure that any random variation is small.

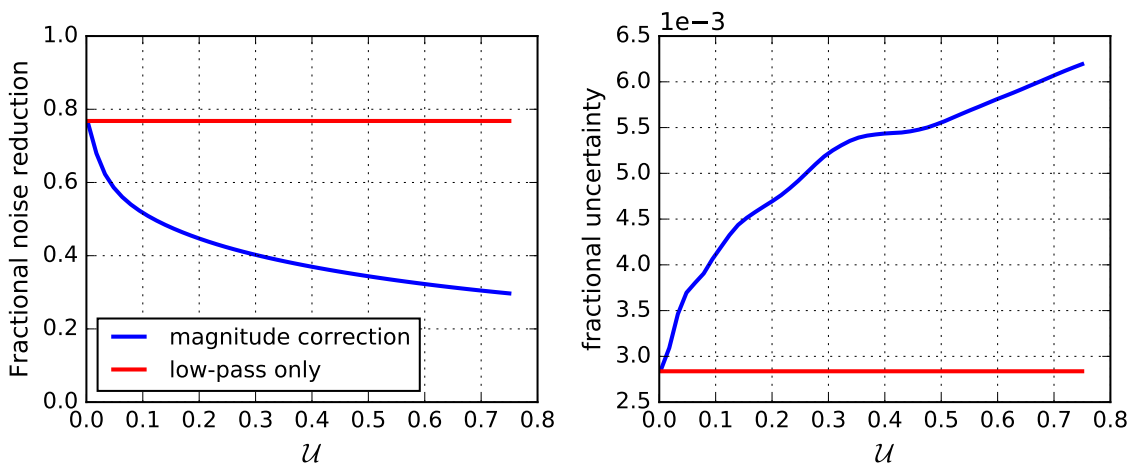


Figure 4.15: (left): Plot of the overall noise reduction resulting from both a low-pass filter, and the same filtering plus the probabilistic magnitude correction. (right): The variation in the correction performance observed from by calculating the correction for 200 different sets of applied Gaussian noise.

4.6.2 Quantitative comparison of prior estimation techniques

All that remains is to compare the ideal correction performance with that obtained when the prior is estimated using the techniques developed in section 4.4, as it must be in any applied case. Both the Bayesian iterative prior approximation (BIPA) and the prior-evidence equivalence approximation (PEEA) proved to be robust and give smoothly-varying performance as a function of \mathcal{U} as shown in figure 4.16. It might have been expected that in the high-noise limit the prior estimates would break down and begin to lose correction performance, but we see the estimates continue to yield improved performance with increasing \mathcal{U} . The BIPA estimates performs better than the PEEA estimate, which we would certainly expect given that PEEA is the trivial approximation (only the assumption of a flat prior being more trivial). The performance results for the linearisation prior estimation approach are not given here because

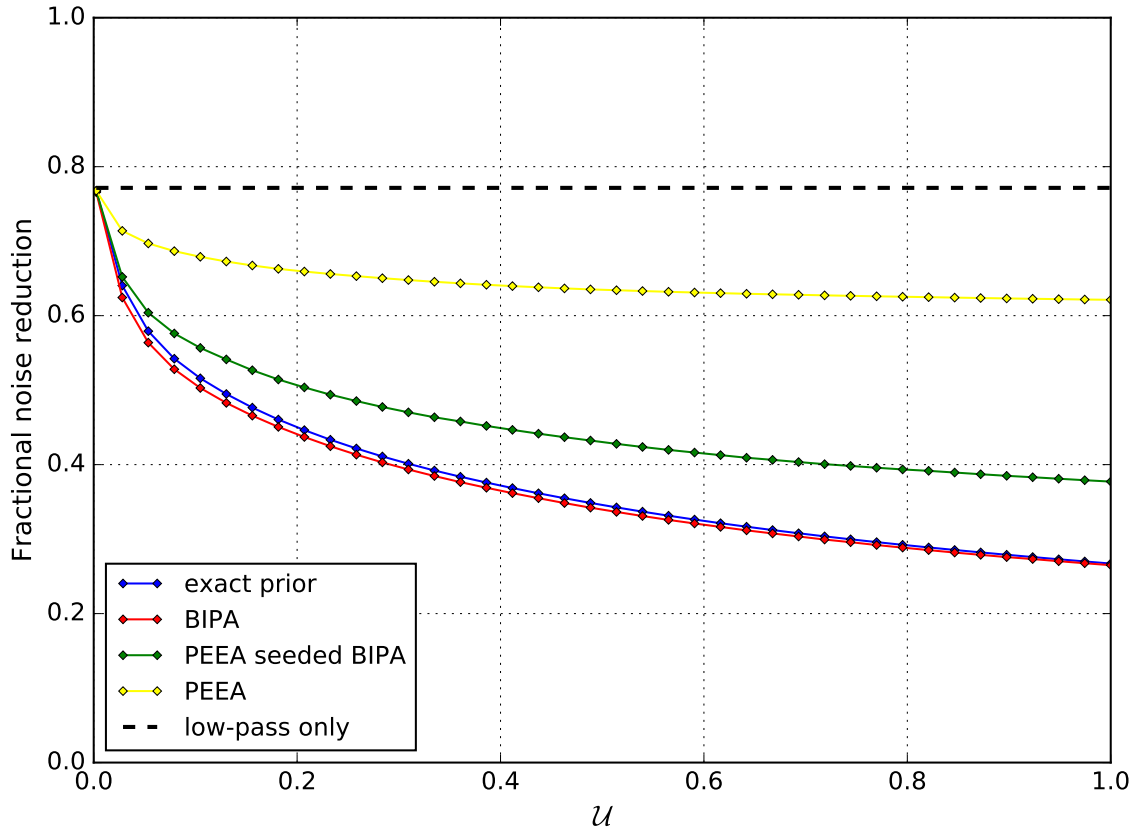


Figure 4.16: Comparison of the correction performance when using estimated priors versus the ideal case with the exact prior. Here BIPA is the Bayesian iterative prior approximation and PEEA is the prior-evidence equivalence approximation.

in testing it failed to produce robust results - performing well in some cases but not others. This approach may still prove useful with some further work to constrain the solutions, but for now will be set aside.

The figure shows two separate performance curves for the BIPA estimate - this is because two alternate versions of the technique were tested. The results labelled ‘BIPA’ are obtained from the approach exactly as described in section 4.4.3. Here it was noted that the ‘zeroth’ iteration f_0 represented an initial guess at the prior in the absence of other information. For the results labelled ‘PEEA seeded BIPA’ f_0 was replaced with the PEEA estimate to investigate what effect this would have on the correction performance. We see that using the original definition of f_0 yields the best results in this case. Furthermore, we see that the standard BIPA performs *better* than the ideal case where the exact prior is used, and seems to converge to the ideal case for large \mathcal{U} . This is certainly unexpected, and the cause is not yet understood. Further work testing different datasets is needed to see if the performance ordering of the various

Chapter 4. Probabilistic noise-correction of discrete Fourier transform coefficients prior estimates persists.

On this basis of the results shown here, we conclude that the BIPA estimation approach is the best option of the three investigated. The full correction procedure can now be summarised as:

- (a) Calculate the DFT of the measured signal.
- (b) Infer the posterior for the Fourier-space standard deviation.
- (c) Estimate the distribution of the measured Fourier magnitudes (either as a sum of log-normal distributions or through other means).
- (d) Use the Bayesian iterative prior approximation to obtain an estimate of the true magnitude distribution.
- (e) Calculate the correction function $E[\tau]$ and multiply each Fourier coefficient by the corresponding correction factor.
- (f) Calculate the inverse-DFT of the spectrum to obtain the noise-corrected series.

4.7 Application to KSTAR ECEI data

Now the correction procedure has been developed and tested, it can be applied to the KSTAR electron-cyclotron emission imaging data which motivated this investigation into noise-correction. KSTAR possesses multiple ECEI systems, each having 192 individual channels. This necessitated that the correction procedure be automated, as by-hand analysis of each channel is not practical. This automation has been successfully implemented such that an arbitrary time-series can be passed to a single function which carries out each step of the process described at the end of the previous section and returns to corrected data. An example showing the correction of one of the channels is shown in figure 4.7. As we would expect, the correction has an overall smoothing effect on the time-series data.

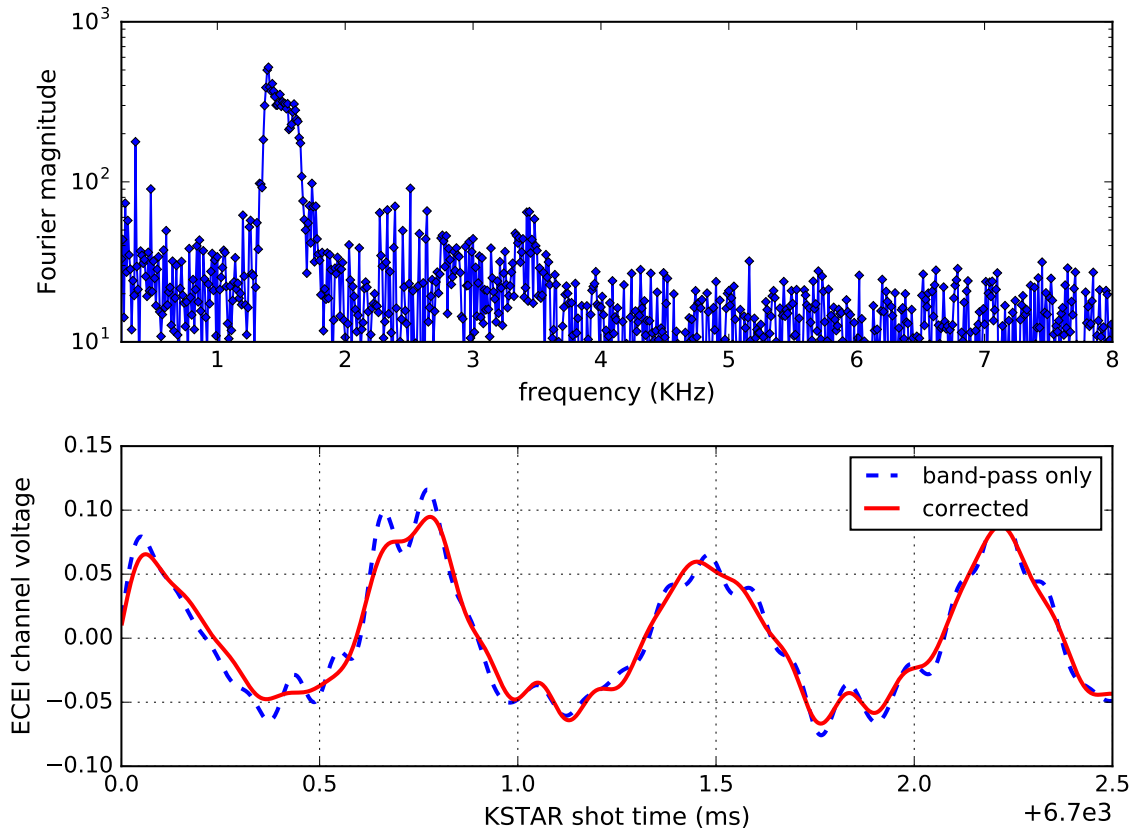


Figure 4.17: Plots of KSTAR ECEI channel #125 from shot # 6123. (top): The uncorrected Fourier magnitude spectrum of the data from 6.6 to 6.8 seconds. (bottom): Comparison between the corrected and uncorrected channel data. For both signals all frequencies below 0.25 kHz and above 8 kHz have been removed.

It is our intention that the corrected ECEI data will be used in future collaborations with NFRI and POSTECH, in particular as part of an extension to the work carried out in [17], which is attached to this thesis as an appendix. My contribution to this publication was the development of software to model the measured ECEI signals, and the design of the stochastic fitting approach used to estimate model parameters. We anticipate that a combination of the noise-corrected data and a Bayesian approach to model parameter inference will yield improved estimates of tearing mode stability parameters.

4.8 Conclusions and further work

A novel technique which corrects for the effects of random noise in an arbitrary real series G_n has been presented. The basis of the technique is to adjust the discrete Fourier

Chapter 4. Probabilistic noise-correction of discrete Fourier transform coefficients transform magnitudes of G_n such that they optimally estimate the ‘true’ magnitude which would be measured if no noise were present.

In section 4.2 it was demonstrated that for a sufficiently large series length N , after a discrete Fourier transform random noise is normally distributed in the real and imaginary parts with identical variance. A correction based on the joint-posterior for the true real and imaginary parts $P(\bar{x}, \bar{y} | x, y)$ was investigated, and shown to be dependent entirely on the prior $P(\bar{x}, \bar{y})$. It was also shown that this prior could be estimated as the solution to a 2D deconvolution problem.

To make the problem more approachable a change to polar coordinates was made, and in section 4.3 a correction to the Fourier magnitude was derived using the Rice distribution and Bayes’ theorem. The result is a correction function $E[\tau]$, which adjusts each Fourier coefficient individually based on its magnitude. By considering the distribution for the measured phase $P(\phi | \hat{\phi}, S)$ it was shown that phase-correction required the solution of a 2D inverse problem.

Section 4.4 examines the problem of estimating the prior distribution $P(S)$ starting from a known $P(R)$. Initially some basic properties of $P(S)$ were investigated using test data, and it was found that whilst $P(S)$ and $P(R)$ tend to be extremely skewed and difficult to work with, the distributions of the natural log of S and R are much better behaved and are able to be well approximated as a sum of normal distributions. It was then shown that various modifications to the inverse problem can be made which make it more tractable. Three approaches to approximating the prior were presented: the first was an iterative approach based on fundamental probability results. The second made use of the Chebyshev polynomials as an orthonormal basis to transform the modified integral inverse problem into a linear algebra inverse problem. Lastly the possibility of a trivial approximation where $P(S)$ is assumed to be numerically equivalent to $P(R)$ was discussed.

In section 4.5 the previous results were combined to demonstrate the magnitude correction technique using real data containing unknown noise. Discussions were presented

on how best to infer the value of the Fourier-domain noise standard deviation and the location of frequency based filter cut-offs.

The performance of the correction technique (and the various prior distribution estimators) were tested quantitatively in section 4.6 using simulated datasets. Gaussian noise was added to a known ‘true’ signal which was then corrected, and the resulting reduction in the noise calculated. It was found that the Bayesian iterative prior approximation yielded the best results, having very similar performance to the ‘ideal’ case obtained by using the exact prior. Meaningful reduction in the noise level was demonstrated for $\mathcal{U} \geq 0.1$, and was shown to improve consistently with increasing \mathcal{U} .

Application of the noise-correction to KSTAR ECEI data was discussed in section 4.7, along with planned future work which will make use of the corrected dataset.

4.8.1 Potential further work

An interesting possibility would be to consider whether an improved correction can be obtained by splitting the frequency space up into sections, each having its own $P(R)$ and $P(S)$. The logic for this would be that the ‘local’ version of $P(S)$ for each frequency region may better represent the contained S_k values than a ‘global’ prior. This would yield a separate correction function for each region. It could also be considered whether this probabilistic correction approach could be extended to time-frequency transforms, such as the wavelet or Gabor transforms.

Although it was demonstrated that for fixed standard deviation, the specific noise series has little effect on the correction performance (for sufficiently large N), it was not shown whether it varies significantly based on the data being corrected. The source of this variation, significant or not, must arise from differences in $P(S)$ between different sets of data. It would therefore be interesting to seek a theoretical relationship between $P(S)$ and the correction performance, in addition to simply testing other datasets to observe any variation directly. Testing additional datasets is also necessary to gain insight into why the correction using the BIPA estimate out-performed (albeit slightly) that from the exact prior.

Chapter 5

Forward-modelling of plasma parameter time-dependence effects in the DIII-D CER system

5.1 Introduction

Charge-exchange recombination (CER) is a physical process which forms the basis for several important diagnostic techniques in high-temperature plasmas physics. It is the mechanism by which a bound electron may be exchanged between two atoms during a collision. Magnetic confinement devices such as tokamaks generally have a core plasma which is fully ionised, and as such the amount of atomic line radiation produced in these regions is negligible.

However, if additional neutrals are introduced into the core plasma from an outside source, charge-exchange may take place between these neutrals and the background plasma, thereby stimulating line emission to occur where there would otherwise be none. Standard spectroscopy techniques may then be used to diagnose the line spectra, allowing us to measure important plasma parameters such as ion density, temperature and flow.

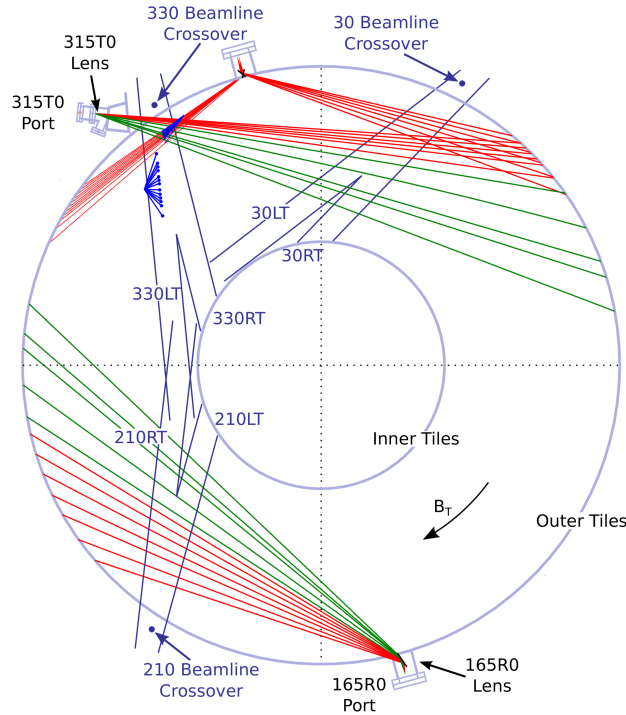


Figure 5.1: Top-down schematic view of the DIII-D torus, showing the layout of the various neutral beams and diagnostic lines-of-sight. [37]

Neutral beam injection (NBI) is typically the source by which the additional neutrals are introduced into the plasma. Often CER spectroscopy systems make use of the pre-existing neutral beams which are used to heat the plasma and inject momentum, but occasionally a separate ‘diagnostic’ neutral beam is used. By using a diagnostic line of sight which intersects a neutral beam, we are able to localise the collected line emission to a relatively small volume of plasma. Additionally we are able to make our measurements spatially resolved by collecting radiation from multiple lines-of-sight which intersect the neutral beam at different points along its length. An example of such a layout on the DIII-D tokamak is shown in figure 5.1.

The plasma flow around magnetic islands created due to neo-classical tearing modes is predicted to influence their stability and evolution. Differences in electron and ion inertia dictate that they each respond differently to the flux perturbation associated with a magnetic island as they flow around it. This leads to a ‘polarisation current’ [38, 39] which affects tearing stability. This effect is expected to play an important role in determining the threshold size and behaviour of NTMs, which is itself an area of much interest as understanding this threshold behaviour is key to preventing or stabilising NTMs in future MCF devices.

As part of an experiment on DIII-D to study NTM stability, the CER system was used to measure the ion flow in the vicinity of a magnetic island as it rotated past the diagnostic line-of-sight. The rotation frequency of the islands in question was around 1 kHz or slightly above, but the maximum available time-resolution of the CER system was $274 \mu\text{s}$. Consequently the experiment sought to push to its limit the ability of the CER system to resolve fast velocity fluctuations.

In this chapter we develop a Bayesian inference framework for the DIII-D CER system, specifically with the goal of inferring ion flow velocities and assessing the system's limit in characterising velocity fluctuations.

5.2 Constructing the CER spectrum

To infer physical quantities of interest from the observed CER spectral data, we must construct a physics model for the spectrum. Here the various mechanisms which affect the CER spectrum are discussed, with emphasis on their relevance in low-density, high-temperature tokamak plasmas.

5.2.1 Relativistic effects

For Carbon ions, thermal velocities are typically too low even at high plasma temperatures to require a proper relativistic treatment. The Lorentz factor for a carbon ion travelling at the thermal velocity in a 50 keV plasma differs negligibly from unity:

$$\gamma - 1 = \left(1 - \frac{T_i}{m_i c^2}\right)^{-\frac{1}{2}} - 1 = 2.23 \times 10^{-6} \quad (5.1)$$

On this basis effects such as relativistic beaming (where radiation is preferentially emitted toward the direction of motion such that an observer measures an increased amount of blue-shifted photons) may be ignored.

5.2.2 Doppler effects

An emitted CER photon seen by an observer is Doppler-shifted by the source ion's velocity component along the line-of-sight between the ion and observer. For positive source velocity defined to be moving away from the observer, the observed and source frequencies ν and ν_0 are related via

$$\nu = \gamma (1 - \beta) \nu_0 = \nu_0 \sqrt{\frac{1 - \beta}{1 + \beta}}. \quad (5.2)$$

Solving for β we obtain

$$\beta = \frac{\nu_0^2 - \nu^2}{\nu_0^2 + \nu^2} = \frac{\lambda^2 - \lambda_0^2}{\lambda^2 + \lambda_0^2}, \quad (5.3)$$

allowing the source velocity to be inferred from ν and ν_0 . However as previously noted, for Carbon ions in MCF-relevant temperature plasmas $\beta \ll 1$. Taylor expanding the right-hand side of (5.2) to first order about $\beta = 0$ and solving for velocity gives

$$v = c \left(1 - \frac{\nu}{\nu_0} \right) = c \left(1 - \frac{\lambda_0}{\lambda} \right). \quad (5.4)$$

Ions with some velocity distribution $P_v(v)$ emitting monochromatic photons of wavelength λ_0 will therefore give rise to the following distribution of observed wavelengths

$$P_\lambda(\lambda) d\lambda = P_v \left(c \left(1 - \frac{\lambda_0}{\lambda} \right) \right) \left(\frac{dv}{d\lambda} \right) d\lambda = \frac{c\lambda_0}{\lambda^2} P_v \left(c \left(1 - \frac{\lambda_0}{\lambda} \right) \right) d\lambda. \quad (5.5)$$

5.2.3 Natural line-width

All spectral lines have a natural width associated with the finite lifetime of excited quantum states. The uncertainty principle tells us that the spread of the state energy is roughly $\Delta E \sim \hbar/\tau$ where τ is the state lifetime. A full treatment of the problem yields the following Lorentzian line-shape

$$P(\nu|\nu_0, \tau) = \frac{2\tau}{1 + (2\pi\tau(\nu - \nu_0))^2}. \quad (5.6)$$

5.2. Constructing the CER spectrum τ can be calculated as the reciprocal of the sum of the Einstein A_{ij} coefficients for all possible transitions from the initial state plus all transitions from the final state - this accounts for the distribution of energies of both states. Typically $A_{ij} \propto \nu_{ij}^3$, resulting in short lifetimes for higher-energy transitions and a correspondingly greater natural line-width [40]. The natural broadening tends to be unimportant in hot plasmas because it is completely dominated by the thermal broadening, but for lower-temperature plasmas and transitions in the ultraviolet and above it may be relevant. As the DIII-D CER system diagnoses the C^{6+} $n = 8 \rightarrow 7$ transition at $\lambda = 529.046$ nm (around the middle of the visible light spectrum) and the plasma temperatures being observed are high, we are able to dismiss the broadening from the natural width as negligible.

5.2.4 Fine-structure splitting

Coupling between a bound electron's orbital and intrinsic angular momentum, in addition to some relativistic effects, leads to atomic 'fine structure' where quantum states of the same n but differing l, j have slightly different energies. Consequently the natural emission spectrum for the C^{6+} $n = 8 \rightarrow 7$ transition is in fact a series of closely spaced spectral lines of the form shown in (5.6) each with their own natural line-width. This effectively increases the observed natural width of the transition, but despite this it still appears to be a negligible effect.

5.2.5 Charge-exchange cross-section variation

At high neutral beam energies the sensitivity of the charge-exchange cross-section to changes in relative velocity is increased [41]. This effect, coupled with high plasma temperatures, can result in non-negligible variation of the cross-section across the distribution of relative collision velocities, leading to a non-gaussian line shape. This effect is more pronounced for light-ion targets due to their higher thermal velocities.

Experiments on JET at high ion temperatures (20 keV) demonstrated that failure to account for this effect can result in large errors in temperature estimation (as much

as 25%) when using Dueterium lines, but errors of only a few percent when using carbon lines. These experiments found no detectable differences in measured ion flow using carbon spectra as a result of taking this effect into account. Due to the use of Carbon in the DIII-D CER system, and the lower ion temperatures (relative to the aforementioned JET experiments) we may conclude that modelling the effect of cross-section variations due to the distribution of relative velocities is unnecessary for our analysis.

5.2.6 Non-thermal ion populations

Certain types of MHD instabilities or turbulent micro-instabilities may produce small populations of ions with non-thermal velocity distributions. As a result the velocity distribution of the ions at a particular point in the plasma may be slightly perturbed away from a thermal distribution. This could in principle introduce errors into measurements of the spectrum parameters, as the Gaussian line-shape assumed for thermal Doppler broadening relies on a Maxwellian ion velocity distribution.

Non-thermal ion populations appear to have little impact on the carbon CER spectroscopy measurements on DIII-D as the spectrum model derived from a Gaussian line-shape agrees with the data very well. If there were a statistically significant amount of non-thermal ions with velocities within a few standard deviations of the mean velocity we would expect to find an apparently non-random discrepancy between the model and the data, however no such discrepancy has been observed.

5.3 Bayesian inference in CER spectroscopy systems

The DIII-D CXR system records a digitised ‘counts’ value for each available pixel in the CCD. Our physics model must therefore make a prediction of this counts level in order for us to infer information about the model parameters. As a step toward this, we

5.3. Bayesian inference in CER spectroscopy systems first consider the fraction of all photons dispersed by the spectrometer which interact with a particular CCD pixel. This may be interpreted in a probabilistic sense as the average probability of a photon interacting with a pixel over all possible wavelengths.

5.3.1 Modelling photon detection probability

Let δ_n be the event that a photon interacts with pixel n . It is helpful to express δ_n and the factors on which it depends as a Bayesian network. This will allow the requisite expression for the probability of δ_n to be easily derived. Bayesian networks are often defined through directed acyclic graphs (DAGs), where variables in the system are represented as nodes, and the dependencies between those variables by directed edges (arrows). For example, for a system of two variables A and B , where A has a dependence on B , the appropriate DAG has a directed edge pointing from the B node to the A node.

To construct a Bayesian network in this fashion, we begin by creating a node for δ_n , add nodes for the variables on which it depends, and connect them with the appropriate edges. This process is repeated for each new node added until there are no further dependencies to include, and the network is complete.

Clearly, the position x at which a photon meets the CCD will influence whether that photon is detected in any given pixel. Additionally, the quantum efficiency of the CCD will depend on the wavelength λ of the photon. δ_n is therefore determined by both x and λ .

Next we must consider the dependencies of x and λ . As the spectrometer disperses the photons based on their wavelength, x depends on λ . A model for the dispersion is required to describe precisely the relationship between λ and x . At this point we need not specify anything about such a model other than that it is defined by some parameter vector $\underline{\alpha}$. x is therefore determined by both λ and $\underline{\alpha}$.

The probability a given photon has wavelength λ depends on the spectrum of light which leaves the spectrometer. The dependencies of λ are therefore the parameters of

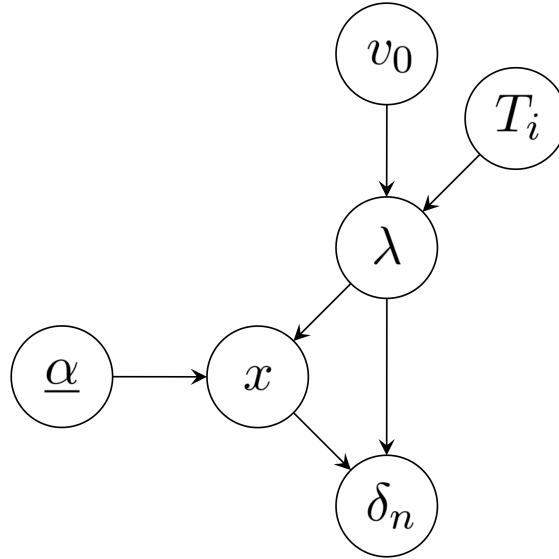


Figure 5.2: A directed acyclic graph of the Bayesian network for the photon detection probability δ_n . Such networks provide a convenient way to map out the dependencies of variables in a system.

our model for this spectrum. Any such model will include the mean flow velocity v_0 and impurity ion temperature T_i which determine the charge-exchange spectrum. v_0 and T_i have no dependencies, so there are no further nodes to be added to the network. The completed network is illustrated as a DAG in figure 5.2.

The network allows us to easily derive the joint probability distribution $P(\delta_n, x, \lambda | v_0, T_i, \underline{\alpha})$ as the product of the individual distributions for δ_n, x, λ , which may be determined from the graph in 5.2. We may therefore write

$$P(\delta_n, x, \lambda | v_0, T_i, \underline{\alpha}) = P(\delta_n | x, \lambda) P(x | \lambda, \underline{\alpha}) P(\lambda | v_0, T_i). \quad (5.7)$$

We want the probability a photon is detected irrespective of its wavelength or position. This may be obtained by integrating (5.7) over all λ, x yielding:

$$P(\delta_n | v_0, T_i, \underline{\alpha}) = \int_0^\infty \int_0^\infty P(\delta_n | x, \lambda) P(x | \lambda, \underline{\alpha}) P(\lambda | v_0, T_i) d\lambda dx. \quad (5.8)$$

At this point it is useful to provide some context by discussing the physical meaningfulness of the three distributions on the right-hand side of (5.8). $P(\lambda | v_0, T_i)$ can be straightforwardly interpreted as describing the wavelength spectrum of incoming CER photons. $P(x | \lambda, \underline{\alpha})$ is the distribution of possible locations a photon of given

5.3. Bayesian inference in CER spectroscopy systems
wavelength may land on the CCD, which is typically referred to as the ‘instrument function’ of the spectrometer-CCD system. $P(\delta_n|x, \lambda)$ is the probability that a photon with a particular wavelength and position interacts with pixel n , and as such may be interpreted as the ‘pixel sensitivity’.

5.3.2 Distribution of wavelengths for incident photons: $P(\lambda|v_0, T_i)$

Our starting point is to assume a thermal velocity distribution with a mean flow

$$P(v|v_0, T_i) = \frac{1}{v_{th}\sqrt{\pi}} \exp\left[-\frac{(v - v_0)^2}{v_{th}^2}\right], \quad v_{th} = \sqrt{\frac{2T_i}{m_i}}, \quad (5.9)$$

where v_0 is the line-of-sight flow velocity, and T_i, m_i are the ion temperature and mass respectively. As discussed in section 5.2.1, even at very high plasma temperatures the thermal velocities of carbon ions are not sufficient to require relativistic treatment. As such, we take the non-relativistic limit of the Doppler effect, where

$$v = c \left(\frac{\lambda_0}{\lambda} - 1 \right). \quad (5.10)$$

λ_0 is the initial wavelength and λ is wavelength as seen by a lab-frame observer. To obtain the distribution for the wavelength, we make the following substitution:

$$\int_{\lambda_1}^{\lambda_2} P(\lambda|v_0, T_i) d\lambda = \int_{v(\lambda_2)}^{v(\lambda_1)} P(v|v_0, T_i) \left(-\frac{dv}{d\lambda} \right) d\lambda, \quad (5.11)$$

such that we may write

$$P(\lambda|v_0, T_i) d\lambda = P(v|v_0, T_i) \left(-\frac{dv}{d\lambda} \right) d\lambda = P(v|v_0, T_i) \left(\frac{c\lambda_0}{\lambda^2} \right) d\lambda. \quad (5.12)$$

$P(\lambda|v_0, T_i)$ is the probability that an incident photon has wavelength λ for a given v_0, T_i , and may now be expressed as

$$P(\lambda|v_0, T_i) = \frac{c\lambda_0}{v_{th}\lambda^2\sqrt{\pi}} \exp\left[-\frac{c^2}{v_{th}^2\lambda^2} \left(\lambda_0 - \lambda \left(1 + \frac{v_0}{c} \right) \right)^2\right]. \quad (5.13)$$

This is sufficient to model the charge exchange emission at a single point in time and space, but in reality the detected emission originates from some volume of space V_i over an integration time t_i . Accounting for the time-dependence of model parameters is addressed later in section 5.3.5. Spatial variation of the temperature and flow over the integration volume will not be modelled explicitly. It is instead assumed that local gradients in v_0 and T_i are sufficiently small that the spatial variation may be ignored.

5.3.3 Model for the instrument function: $P(x|\lambda, \underline{\alpha})$

The point-spread function (PSF) for the CER system is parametrised about zero as a sum of Gaussian functions:

$$\text{PSF} = \sum_k \frac{A_k}{S_k \sqrt{2\pi}} \exp \left[-\frac{1}{2} \left(\frac{x - L_k}{S_k} \right)^2 \right], \quad (5.14)$$

which is appropriately normalised provided that

$$\sum_k A_k = 1. \quad (5.15)$$

The A_k , L_k , and S_k are experimentally-determined constants. The PSF does not depend on λ , so to obtain $P(x|\lambda, \underline{\alpha})$ we must include a model for the dispersion. The dispersion is a function which relates λ to the point x_0 on the CCD where a photon of that wavelength would land in the absence of any point-spread effect. This is often determined through experimental calibration, and parametrised as a polynomial with coefficients \underline{d} . In this case, the dispersion is taken to be linear:

$$x_0 = d_1 \lambda + d_0. \quad (5.16)$$

We will see later in section 5.4.1 that a linear dispersion relation is an important feature of the experimental design from an analysis perspective, as it allows the instrument function convolution to be dealt with analytically. This represents a huge simplification and computational cost saving, and is not possible if non-linear terms are needed to adequately describe the dispersion. We require that the PSF is centred about x_0 rather

5.3. Bayesian inference in CER spectroscopy systems than zero, which can be achieved by replacing x with $x - x_0$ in (5.14). Doing so allows us to define

$$P(x|\lambda, \underline{\alpha}) = \sum_k \frac{A_k}{S_k \sqrt{2\pi}} \exp \left[-\frac{1}{2} \left(\frac{x - L_k - d_1 \lambda - d_0}{S_k} \right)^2 \right]. \quad (5.17)$$

As we defined $\underline{\alpha}$ to be the vector of all parameters needed to specify $P(x|\lambda, \underline{\alpha})$, it necessarily contains \underline{d} , \underline{A} , \underline{L} , and \underline{S} .

5.3.4 Model for pixel sensitivity: $P(\delta_n|x, \lambda)$

If we assume that the quantum efficiency Q of the CCD varies negligibly over the range of x, λ in the experiment so that we may treat it as constant, then the simplest model we can write for $P(\delta_n|x, \lambda)$ is:

$$P(\delta_n|x, \lambda) = \begin{cases} Q & \text{if } |x - x_n| < \frac{1}{2}w \\ 0 & \text{otherwise} \end{cases}, \quad (5.18)$$

where x_n is the centre location of pixel n and w is the width of a pixel. This model also assumes that the angle of incidence ϕ is zero for all x , but is good approximation provided ϕ remains small. The potential for charges to leak between adjacent pixels has been purposefully ignored here, as this effect should be captured by the experimentally-determined instrument function profiles in $P(x|\lambda, \underline{\alpha})$.

5.3.5 Expected counts & time-dependence of the CER spectrum

If the model in (5.18) is used, (5.8) becomes

$$P(\delta_n|v_0, T_i) = Q \int_{x_n - \frac{1}{2}w}^{x_n + \frac{1}{2}w} \int_0^\infty P(x|\lambda, \underline{\alpha}) P(\lambda|v_0, T_i) d\lambda dx. \quad (5.19)$$

Let R_γ be the rate at which charge-exchange photons leave the spectrometer. The number of photons detected in pixel n is then

$$C_n(\underline{\theta}) = Q \int_{t_0 - \frac{1}{2}t_i}^{t_0 + \frac{1}{2}t_i} R_\gamma \int_{x_n - \frac{1}{2}w}^{x_n + \frac{1}{2}w} \int_0^\infty P(x|\lambda, \underline{\alpha})P(\lambda|v_0, T_i) d\lambda dx dt, \quad (5.20)$$

where t_i is the integration time of the measurement, t_0 is the time at the centre of the integration window and $\underline{\theta}$ is a vector containing all model parameters.

Generally, when physical quantities are inferred based on diagnostic data collected over an integration time, it is assumed that these quantities do not vary significantly over the time window such that they can be assumed to have zero time-dependence.

However if meaningful variation in the model parameters does occur on time-scales comparable to t_i , this assumption is no longer satisfactory. To address this, the time dependences of v_0, T_i, R_γ are modelled as Taylor expansions about the centre of the integration window:

$$v_0(t) \approx \sum_{n=0}^N \frac{(t - t_0)^n}{n!} v_0^{(n)}, \quad (5.21)$$

$$T_i(t) \approx \sum_{n=0}^N \frac{(t - t_0)^n}{n!} T_i^{(n)}, \quad (5.22)$$

$$R_\gamma(t) \approx \sum_{n=0}^N \frac{(t - t_0)^n}{n!} R_\gamma^{(n)}. \quad (5.23)$$

This approach is convenient because the model parameters which determine these quantities (the $v_0^{(n)}, T_i^{(n)}$ and $R_\gamma^{(n)}$) are now by definition their time-derivatives evaluated at t_0 . Consequently, we may now infer probability distributions for these time-derivatives as an alternative (or in addition) to those for the values of the quantities at t_0 .

It should not be necessary to expand v_0, T_i and R_γ past second-order. If the time-behaviour of these quantities during the integration time cannot be adequately approximated by a quadratic, then t_i is likely too large to properly capture their dynamics. Expanding to higher orders also greatly increases the number of model parameters, thereby significantly increasing computational costs.

We must also consider the effect of background emission (any radiation reaching the CCD not arising from the charge exchange process) on the number of detected photons. To account for this we include a background model $\beta_n(\underline{u})$ which at this point can remain unspecified other than that is defined by some set of parameters \underline{u} . After inclusion of this model $C_n(\underline{\theta})$ becomes

$$C_n(\underline{\theta}) = Q \int_{t_0 - \frac{1}{2}t_i}^{t_0 + \frac{1}{2}t_i} R_\gamma \int_{x_n - \frac{1}{2}w}^{x_n + \frac{1}{2}w} \int_0^\infty P(x|\lambda, \underline{\alpha}) P(\lambda|v_0, T_i) d\lambda dx dt + \beta_n(\underline{u}). \quad (5.24)$$

5.3.6 Inference of model parameter distributions

To infer the probability of the model parameters $\underline{\theta}$, we first require a statistical model for the uncertainty in the observed data, given our model for the expected counts. Let the predicted total amount of detected photons across all pixels be m ;

$$m = \sum_n C_n. \quad (5.25)$$

We can think of $C_n(\underline{\theta})/m$ as an updated photon detection probability which now includes our model for background light sources. In this sense we can model the probability of observing a number of photons y_n in pixel n through the following binomial distribution:

$$P(y_n|\underline{\theta}) = \frac{m!}{y_n!(m - y_n)!} \left(\frac{C_n}{m}\right)^{y_n} \left(1 - \frac{C_n}{m}\right)^{m - y_n}. \quad (5.26)$$

Note here that as y_n is a number of observed photons, this is not necessarily equal to the ‘counts’ value reported by the CCD - typically multiple photons must interact with a given pixel in order to accumulate enough charge to register a CCD count. Consequently, a calibration for the average photons per count is needed to obtain the y_n . Often counting uncertainties are taken to be Poisson-distributed. Figure 5.3 illustrates that the Poisson distribution is in fact a limiting case of the above binomial distribution when $c_n \ll m$;

$$\lim_{m/c_n \rightarrow \infty} P(y_n|\underline{\theta}) = \frac{C_n^{y_n}}{y_n!} \exp(-C_n). \quad (5.27)$$

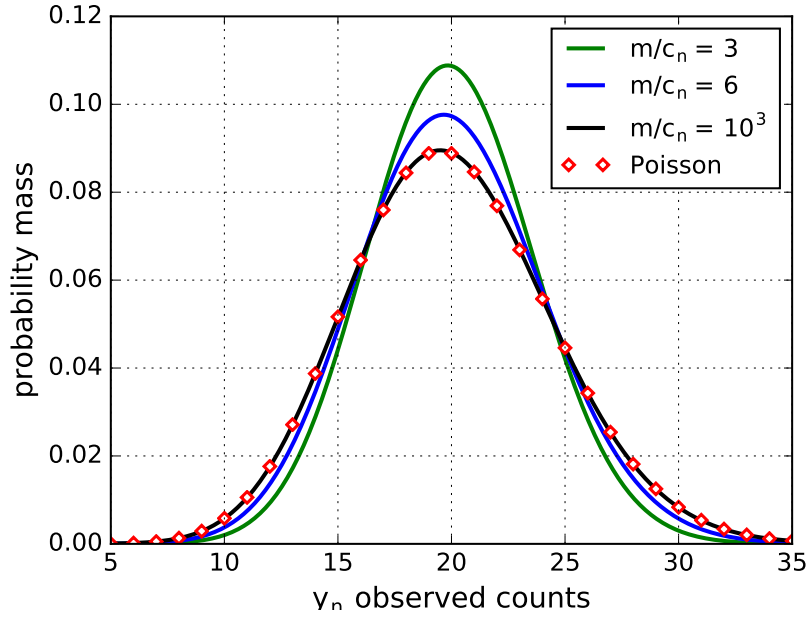


Figure 5.3: Plots of the binomial distribution in (5.26) for various values of m (lines), and the limiting Poisson distribution in (5.27) (points) with $C_n = 20$. It can be seen that in the limit where $m/C_n \gg 1$ the uncertainty becomes Poisson distributed.

For most pixels in DIII-D CER measurements the m/C_n values are very large and the binomial distribution is indistinguishable from the Poisson distribution. Pixels around the peak of the CER spectrum could have a m/C_n as low as 30, but even in this case the two distributions differ by only a few percent at their peak. Accordingly we will assume that the y_n are Poisson distributed and mutually statistically independent, such that the joint probability of all y_n can be written as the product of their individual likelihoods. Let $\mathcal{D} = \{y_n\}$, then:

$$P(\mathcal{D}|\underline{\theta}) = \prod_n P(y_n|\underline{\theta}) = \exp \left[\sum_n y_n \ln (C_n(\underline{\theta})) - C_n(\underline{\theta}) - \ln (\Gamma(y_n + 1)) \right]. \quad (5.28)$$

We may now use Bayes' theorem to obtain the probability of the model parameters $\underline{\theta}$:

$$P(\underline{\theta}|\mathcal{D}) = \frac{P(\mathcal{D}|\underline{\theta})P(\underline{\theta})}{P(\mathcal{D})} \quad (5.29)$$

The prior distribution $P(\underline{\theta})$ represents any information on the model parameters which is already known, for example knowledge obtained from a Bayesian treatment of another diagnostic system. The distribution $P(\mathcal{D})$ may be determined through normalisation of $P(\mathcal{D}|\underline{\theta})P(\underline{\theta})$.

We may now infer the probability distribution of a sub-set of desired model parameters.

5.4. Numerical optimisation of the model

Let \underline{z} the set parameters which we wish to infer, and $\underline{\epsilon}$ be the complement of \underline{z} with respect to $\underline{\theta}$ such that $\underline{\theta} = [\underline{z}, \underline{\epsilon}]$. The $\underline{\epsilon}$ are often referred to as ‘nuisance parameters’ and are removed from the joint probability distribution by integrating over each variable - this process is known as marginalisation. Accordingly we may express $P(\underline{z}|\mathcal{D})$ as

$$P(\underline{z}|\mathcal{D}) = \int_{-\infty}^{\infty} \cdots \int_{-\infty}^{\infty} P(\underline{z}, \underline{\epsilon}|\mathcal{D}) d\underline{\epsilon}. \quad (5.30)$$

The full calculation of $P(\underline{z})$ may now be summarised as:

$$P(\underline{z}|\mathcal{D}) = \int_{-\infty}^{\infty} \cdots \int_{-\infty}^{\infty} \exp \left[\sum_n y_n \ln (C_n(\underline{\theta})) - C_n(\underline{\theta}) - \ln (\Gamma(y_n + 1)) \right] \frac{P(\underline{\theta})}{P(\mathcal{D})} d\underline{\epsilon} \quad (5.31)$$

$$C_n(\underline{\theta}) = Q \int_{t_0 - \frac{1}{2}t_i}^{t_0 + \frac{1}{2}t_i} R_\gamma \int_{x_n - \frac{1}{2}w}^{x_n + \frac{1}{2}w} \int_0^\infty P(x|\lambda, \underline{\alpha}) P(\lambda|v_0, T_i) d\lambda dx dt + \beta_n(\underline{u}). \quad (5.32)$$

5.4 Numerical optimisation of the model

Computational cost is a concern for the numerical implementation of Bayesian inference systems, usually due to the presence of a high-dimensionality integral such as that in (5.31). It is therefore important to consider whether the calculation of the physics model (in this case $C_n(\underline{\theta})$) may be simplified without sacrificing significant accuracy. The obvious target for our efforts in this regard are the three integrals in (5.32).

5.4.1 Wavelength integration

If the range of λ over which the spectrum is observed is small in comparison to λ_0 , then

$$\left(1 - \frac{\lambda}{\lambda_0}\right) \approx -\left(1 - \frac{\lambda_0}{\lambda}\right). \quad (5.33)$$

The above may be used with (5.13) to yield a Gaussian approximation of $P(\lambda|v_0, T_i)$, which we will call $f(\lambda)$:

$$P(\lambda|v_0, T_i) \approx f(\lambda) = \frac{c}{v_{th}\lambda_0\sqrt{\pi}} \exp \left[-\frac{c^2}{v_{th}^2\lambda_0^2} \left(\lambda - \lambda_0 \left(1 - \frac{v_0}{c} \right) \right)^2 \right]. \quad (5.34)$$

$f(\lambda)$ has mean and variance

$$\mu_f = \lambda_0 \left(1 - \frac{v_0}{c} \right), \quad \sigma_f^2 = \frac{1}{2} \left(\frac{v_{th}\lambda_0}{c} \right)^2. \quad (5.35)$$

For DIII-D relevant spectrum parameters the fractional error in this approximation is less than 1% within $\mu_f \pm 3\sigma_f$, as illustrated in figure 5.4. Now temporarily re-arrange

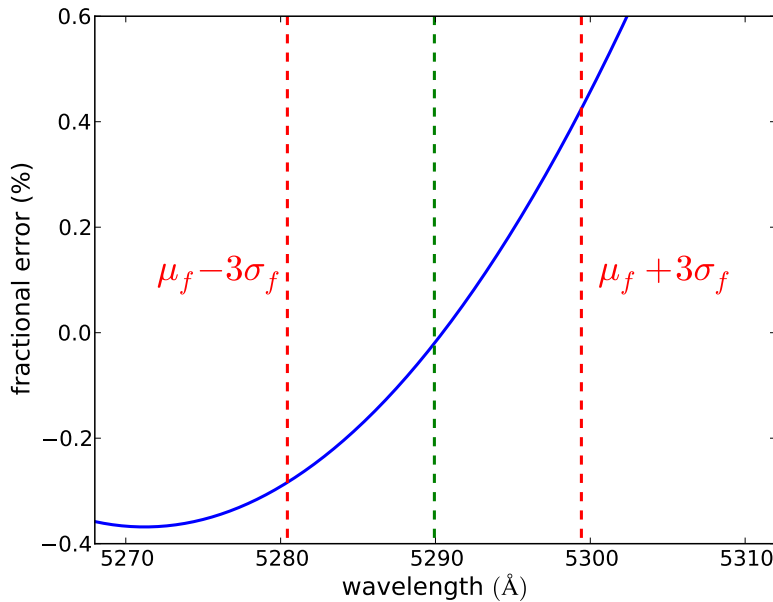


Figure 5.4: Plot of the fractional error in $f(\lambda)$ for $T_i = 4$ keV, $v_0 = 30$ km/s and $\lambda_0 = 5920.46$ Å. The green dashed line marks the location of μ_f and the red dashed lines mark $\mu_f \pm 3\sigma_f$.

(5.17) as a Gaussian in λ :

$$P(x|\lambda, \underline{\alpha}) = \sum_k \frac{A_k}{S_k\sqrt{2\pi}} \exp \left[-\frac{1}{2} \frac{d_1^2}{S_k^2} \left(\lambda - \frac{x - L_k - d_0}{d_1} \right)^2 \right], \quad (5.36)$$

which has mean and variance

$$\mu_k = \frac{x - L_k - d_0}{d_1}, \quad \sigma_k^2 = \frac{S_k^2}{d_1^2}. \quad (5.37)$$

Replacing $P(\lambda|v_0, T_i)$ with $f(\lambda)$ in (5.19) allows us to evaluate the integral over λ analytically:

$$\begin{aligned} & \sum_k \frac{A_k}{2\pi\sigma_f\sigma_k d_1} \int_0^\infty \exp \left[-\frac{1}{2} \left(\frac{\lambda - \mu_f}{\sigma_f} \right)^2 - \frac{1}{2} \left(\frac{\lambda - \mu_k}{\sigma_k} \right)^2 \right] d\lambda \\ &= \sum_k \frac{A_k}{d_1 \sqrt{2\pi} (\sigma_f^2 + \sigma_k^2)} \exp \left[-\frac{1}{2} \frac{(\mu_f - \mu_k)^2}{\sigma_f^2 + \sigma_k^2} \right] \end{aligned} \quad (5.38)$$

The exponential in $P(\delta_n|v_0, T_i)$ may now be expressed as a Gaussian in x :

$$P(\delta_n|v_0, T_i) = Q \sum_k \int_{x_n - \frac{1}{2}w}^{x_n + \frac{1}{2}w} \frac{A_k}{\sigma_x \sqrt{2\pi}} \exp \left[-\frac{1}{2} \left(\frac{x - \mu_x}{\sigma_x} \right)^2 \right] dx, \quad (5.39)$$

with mean and variance

$$\mu_x = L_k + d_0 + d_1 \lambda_0 \left(1 - \frac{v_0}{c} \right), \quad \sigma_x^2 = \left(\frac{T_i}{m_i c^2} \right) \lambda_0^2 d_1^2 + S_k^2. \quad (5.40)$$

5.4.2 Pixel-width integration

Now the integrand in $P(\delta_n|v_0, T_i)$ has been reduced to a Gaussian, the x integral can be easily calculated as

$$\begin{aligned} & \int_{x_n - \frac{1}{2}w}^{x_n + \frac{1}{2}w} \frac{1}{\sigma_x \sqrt{2\pi}} \exp \left[-\frac{1}{2} \left(\frac{x - \mu_x}{\sigma_x} \right)^2 \right] dx = \\ & \frac{1}{2} \left[\operatorname{erf} \left(\frac{x_n - \mu_x + \frac{1}{2}w}{\sigma_x \sqrt{2}} \right) - \operatorname{erf} \left(\frac{x_n - \mu_x - \frac{1}{2}w}{\sigma_x \sqrt{2}} \right) \right], \end{aligned} \quad (5.41)$$

such that the detection probability is now

$$P(\delta_n|v_0, T_i) = Q \sum_k A_k \left[\frac{1}{2} \operatorname{erf} \left(\frac{x_n - \mu_x + \frac{1}{2}w}{\sigma_x \sqrt{2}} \right) - \frac{1}{2} \operatorname{erf} \left(\frac{x_n - \mu_x - \frac{1}{2}w}{\sigma_x \sqrt{2}} \right) \right]. \quad (5.42)$$

5.4.3 Time integration

The model for the expected counts has now been simplified to

$$C_n(\underline{\theta}) = Q \left(\sum_k A_k \int_{t_0 - \frac{1}{2}t_i}^{t_0 + \frac{1}{2}t_i} R_\gamma \left[\frac{1}{2} \operatorname{erf} \left(\frac{\psi + \eta}{\sqrt{2}} \right) - \frac{1}{2} \operatorname{erf} \left(\frac{\psi - \eta}{\sqrt{2}} \right) \right] dt \right) + \beta_n(\underline{u}), \quad (5.43)$$

where

$$\psi = \frac{x_n - \mu_x}{\sigma_x}, \quad \eta = \frac{w}{2\sigma_x}. \quad (5.44)$$

The remaining integral over time has no analytical solutions for even simple models of time-dependence (for example if v_0, T_i, R_γ are assumed to vary linearly with time). We must therefore either evaluate the integral numerically or find a suitable analytical approximation. An infinite-series solution to the integral can be constructed by considering the Taylor expansion of the integrand $y(t)$ about t_0 ;

$$y(t) = R_\gamma \left[\frac{1}{2} \operatorname{erf} \left(\frac{\psi + \eta}{\sqrt{2}} \right) - \frac{1}{2} \operatorname{erf} \left(\frac{\psi - \eta}{\sqrt{2}} \right) \right] = \sum_{k=0}^{\infty} \frac{(t - t_0)^k}{k!} y^{(k)}(t_0). \quad (5.45)$$

The integral may now be represented exactly as

$$\begin{aligned} \int_{t_0 - \frac{1}{2}t_i}^{t_0 + \frac{1}{2}t_i} y(t) dt &= \sum_{k=0}^{\infty} \frac{y^{(k)}(t_0)}{k!} \int_{t_0 - \frac{1}{2}t_i}^{t_0 + \frac{1}{2}t_i} (t - t_0)^k dt = \sum_{k=0}^{\infty} \frac{2^{-2k} (t_i^{2k+1})}{(2k+1)(2k)!} y^{(2k)}(t_0) \\ &= y(t_0)t_i + y^{(2)}(t_0) \frac{t_i^3}{24} + y^{(4)}(t_0) \frac{t_i^5}{1920} + \dots \end{aligned} \quad (5.46)$$

Truncating this series at the second order term yields an excellent approximation of the integral for physically sensible time-variation. To compute the second-order term we require the second-derivative of y from (5.45) with respect to time. To simplify this process let

$$\frac{\partial}{\partial t} \frac{1}{2} \operatorname{erf} \left(\frac{z}{\sqrt{2}} \right) = \frac{\partial z}{\partial t} G(z), \quad G(z) = \frac{1}{\sqrt{2\pi}} \exp \left[-\frac{z^2}{2} \right]. \quad (5.47)$$

Differentiating y twice gives

$$\begin{aligned} \frac{\partial^2 y}{\partial t^2} &= \frac{\partial^2 R_\gamma}{\partial t^2} \left[\frac{1}{2} \operatorname{erf} \left(\frac{\psi + \eta}{\sqrt{2}} \right) - \frac{1}{2} \operatorname{erf} \left(\frac{\psi - \eta}{\sqrt{2}} \right) \right] + \\ &2 \frac{\partial R_\gamma}{\partial t} \left[\left(\frac{\partial \psi}{\partial t} + \frac{\partial \eta}{\partial t} \right) G(\psi + \eta) - \left(\frac{\partial \psi}{\partial t} - \frac{\partial \eta}{\partial t} \right) G(\psi - \eta) \right] + \\ &R_\gamma \left[\left(\frac{\partial^2 \psi}{\partial t^2} + \frac{\partial^2 \eta}{\partial t^2} - (\psi + \eta) \left(\frac{\partial \psi}{\partial t} + \frac{\partial \eta}{\partial t} \right)^2 \right) G(\psi + \eta) - \right. \\ &\left. \left(\frac{\partial^2 \psi}{\partial t^2} - \frac{\partial^2 \eta}{\partial t^2} - (\psi - \eta) \left(\frac{\partial \psi}{\partial t} - \frac{\partial \eta}{\partial t} \right)^2 \right) G(\psi - \eta) \right]. \end{aligned} \quad (5.48)$$

This in turn requires the first and second derivatives of ψ and η , which are:

$$\frac{\partial \eta}{\partial t} = \frac{\partial}{\partial t} \left(\frac{w}{2\sigma_x} \right) = -\frac{w}{2\sigma_x^2} \frac{\partial \sigma_x}{\partial t}, \quad (5.49)$$

$$\frac{\partial^2 \eta}{\partial t^2} = \frac{w}{\sigma_x^3} \left(\frac{\partial \sigma_x}{\partial t} \right)^2 - \frac{w}{2\sigma_x^2} \frac{\partial^2 \sigma_x}{\partial t^2}, \quad (5.50)$$

$$\frac{\partial \psi}{\partial t} = \frac{\partial}{\partial t} \left(\frac{x_n - \mu_x}{\sigma_x} \right) = -\frac{x_n - \mu_x}{\sigma_x^2} \frac{\partial \sigma_x}{\partial t} - \frac{1}{\sigma_x} \frac{\partial \mu_x}{\partial t}, \quad (5.51)$$

$$\begin{aligned} \frac{\partial^2 \psi}{\partial t^2} &= \frac{2}{\sigma_x^2} \frac{\partial \mu_x}{\partial t} \frac{\partial \sigma_x}{\partial t} - \frac{x_n - \mu_x}{\sigma_x^2} \frac{\partial^2 \sigma_x}{\partial t^2} + 2 \frac{x_n - \mu_x}{\sigma_x^3} \left(\frac{\partial \sigma_x}{\partial t} \right)^2 - \frac{1}{\sigma_x} \frac{\partial^2 \mu_x}{\partial t^2} \\ &= \frac{2}{\sigma_x^2} \frac{\partial \mu_x}{\partial t} \frac{\partial \sigma_x}{\partial t} - \frac{\psi}{\sigma_x} \frac{\partial^2 \sigma_x}{\partial t^2} + \frac{2\psi}{\sigma_x^2} \left(\frac{\partial \sigma_x}{\partial t} \right)^2 - \frac{1}{\sigma_x} \frac{\partial^2 \mu_x}{\partial t^2}. \end{aligned} \quad (5.52)$$

Finally we need the derivatives of μ_x and σ_x in terms of T_i and v_0 :

$$\frac{\partial \mu_x}{\partial t} = \frac{\partial}{\partial t} \left(L_k + d_0 + d_1 \lambda_0 \left(1 - \frac{v_0}{c} \right) \right) = -\frac{d_1 \lambda_0}{c} \frac{\partial v_0}{\partial t}, \quad (5.53)$$

$$\frac{\partial^2 \mu_x}{\partial t^2} = -\frac{d_1 \lambda_0}{c} \frac{\partial^2 v_0}{\partial t^2}, \quad (5.54)$$

$$\frac{\partial \sigma_x}{\partial t} = \frac{1}{2\sigma_x} \frac{\partial \sigma_x^2}{\partial t} = \frac{1}{2\sigma_x} \frac{\partial}{\partial t} \left(\left(\frac{\lambda_0 d_1}{c} \right)^2 \frac{T_i}{m_i} + S_k^2 \right) = \frac{1}{2\sigma_x} \frac{1}{m_i} \left(\frac{\lambda_0 d_1}{c} \right)^2 \frac{\partial T_i}{\partial t}, \quad (5.55)$$

$$\begin{aligned} \frac{\partial^2 \sigma_x}{\partial t^2} &= \frac{1}{2\sigma_x} \frac{1}{m_i} \left(\frac{\lambda_0 d_1}{c} \right)^2 \frac{\partial^2 T_i}{\partial t^2} - \frac{1}{2\sigma_x^2} \frac{1}{m_i} \left(\frac{\lambda_0 d_1}{c} \right)^2 \frac{\partial T_i}{\partial t} \frac{\partial \sigma_x}{\partial t} \\ &= \frac{\partial \sigma_x}{\partial t} \left(\frac{\partial^2 T_i}{\partial t^2} / \frac{\partial T_i}{\partial t} \right) - \frac{1}{\sigma_x} \left(\frac{\partial \sigma_x}{\partial t} \right)^2. \end{aligned} \quad (5.56)$$

Referring back to the definitions of $v_0(t)$, $T_i(t)$ and $R_\gamma(t)$ in (5.21), (5.22) and (5.23) we see that their derivatives at $t = t_0$ are the corresponding model parameters which define the Taylor expansions:

$$\left[\left(\frac{\partial}{\partial t} \right)^n v_0(t) \right]_{t=t_0} = v_0^{(n)}, \quad \left[\left(\frac{\partial}{\partial t} \right)^n T_i(t) \right]_{t=t_0} = T_i^{(n)}, \quad \left[\left(\frac{\partial}{\partial t} \right)^n R_\gamma(t) \right]_{t=t_0} = R_\gamma^{(n)}. \quad (5.57)$$

For the general case these expressions are large, so much so that in practice numerical integration techniques such as quadrature or the Newton-Coates formulae yield comparable approximations at less computational expense. The current implementation evaluates the integral using a 9-point composite Boole's rule - numerical testing has shown this to be extremely accurate for physically sensible model parameters.

These expressions can be simplified significantly in special cases however - for example under the assumption that there is no variation in temperature and linear changes in velocity and photon rate we obtain

$$\begin{aligned} \frac{\partial^2 y}{\partial t^2} &= \left(\frac{d_1 \lambda_0}{\sigma_x c} \right) \left(\frac{\partial v_0}{\partial t} \right) \left(2 \left(\frac{\partial R_\gamma}{\partial t} \right) [G(\psi + \eta) - G(\psi - \eta)] - \right. \\ &\quad \left. R_\gamma \left(\frac{d_1 \lambda_0}{\sigma_x c} \right) \left(\frac{\partial v_0}{\partial t} \right) [(\psi + \eta)G(\psi + \eta) - (\psi - \eta)G(\psi - \eta)] \right). \end{aligned} \quad (5.58)$$

For the case where only the velocity is allowed to vary (and does so linearly) the expression becomes very simple:

$$\frac{\partial^2 y}{\partial t^2} = R_\gamma \left(\frac{d_1 \lambda_0}{\sigma_x c} \right)^2 \left(\frac{\partial v_0}{\partial t} \right)^2 [(\psi - \eta)G(\psi - \eta) - (\psi + \eta)G(\psi + \eta)] \quad (5.59)$$

These cases are simplified enough that the series solution is a reasonable alternative to numerical integration.

5.5 Effects of time-dependence on predicted spectra

tra

As changes in the ion temperature, flow or density during the course of the diagnostic integration time distort the observed spectrum, we could in principle retrieve information about this time evolution from the experimental data. In effect, this would push the time-resolution of the instrument below the integration time.

This would require both that we have model which can describe the time-evolution of the parameters during the integration time, and that any such evolution has a non-negligible impact on the experimental data. Because of the forward-modelling approach used to derive our model for the observed counts, an integral over the integration time arises naturally, and the time-dependence of the plasma parameters can be conveniently modelled through Taylor expansions as described in section 5.3.5, so the first requirement is already met.

In this section we investigate the second requirement: does the time-evolution of the temperature, density and flow during the integration time result in measurable differences to the observed spectra?

5.5.1 Analytical results for linear velocity changes

For the general case, the time-integration in the time-dependent model must be evaluated numerically - however in the case of linear velocity changes only progress can be made analytically. Using the series in (5.46) truncated to second-order, the fractional change arising from the inclusion of time-dependence is

$$\frac{y(t_0)t_i + y^{(2)}(t_0)\frac{t_i^3}{24}}{y(t_0)t_i} - 1 = \frac{t_i^2}{24} \frac{y^{(2)}(t_0)}{y(t_0)}. \quad (5.60)$$

Referring to (5.59) for the linear velocity case, we see that the maximum absolute change occurs at $\psi = 0$. Evaluating the fractional change with $\psi = 0$ gives

$$\begin{aligned} \left[\frac{t_i^2 y^{(2)}(t_0)}{24 y(t_0)} \right]_{\psi=0} &= -2 \frac{t_i^2}{24} \left(\frac{d_1 \lambda_0}{\sigma_x c} \right)^2 \left(\frac{\partial v_0}{\partial t} \right)^2 \eta \frac{G(\eta) + G(-\eta)}{\operatorname{erf}\left(\frac{\eta}{\sqrt{2}}\right) - \operatorname{erf}\left(-\frac{\eta}{\sqrt{2}}\right)} \\ &= -\frac{t_i^2}{12} \left(\frac{d_1 \lambda_0}{\sigma_x c} \right)^2 \left(\frac{\partial v_0}{\partial t} \right)^2 \frac{\eta G(\eta)}{\operatorname{erf}\left(\frac{\eta}{\sqrt{2}}\right)}. \end{aligned} \quad (5.61)$$

η arises from pixel-width effects and is small. In the limit that $\eta \rightarrow 0$ the terms containing η become

$$\lim_{\eta \rightarrow 0} \left[\frac{\eta G(\eta)}{\operatorname{erf}\left(\frac{\eta}{\sqrt{2}}\right)} \right] = \frac{1}{2\sqrt{2\pi}}. \quad (5.62)$$

Using this limit to remove the η dependence from (5.61) we obtain

$$\left[\frac{t_i^2 y^{(2)}(t_0)}{24 y(t_0)} \right]_{\psi=0} = -\frac{t_i^2}{24\sqrt{2\pi}} \left(\frac{d_1 \lambda_0}{\sigma_x c} \right)^2 \left(\frac{\partial v_0}{\partial t} \right)^2. \quad (5.63)$$

As we have specified that the velocity changes are linear, the time-derivative of v_0 may be replaced with a total velocity change Δv_0 over the integration time. We may also expand σ_x at this stage. This yields the final expression

$$\left[\frac{t_i^2 y^{(2)}(t_0)}{24 y(t_0)} \right]_{\psi=0} = -\frac{1}{24\sqrt{2\pi}} \left(\frac{T_i}{m_i c^2} + \frac{S_k^2}{d_1^2 \lambda_0^2} \right)^{-1} \left(\frac{\Delta v_0}{c} \right)^2. \quad (5.64)$$

As expected, we find that the broadening associated with the ion temperature and the instrument function determines what changes in velocity are needed to produce a appreciable perturbation to the spectrum. Solving the above for the velocity change required to produce a 1% perturbation at $\psi = 0$, $T_i = 4$ keV and without instrument function effects we obtain $\Delta v_0 \approx 48$ Km/s. This change in velocity is at least an order of magnitude larger than any that could be expected over one integration time, and still produces only a 1% perturbation at the peak of the spectrum. On this basis we may conclude that linear changes in velocity have no appreciable or detectable effect on the observed CER spectrum.

5.5.2 Simultaneous linear changes in v_0 , T_i and R_γ

When (v_0, t_i, R_γ) are changing simultaneously, it is no longer the case that the largest change in the spectrum always occurs at $\psi = 0$. Here we also look at changes in the complete model $C_n(\theta)$ rather than just the time-dependent part $y(t)$. Let $\tilde{C}_n(\theta)$ be the ‘static’ model where (v_0, t_i, R_γ) remain constant over the integration time. We use the following metric to interpret the differences between the static and time-dependent models:

$$\epsilon = \left| \frac{\max(C_n(\theta) - \tilde{C}_n(\theta))}{\max(\tilde{C}_n(\theta))} \right| \quad (5.65)$$

ϵ is the maximum absolute change between the two models as a fraction of the peak value of the static model. This allows ϵ to be expressed as a percentage making it easy to interpret. As we have specified that all changes are linear, it is convenient to calculate ϵ as a function of the total change in (v_0, t_i, R_γ) across the integration time, i.e. $\epsilon = \epsilon(\Delta v_0, \Delta T_i, \Delta R_\gamma)$. The results of calculating ϵ are summarised in figure 5.5. Slices through planes of constant ΔR_γ are shown to illustrate the variation with ΔR_γ . The planes with negative ΔR_γ have been omitted as they are identical to the corresponding positive ΔR_γ planes, except rotated through π radians. Consistent with the prediction in section 5.5.1 we see that exceptionally large linear changes in velocity are needed to produce even small changes to the spectrum. The changes in temperature required to produce a change of $\epsilon = 1\%$ are less extreme, but still very large at $\Delta T_i \sim 2$ keV. We also note that the changes in R_γ introduce an asymmetry between positive/negative changes in the velocity and temperature which are not present when $\Delta R_\gamma = 0$. This asymmetry makes changes in the spectrum easier to produce for certain changes in velocity and temperature, but not by a meaningful amount.

It is therefore likely infeasible to infer information regarding the time-evolution temperature, density or flow velocity on time-scales less than the integration time, as for fusion-relevant plasma conditions any such time-evolution has too subtle an affect on the experimental data as to be reasonably detected.

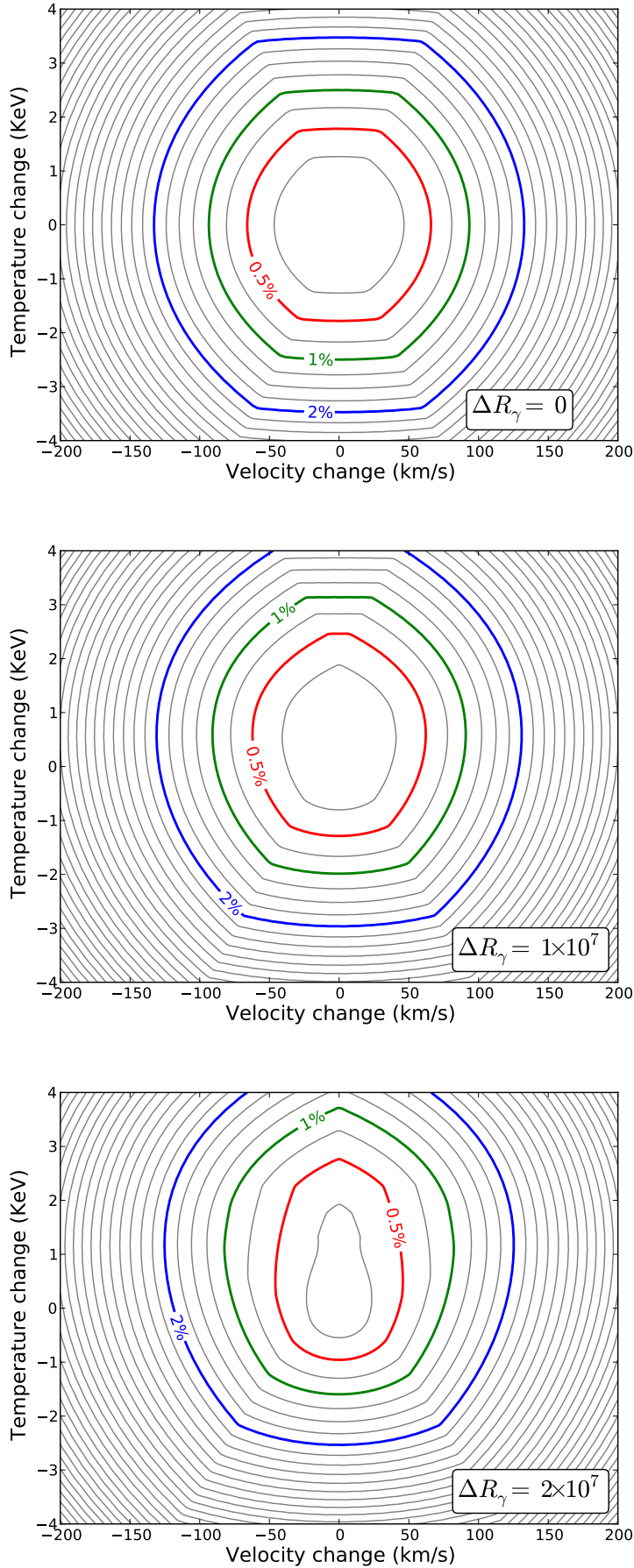


Figure 5.5: Contour plots of ϵ from (5.65). The plasma conditions used to generate these results are $v_0 = 20$ Km/s, $T_i = 4$ keV and $R_\gamma = 5 \times 10^7$ s $^{-1}$.

Table 5.1: Values for the various parameters which define the experimentally determined instrument function used in the framework validation. These values are taken from the tangential#03 chord for shot #141948. The way in which these parameters are incorporated into the spectrum model is discussed in section 5.3.3.

i	1	2	3	4	5	6
A_i	0.0510733	0.0141003	0.0368144	0.136463	0.500188	0.261359
L_i	-8.01830	-9.83847	8.15435	-5.36806	3.11777	-2.21490
S_i	1.30378	0.893262	1.57581	1.86573	3.13346	2.44473
d_i	2.439×10^4	-4.58×10^{10}				

5.6 Inference validation using simulated data

In order to test the implementation of the inference scheme we first generate the expected counts using (5.43) for some chosen parameters $\underline{\theta}$. Simulated measured counts data is then obtained through sampling from Poisson distributions as described in (5.27). The implementation can then be validated by comparing marginal distributions for the physics parameters derived from the simulated data with the actual values used to generate the data.

Here we give an example of results obtained using this validation procedure. The data was simulated for the tangential#03 chord, the instrument function and dispersion coefficients for which are given in table 5.1. R_γ , T_i and v_0 were taken to be static in accordance with the conclusions of section 5.5 - additional insight cannot be gained by allowing these parameters to vary over the integration time. The model for the background $\beta_n(\underline{u})$ was taken to be linear such that

$$\beta_n(\underline{u}) + u_1 x_n + u_0. \quad (5.66)$$

An example of simulated counts data, along with the spectrum model used to generate it is shown in figure 5.6. Here each detected photon is assumed to produce a CCD count - this is reasonable for validation purposes, but calibration data for the CCD would be required for analysis of experimental data. GridFill (discussed earlier in chapter 3) was used to calculate marginal distributions for parameters of interest for the simulated data. These results, plus estimates obtained from a least-squares treatment of the problem are given in figure 5.7.

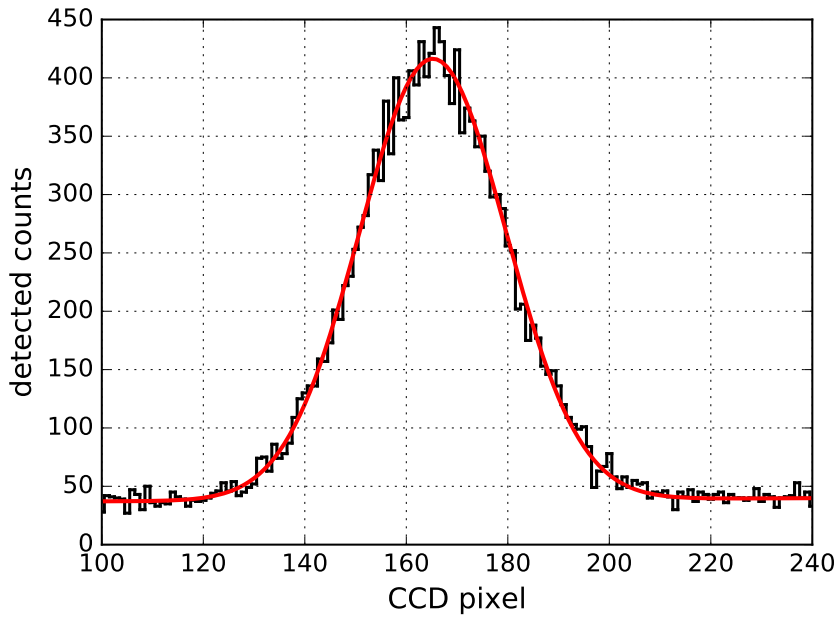


Figure 5.6: The expected counts is plotted in red, and one possible simulated dataset drawn from the expected counts is plotted in black. The parameters used to generate this data are $v_0 = 13 \text{ Km/s}$, $T_i = 3.5 \text{ keV}$, $R_\gamma = 5 \times 10^7 \text{ s}^{-1}$, $b_0 = 35$, $b_1 = 0.02$ and $t_i = 274 \mu\text{s}$.

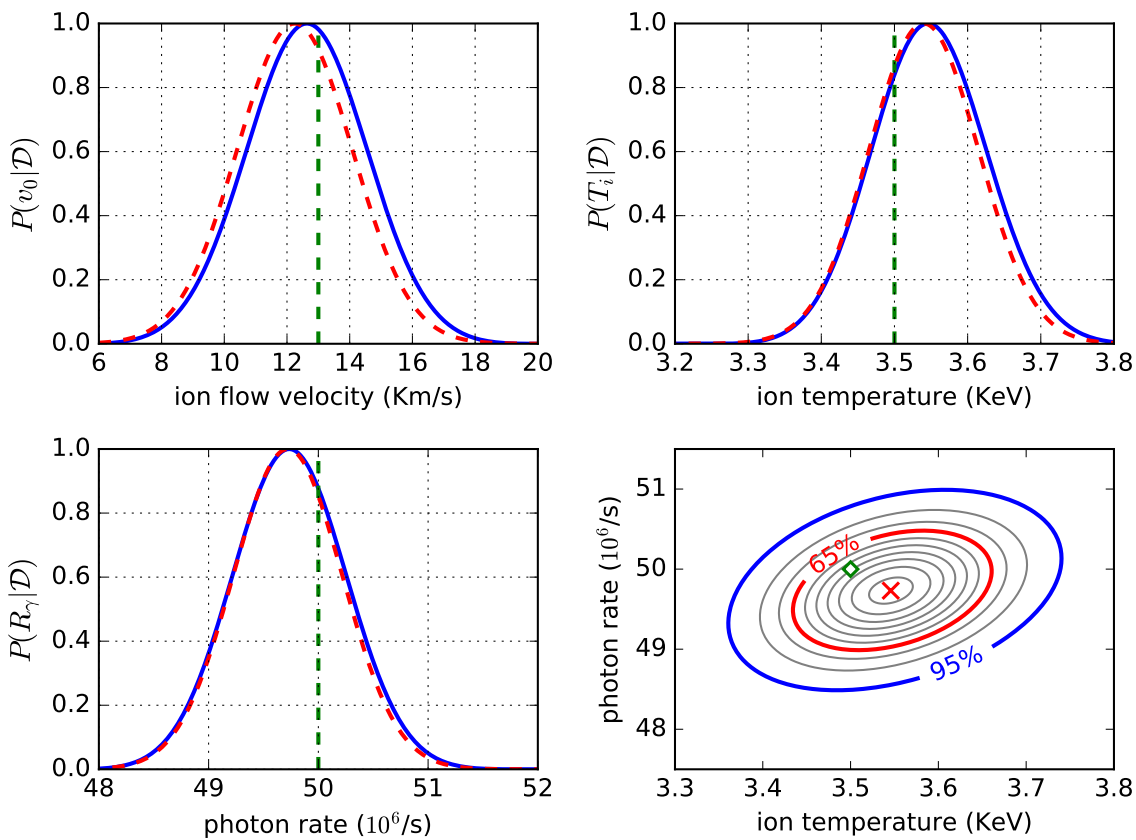


Figure 5.7: Summary of inference results derived from the simulated data. Inferred marginal distributions are shown in blue, estimates from least squares fitting in red and the actual values in green.

Agreement between the calculated marginal distributions and the actual parameter values used to generate the simulated data indicate that the inference framework works as intended. For some parameters very close agreement between the Bayesian and least-squares estimates is seen. To fully assess the performance of the Bayesian parameter estimates versus those obtained from least-squares, this process could be automated to analyse thousands of simulated datasets. The distribution of probability densities at which the correct parameter values occur for both approaches can then be used to draw conclusions regarding estimation performance - this is a potential subject of further work.

5.7 Summary

In this chapter a framework for the Bayesian inference of certain physics parameters using the DIII-D charge-exchange spectroscopy system was presented. A graphical model was used to construct the probability that a randomly selected photon leaving the spectrometer would be detected in a given CCD pixel. It was then shown that these detection probabilities result in a binomial distribution of observed CCD counts, which under experimentally-relevant conditions is very well approximated by the Poisson distribution. This allowed the construction of a likelihood function for the data, and in turn a posterior distribution for the model parameters. In order to reduce the computational expense of the posterior calculation, various approximations were proposed and their accuracy and range of validity was assessed.

The spectrum model was then used to investigate whether perturbations to the predicted spectra arising from time-evolution of the temperature, density and flow during the integration time could be used to infer the dynamics of these quantities on sub-integration time-scales. This idea was tested theoretically in the simplified case of only linear velocity changes, and numerically for the more general case of simultaneous linear changes in all 3 parameters. It was concluded that time variation of the parameters of the sort that could be reasonably expected in DIII-D experiments does not result

Chapter 5. Bayesian CER analysis on DIII-D

in perturbations to the spectrum which are significant enough to allow us to extract useful information.

As part of future work we plan to generate simulated datasets containing flow velocity oscillations of various amplitudes and frequencies, and use the inference framework presented here to attempt to recover the time variation. This will allow us to establish what types of flow oscillation can be reasonably characterised by the CER system, which in turn will assist in guiding experiment and choosing which data is merits analysis.

Chapter 6

Summary & Conclusions

The threat of climate change and the limited nature of fossil fuels demands that, in the near future, we as a global society make significant changes to how we produce and consume energy. If we are to remove our dependence on fossil fuels a sustainable, high-output and carbon-neutral source of energy is needed. Nuclear fusion meets all these criteria and is a promising long-term solution, having fuel reserves which will last a minimum of several thousand years. Realising fusion energy has proved to be a huge challenge, but incredible progress has been made over the last half-century and this looks to continue with the ITER project on the horizon.

In this thesis we investigated the application of Bayesian probability theory to several problems in magnetic confinement fusion data analysis. Bayesian probability theory is a framework for inductive logical reasoning through probabilities, and when applied to problems in data analysis offers advantages over conventional techniques. An introduction to the theory was presented by first discussing some fundamental mathematical results, and then demonstrating the application of these results through several examples.

The first of the three research chapters presented focused on the challenges surrounding numerical integration in Bayesian data analysis. Calculation of marginal distributions from many-dimensional posteriors is typically achieved through Markov-chain Monte-Carlo methods. While undoubtedly very useful, MCMC does have drawbacks, and this

fact motivated an investigation into whether a more advanced grid-based approach could be a viable alternative. A new approach to characterising many-dimensional posterior distributions was developed and implemented as the ‘GridFill’ algorithm. By evaluating only the areas of the probability space containing significant density, GridFill was shown to be highly efficient in comparison with conventional grid-based approaches. While the current implementation has applicability for relatively low-dimensional problems, it was found that it cannot currently compete with MCMC methods for high-dimensionality problems. The fundamental causes of this limitation were discussed at length, and a modification to the algorithm was proposed which will address these problems. Even without these proposed improvements, GridFill was shown to outperform an MCMC scheme in a 5D test-case, and has been usefully exploited to calculate marginal distributions for several problems discussed in this thesis.

Credible regions are an important tool in the interpretation of inference results, but calculating the probability density which defines the boundary contour of any such region requires an unusual integration over the distribution which is challenging using regular grids. We demonstrated that a semi-continuous distribution for the boundary density can be constructed from any random sample drawn from the distribution. This offers an easier and more elegant means of calculating boundary densities, and because the posterior for the density is known, the uncertainty can be reduced to whatever level is required. Effective means of presenting inference results, particularly in the case of two-dimensional distributions were also discussed. We proposed a standardised approach where the distribution is visualised using the boundary contours of a series of credible regions containing a fixed set of probabilities. We argue that this approach easily conveys important quantitative information about the results to the reader in ways colour density plots cannot.

An experiment studying the stability of neo-classical tearing modes using the KSTAR ECEI system motivated an investigation into applying probability theory to the discrete Fourier transform as a means of correcting for random noise. The problem was examined first in terms of the real and imaginary Fourier components, and it was shown that a correction was possible but was determined entirely by the joint prior for the

noise-free Fourier components. A change to polar coordinates was made, and a correction to the magnitude was derived. To calculate the correction the prior distribution for the noise-free Fourier magnitudes is required, and we showed that this can be obtained as the solution of a 1D integral equation inverse problem. It was demonstrated that the integral equation could be transformed in several ways which made the problem easier to attack.

Several approaches to obtaining approximate solutions to the inverse problem were developed and tested. First, an iterative approximation constructed using probability identities was presented, and was shown to yield a solution to the integral equation if successive iterations converged. A second approach based on using a complete orthonormal basis to linearise the integral equation was also investigated. Chebyshev polynomials were chosen as the basis, and a prior distribution for the basis coefficients was constructed in such a way as to keep the location of the posterior mode analytically obtainable.

Of the various prior approximations, the iterative approach was determined to be the most robust when tested, and also yielded correction performance similar to that obtained in the ideal case of an exact prior. The testing was based on correcting many sets of simulated data generated by adding different sets of Gaussian noise to a known reference signal. The difference between the ratio of the initial and post-correction noise standard deviation δ_c/δ_i was used as a metric for correction performance. This was calculated as a function of the ratio of the power in the noise to that in the true signal \mathcal{U} , which was used to parametrise the noise-level. In the limit of $\mathcal{U} \rightarrow 0$, the correction offered no additional reduction in the noise level, as we would expect. As \mathcal{U} was increased δ_c/δ_i was shown to fall rapidly at first, leading to significant noise reduction for $\mathcal{U} \geq 0.1$.

Further work was done to automate the correction procedure such that it could be applied to large datasets without by-hand analysis. Following this, the correction was applied to KSTAR ECEI data as part of an experiment investigating heat transport around magnetic islands and its impact on tearing-mode stability. As part of further work on tearing stability, the corrected KSTAR data will be used to derive marginal

Chapter 6. Summary & Conclusions

distributions for the critical island width w_c . Although it was this KSTAR work which motivated the development of the correction technique it is completely general, making no assumptions regarding the data to be corrected. The technique may therefore have wider applicability in fusion data analysis, and generally in signal processing.

Experiments on DIII-D attempting to characterise fast fluctuations in ion flow velocity due to magnetic islands motivated an investigation into the limits of the information that could be extracted from the data. A model for CCD photon detection probability was constructed using a Bayesian network approach, which was in turn used to construct a model for the observed data and then the posterior distribution for the model parameters. The behaviour of the spectrum model in the presence of time-varying temperature, density and flow was assessed numerically in the general case and analytically in a simplified case. It was shown that in order to produce non-negligible changes to the observed data, extreme time-variation of these physical quantities is required during the integration time. As this level of variation is far beyond what is currently expected in tokamak experiments, we concluded that inferring the dynamics of these quantities on sub-integration time-scales is not feasible.

Appendix - Estimation of tearing stability parameters using KSTAR ECEI data

Improved accuracy in the estimation of the tearing mode stability parameters (Δ' and w_c) using 2D ECEI data in KSTAR

Minjun J Choi¹, Gunsu S Yun¹, Woochang Lee¹, Hyeon K Park², Young-Seok Park³, Steve A Sabbagh³, Kieran J Gibson⁴, Christopher Bowman⁴, Calvin W Domier⁵, Neville C Luhmann Jr⁵, Jun-Gyo Bak⁶, Sang G Lee⁶ and the KSTAR Team⁶

¹ Pohang University of Science and Tehcnology, Pohang, Gyungbuk 790-784, Korea

² Ulsan National Institute of Science and Technology, Ulsan, Gyungbuk 689-798, Korea

³ Columbia University, New York, NY 10027, USA

⁴ York Plasma Institute, Department of Physics, University of York, Heslington, YO10 5DD, UK

⁵ University of California at Davis, Davis, CA 95616, USA

⁶ National Fusion Research Institute, Daejeon 169-148, Korea

E-mail: minjun.choi@postech.edu

Received 14 February 2014, revised 17 April 2014

Accepted for publication 7 May 2014

Published 3 June 2014

Abstract

The accuracy in estimation of two important tearing mode stability parameters (Δ' and w_c) is improved by employing two-dimensional (2D) ECE imaging data which help one to overcome the resolution limit of conventional one-dimensional data. The experimentally measured 2D images are directly compared with synthetic ones from a tearing mode T_c model to estimate the parameters and an excellent agreement is achieved. The results imply that the observed tearing mode is classically stable but has non-negligible bootstrap current drive.

Keywords: tearing mode stability, electron cyclotron emission imaging, synthetic diagnostic

1. Introduction

The tearing mode is an internal resistive instability which tears the nested magnetic flux surfaces and forms a magnetic island across the rational flux surface in tokamak plasmas. The magnetic island of this mode reconnects the inner and outer regions of the rational surface. When the island size is sufficiently large so that the cross-field transport effect is negligible, the pressure profile inside the island is flattened due to rapid parallel transport along the connected field line [1]. Since the large island with the flattened pressure profile prevents high β plasma operation and often leads to a disruption, a precise understanding of the magnetic island dynamics has been an important issue and studied actively.

The temporal dynamics of the magnetic island of the tearing mode has been understood within the frame of the modified Rutherford equation (MRE) [2] as given in the following:

$$a_1 \frac{\tau_r}{r_s} \frac{dw}{dt} = r_s \Delta' + a_2 r_s \sqrt{\epsilon} \beta_\theta \frac{L_q}{L_p} \frac{w}{w^2 + w_c^2} + \dots, \quad (1)$$

where w is the island half-width, a_1 and a_2 are coefficients related to the flux surface geometry, r_s is the minor radius of the rational flux surface, $\tau_r = \mu_0 r_s^2 / \eta$ is the current diffusion time where η is the plasma resistivity, ϵ is the inverse aspect ratio, β_θ is the plasma poloidal beta and $L_q = q/q'$ and $L_p = p/p'$ where q is the safety factor, p is the total pressure and the prime denotes the radial derivative. The first term with the nonlinear classical tearing stability index Δ' is related to the equilibrium current profile, which can be either stabilizing or destabilizing. The second term is the neoclassical destabilizing term which stems from the loss of bootstrap current due to pressure flattening inside the island. w_c is the critical half-width for the pressure flattening. When the second term is dominant, it becomes the neoclassical tearing mode which is known to be harmful for high β plasma operation [3]. Terms from the polarization current and magnetic field curvature are omitted, because they are known to be important near the onset of tearing mode which is not considered in this paper.

Identification of the main driving/decaying mechanism of the large magnetic island is important for steady-state, high β

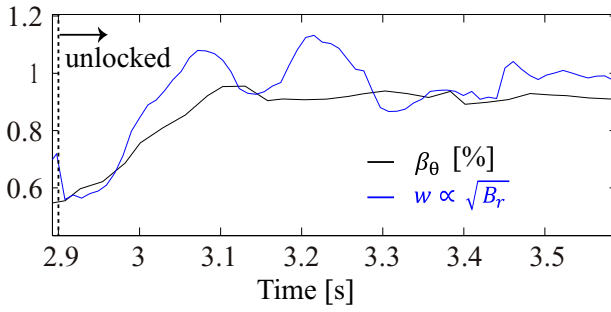


Figure 1. The plasma poloidal beta β_θ and the normalized island half-width are drawn together. The island half-width is normalized by the half-width at 3.25 s.

plasma operation. In order to develop a control method based on growth dynamics of the MRE, an accurate determination of the two stability parameters, Δ' and w_c , is essential among the parameters in (1). Numerous studies [4–6] with conventional one-dimensional (1D) experimental data have been performed to model the magnetic island T_e structure of the tearing mode and determine those parameters. However, the estimated Δ' and w_c based on 1D experimental data have been limited to the uncertainty from insufficient spatial resolution of the data [5]. Techniques such as radial plasma jogging were introduced to reduce the uncertainties [4], under the assumption that the perturbation from jogging does not influence the stability of the tearing mode.

The two-dimensional (2D) electron cyclotron emission imaging (ECEI) diagnostic is ideal for the study of various MHD instabilities [7–10] and has provided 2D T_e fluctuation data with an unprecedented high temporal and spatial resolution. In section 2, the detailed magnetic island structures measured by the 2D ECEI diagnostic in KSTAR plasmas are provided with a brief description of the ECEI system. The T_e model [5, 6] to be compared with the measurements for determination of Δ' and w_c is introduced in section 3. Statistical analysis by comparison of the modelled data with the measured ones (1D and 2D data) is performed and a clear advantage of 2D data is demonstrated in section 4. A summary follows at the end.

2. The 2D magnetic island structure of tearing mode visualized by ECEI

The $m/n = 2/1$ magnetic island of the tearing mode has been observed in the KSTAR discharge # 7131. The toroidal field at the major radius was 1.96 T and the plasma was heated by two NBI with the total power of 3 MW. The 170 GHz ECRH power at 0.3 MW was turned on from 3.01 to 3.50 s. The plasma current was constant at 600 kA. The time evolution of the plasma poloidal beta (β_θ) and half-width (w) of the $m/n = 2/1$ island are depicted in figure 1. The half-width of the island is estimated from the Mirnov coil fluctuation amplitude divided by fluctuating frequency ($\int \dot{B} dt \approx \dot{B}/f$), and this quantity is normalized by the half-width at 3.25 s. The mode locking and unlocking due to the magnetic island have repeated in this plasma and the β_θ and w have evolved with the state of the plasma. The unlocked phase starts from 2.9 s in figure 1. As the β_θ recovers in time, the w also increases. This correlation

may suggest that the observed mode has the finite neoclassical driving term in (1). Estimation of Δ' and w_c is necessary for more accurate analysis of the tearing mode dynamics, and the 2D ECEI diagnostic data near the $2/1$ magnetic island around 3.25 s has been obtained for that purpose.

The 2D ECEI diagnostic measures high-resolution (space and time) images of the local electron temperature fluctuations near the $m/n = 2/1$ magnetic island produced by the tearing mode as shown in figure 2(a). The 2D image (40 cm \times 12 cm) consists of 192 pixels (24 detectors array and each detector has 8 horizontal channels). Each pixel represents the normalized fluctuations $\frac{\delta T_{e,ECEI}}{\langle T_{e,ECEI} \rangle_t} = \frac{T_{e,ECEI} - \langle T_{e,ECEI} \rangle_t}{\langle T_{e,ECEI} \rangle_t}$, where $\langle \rangle_t$ means time average for many fluctuation periods. As the magnetic island structure rotates in the laboratory frame, different phases of the island are captured at different times. The first image in figure 2(b) corresponds to the image of the X-point phase (t_1) when the X-point of the magnetic island is at the centre of the ECEI view. The ECE images at four different phases (t_1 – t_4) cover the entire structure of the magnetic island. The channel in the region of $r < r_s$ will detect higher temperatures (inner flux) at the X-point phase, but the channel at $r > r_s$ will measure lower temperatures (outer flux) at the same time. This results in the phase inverted temperature fluctuations across the rational surface. The measured 2D data of $\delta T_{e,ECEI}/\langle T_{e,ECEI} \rangle_t$ will be compared with the synthetic 2D normalized T_e fluctuations from the T_e model of the magnetic island to determine Δ' and w_c .

Even though the instrumental spatial resolution of the 2D ECEI diagnostic in (R, Z) is similar to that of the conventional 1D ECE diagnostic, the effective resolution of the 2D data in (r, ζ) space can be much finer due to its 2D nature as illustrated in figure 2(c). Note that ζ is the helical angle in the direction perpendicular to the magnetic field at r_s . For example, the horizontal channels of the single detector of the ECEI diagnostic can be considered as the conventional 1D ECE diagnostic, and the horizontal channels have a separation distance of ~ 2.0 cm. The separation distance could not be reduced much in the 1D diagnostic to allow enough bandwidth for an adequate signal to noise ratio. However, the effective separation distance can be smaller than 1.0 cm with additional independent detectors in the 2D diagnostic as shown in figure 2(c). The channels from different detector row fill the r space by overlapping each other without loss of signal-to-noise ratio. Therefore, the 2D ECEI diagnostic can provide a fine resolution measurement of the magnetic island T_e structure.

3. The T_e model for Δ' and w_c estimation

3.1. Definition of Δ' and w_c

In this section, a brief description of the nonlinear classical stability parameter (Δ') and critical island half-width (w_c) of the tearing mode is given with basic principle employed in estimation of the parameters. From Maxwell's equation and Ohm's law, diffusion of the radial magnetic field B_r can be written as

$$\frac{\partial B_r}{\partial t} \approx \frac{\eta}{\mu_0} \frac{\partial^2 B_r}{\partial r^2}. \quad (2)$$

Using the helical magnetic flux notation $B = \nabla\psi \times \hat{e}_\phi$ with single-helicity assumption where ψ is the helical magnetic

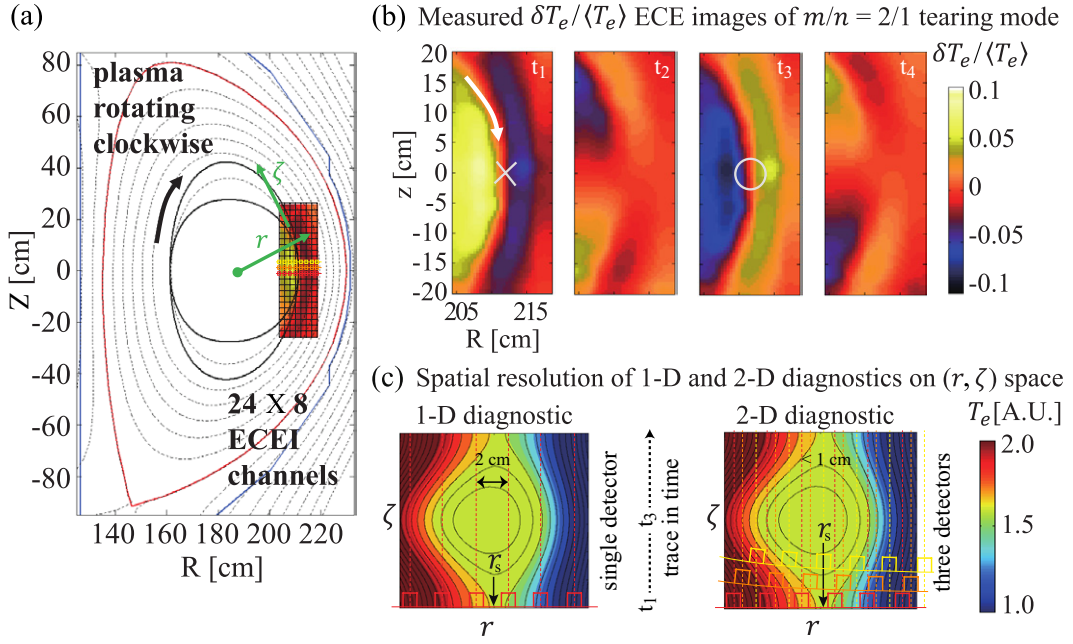


Figure 2. (a) The 192 pixels (24 detectors \times 8 horizontal channels) of the 2D ECE image near the $m/n = 2/1$ island in the plasma are shown. Perturbed magnetic flux surfaces of the island are illustrated with black lines over the EFIT reconstructed equilibrium (dashed lines). Coloured boxes represent measurement area of channels of three detectors in (R, Z) space. (b) Four images at different phases of the magnetic island are plotted as it rotates in time around 3.25 s. The X-point and O-point of the island are indicated with the white X and O marks, respectively. (c) The effective spatial resolution in (r, ζ) space is significantly improved in the 2D diagnostic. Coloured boxes represent measurement area of the channels in (r, ζ) space. Additional detectors allow fine radial measurements of the magnetic island T_e structure.

flux function and \hat{e}_ϕ is unit vector along magnetic field at r_s and employing the relation $B_r \propto w^2$ and constant ψ approximation, it is integrated into

$$\frac{dw}{dt} \sim \frac{\eta}{2\mu_0} \frac{\psi'}{\psi} \Big|_{r_s-w}^{r_s+w}. \quad (3)$$

The relative difference in ψ' is defined as $\Delta'(w) \equiv \frac{\psi'}{\psi} \Big|_{r_s-w}^{r_s+w}$, where $r_s \pm w$ are the magnetic island boundaries. Now, Δ' can be determined if the magnetic flux function is known and the sign of Δ' implies either the growth or decay of the island width as shown in (3).

w_c is the critical half-width above which temperature is flattened inside the magnetic island [1]. It was derived as $\sqrt{\frac{RqL_q}{m} \left(\frac{\kappa_\perp}{\kappa_\parallel}\right)^{1/4}}$ by balancing between parallel and perpendicular heat transport where κ_\parallel and κ_\perp are the parallel and the perpendicular thermal conductivity, respectively [1, 2].

Without a significant heat source or sink, the heat flow $q = -\kappa_\parallel \nabla_\parallel T_e - \kappa_\perp \nabla_\perp T_e$ will have zero divergence,

$$\kappa_\parallel \nabla_\parallel^2 T_e + \kappa_\perp \nabla_\perp^2 T_e = 0. \quad (4)$$

In general, the parallel thermal conductivity is much larger than the perpendicular one and the perpendicular transport term is often neglected. However, if the perpendicular term is finite, or $w \sim w_c$, the perpendicular transport changes the temperature profile inside the island in which the temperature does not follow the magnetic flux contours [1]. Therefore, temperature distribution over the island can be the measure of w_c .

3.2. The T_e model in the vicinity of the magnetic island

The model for T_e in the vicinity of the magnetic island can be obtained by solving (4) over the properly modelled magnetic geometry. The helical coordinates (r, ζ, ϕ) with the helical angle $\zeta = m\theta - nz/R_0$ are used in this modelling [5]. With $\kappa_\parallel/\kappa_\perp \gg 1$, equation (4) can be rewritten as

$$\left[\frac{\kappa_\parallel}{\kappa_\perp} \nabla_\parallel^2 + \nabla_\perp^2 \right] T_e = 0. \quad (5)$$

The Laplacian is approximated as $\nabla^2 \approx \frac{\partial^2}{\partial r^2} + \left(\frac{m}{r_s}\right)^2 \frac{\partial^2}{\partial \zeta^2}$ in this equation, and the parallel gradient will be derived from the helical magnetic flux notation of magnetic field and slab geometry assumption as shown in the below:

$$\begin{aligned} \nabla_\parallel &= \hat{b} \cdot \nabla = \frac{1}{|B|} \left[\begin{array}{c} -\frac{m}{r_s} \psi_1 \sin \zeta \\ -\frac{\partial \psi_0}{\partial r} - \frac{\partial \psi_1}{\partial r} \cos \zeta \end{array} \right] \cdot \left[\begin{array}{c} \frac{\partial}{\partial r} \\ \frac{\partial}{\partial \zeta} \end{array} \right] \\ &= -\frac{m}{r_s |B|} \left(\psi_1 \sin \zeta \frac{\partial}{\partial r} + \psi_0' \frac{\partial}{\partial \zeta} + \psi_1' \cos \zeta \frac{\partial}{\partial \zeta} \right), \end{aligned} \quad (6)$$

where ψ_0 is the equilibrium helical magnetic flux function and ψ_1 is the perturbed flux function.

The equilibrium magnetic flux function will take the form of $\psi_0(r) = \frac{\mu_0 I_0}{8\pi} \left(\left(\frac{r}{a}\right)^2 - \left(\frac{r_s}{a}\right)^2 \right)^2$ from the parabolic current profile assumption where I_0 is the peak value of the plasma current profile. The perturbed magnetic flux function will be modelled with three dimensionless parameters, α , β and γ , as [5]

$$\begin{aligned} \psi_1(r) &= \frac{\mu_0 I_0}{8\pi} \alpha \left(\frac{r}{r_s} \right)^m \left(1 - \beta \frac{r}{r_s} \right) \quad \text{for } r \leq r_s \\ &= \frac{\mu_0 I_0}{8\pi} \left(\frac{\alpha(1-\beta) - \gamma + \gamma r/r_s}{(r/r_s)^{m+1}} \right) \quad \text{for } r > r_s. \end{aligned} \quad (7)$$

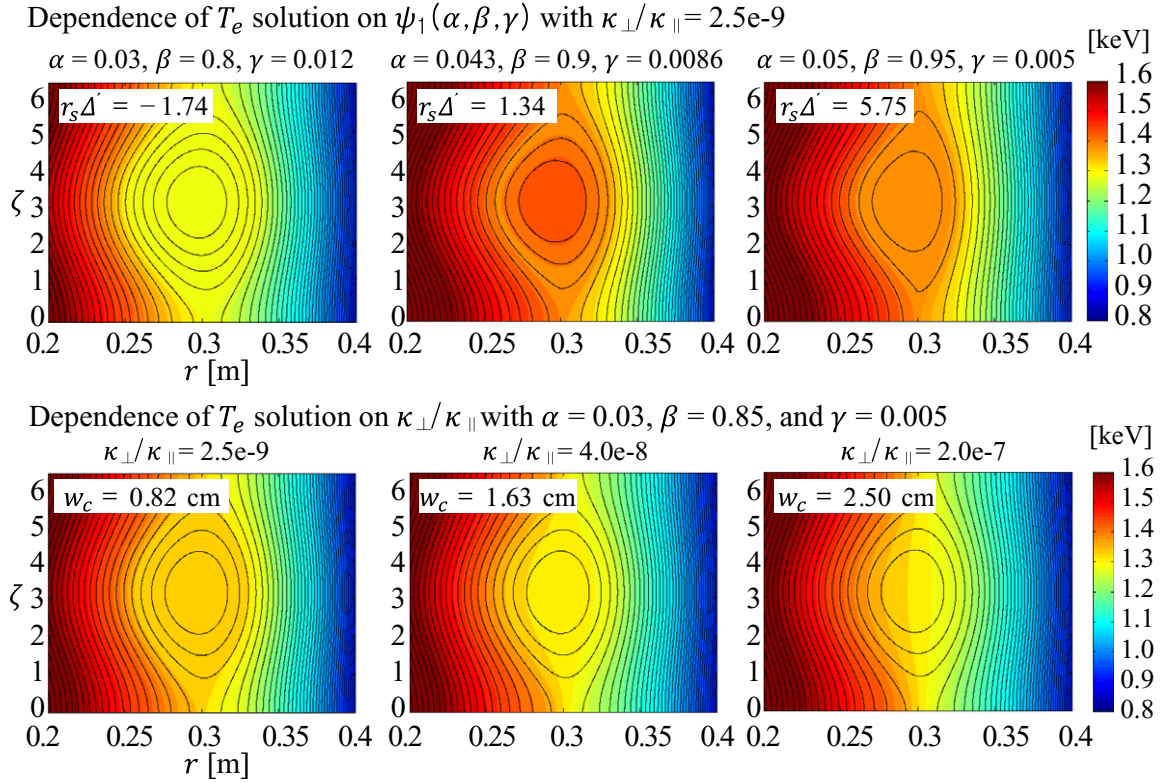


Figure 3. Dependence of T_e solution on four parameters ($\alpha, \beta, \gamma, \kappa_{\perp}/\kappa_{\parallel}$) is illustrated. Black line contours are magnetic flux function contours and colour contours are T_e contours. (a) The first three parameters (α, β, γ) determine the magnetic geometry of the island and examples for different Δ' are given. (b) $\kappa_{\perp}/\kappa_{\parallel}$ affects the perpendicular heat transport and determines the temperature distribution over the island. As the perpendicular conductivity increases, the temperature gradient inside the magnetic island increases.

This model function will behave in both limits $r \rightarrow 0$ and $r \rightarrow \infty$, satisfying vacuum solution of the tearing mode equation [5], and it can provide various forms of realistic flux function (well fitted into solutions of the tearing mode equation).

Equation (5) will be solved with (6) and (7) and boundary T_e values to obtain the $T_e(r, \zeta)$ profile near the magnetic island of the tearing mode (see appendix A). Figure 3 shows a parametric dependence of the T_e solution. The three parameters, α, β and γ , determine the magnetic flux geometry of the island through ψ_1 , and the conductivity ratio $\kappa_{\perp}/\kappa_{\parallel}$ affects the flatness of the T_e profile inside the island. Examples of the T_e solution for different $\Delta'(\alpha, \beta, \gamma)$ and $w_c(\kappa_{\perp}/\kappa_{\parallel})$ of the model are given in figure 3.

4. Comparative study between the measurements and synthetic images

4.1. Reconstruction of synthetic data from the T_e model

The T_e solution of equation (5) is converted into synthetic ECEI data in two steps. First, the synthetic 2D T_e data are reconstructed as if they are measured by the ECEI diagnostic by applying instrumental functions of the KSTAR ECEI system and emission theory. For example, each synthetic channel has the $T_{e,\text{syn}}$ value by

$$T_{e,\text{syn}} = \frac{\int \int T_e F_{\text{inst}}(R, Z) dR dZ}{\int \int F_{\text{inst}}(R, Z) dR dZ}, \quad (8)$$

where $F_{\text{inst}}(R, Z) = f(R) \cdot g(Z)$ is the 2D response function of the ECEI channel. $f(R)$ and $g(Z)$ have a finite coverage as prescribed by the detection frequency bandwidth and vertical coverage, respectively. The functional shape of $f(R)$ is calculated including the relativistic electron cyclotron radiation frequency downshift effect [11]. In the region where the 2/1 magnetic island is located, the reabsorption process minimizes the downshift effect and $f(R)$ is close to ideal frequency response of the channel. The functional shape of $g(Z)$ of the KSTAR ECEI diagnostic is known to be close to Gaussian shape [12]. Note that refraction effect due to the plasma density gradient is sufficiently small to be neglected in this case.

Second, the $T_{e,\text{syn}}$ is normalized by the time-averaged value $\langle T_{e,\text{syn}} \rangle_t$ such as $\frac{\delta T_{e,\text{syn}}}{\langle T_{e,\text{syn}} \rangle_t} = \frac{T_{e,\text{syn}} - \langle T_{e,\text{syn}} \rangle_t}{\langle T_{e,\text{syn}} \rangle_t}$. Since the plasma rotates in time, $\langle T_{e,\text{syn}} \rangle_t$ is essentially a time-averaged value along ζ . After normalization, the synthetic term, $\delta T_{e,\text{syn}}/\langle T_{e,\text{syn}} \rangle_t$, can be directly compared with the equivalent measured ECEI term, $\delta T_{e,\text{ECEI}}/\langle T_{e,\text{ECEI}} \rangle_t$. Basically, the structure of $\delta T_{e,\text{syn}}/\langle T_{e,\text{syn}} \rangle_t$ depends on the shape of the T_e solution which is deduced from four parameters ($\alpha, \beta, \gamma, \kappa_{\perp}/\kappa_{\parallel}$). Arbitrary initial boundary T_e values ($T_e(r = 0.1) = 2.1$ keV and $T_e(r = 0.4) = 0.9$ keV) introduced in solving the model equation only affect the overall amplitude of the $\delta T_{e,\text{syn}}/\langle T_{e,\text{syn}} \rangle_t$ and not its detailed shape. The solution can have a degree of freedom to have different boundary values in case the absolute T_e measurement at the boundary is absent. Here, a scale parameter A is introduced such as

$A \cdot \delta T_{e,\text{syn}} / \langle T_{e,\text{syn}} \rangle_t$ to allow different boundary values within the range $0.5 < A < 3.0$. The range of A is restricted for the physically reasonable variation of the boundary values. For an each model parameter set, the value of A is determined to give the minimum difference between the synthetic and experimental data.

4.2. Importance of higher resolution in synthetic data of the T_e model

High spatial resolution is important to resolve small variations of synthetic data from different T_e model parameters. In (r, ζ) space, the resolution on ζ axis can be increased by employing additional detectors or using more measurement points in time, but the radial resolution can only be increased by additional detectors (figure 2(c)). The improved radial resolution in 2D diagnostic can enhance the resolving power among the synthetic data sets with different T_e model parameters. This is demonstrated by comparing the synthetic data sets reconstructed from 1D and 2D measurements, respectively.

The seven horizontal channels on the midplane of the ECEI diagnostic system are selected to compose the 1D measurement. The synthetic data sets are reconstructed by the seven channels with the model parameter sets $\mathbf{p} = (\alpha, \beta, \gamma, \kappa_{\perp}/\kappa_{\parallel})$ over $(0.02 \leq \alpha \leq 0.04, 0.82 \leq \beta \leq 0.98, -0.012 \leq \gamma \leq 0.03, 4 \times 10^{-10} \leq \kappa_{\perp}/\kappa_{\parallel} \leq 2 \times 10^{-8})$ space. The $5^4 = 625$ combinations of \mathbf{p} over the four-dimensional parameter space are used to generate the synthetic data sets. The $\chi^2(\mathbf{p}_i, \mathbf{p}_j) = \frac{1}{2} \sum_{n=1}^N [y_n(\mathbf{p}_i) - \hat{y}_n(\mathbf{p}_j)]^2$ among the data sets are calculated to check the difference of a particular synthetic data set from other synthetic data sets with different T_e model parameters. N is the number of data points (channel number \times measurement points in time = $7 \times 67 = 469$), $y_n(\mathbf{p}_i)$ is the synthetic data set of the parameters \mathbf{p}_i with the hypothetical random system noise and $\hat{y}_n(\mathbf{p}_j)$ is the synthetic data set of \mathbf{p}_j without noise. The 67 measurement points in time are used to make the ζ resolution comparable to that of the 2D measurement. If the χ^2 difference between \mathbf{p}_i and \mathbf{p}_j is less than the system noise level ($\sqrt{((\partial \chi^2 / \partial y) \delta y)^2} = 0.0017$), the two parameter sets are not distinguishable. The calculation of $\chi^2(\mathbf{p}_i, \mathbf{p}_j)$ is repeated 20 times for different random system noises, and the average number of the parameter set whose synthetic data is indistinguishable with other synthetic data is 19 ± 3.3 out of 625 in the 1D measurement case.

The above processes are repeated with 2D measurement channels, i.e. 7 (horizontal channels) \times 20 (detectors) = 140 channels. In this case, 4 measurement points in time for each channel is used to make the ζ resolution and total number of data points $N = 7 \times 20 \times 4 = 560$ comparable with those of the previous case. However, the radial resolution is significantly improved with additional detectors. The average number of indistinguishable parameter set is 11.8 ± 2.7 , which means that the improved radial resolution results in enhanced resolving power. More clear distinction among the synthetic data sets allows higher confidence in the selected parameter set when they are compared with the experimentally measured data. This difference leads to more reliable and accurate estimation of Δ' and w_c through the usage of 2D measurements as shown in the following section.

4.3. Comparative analysis between the synthetic and measured data

The comparison between the synthetic data based on the model and experimentally measured data is non-trivial due to multi-variables (four parameters) of the model. The Levenberg–Marquardt Algorithm (LMA), known as the most standard multi-parameter fitting algorithm, is introduced for analysis. After the initial parameter set $\mathbf{p} = (\alpha, \beta, \gamma, \kappa_{\perp}/\kappa_{\parallel})$ is given with the Monte-Carlo method, it is updated towards the minimum $\chi^2(\mathbf{p}) = \frac{1}{2} \sum_{n=1}^N [y_n - \hat{y}_n(\mathbf{p})]^2$ difference through the gradient descent method and Gauss–Newton method. y_n is the measured data points and $\hat{y}_n(\mathbf{p})$ is the synthetic data points from the T_e model parameters \mathbf{p} . The goal of this algorithm is to find the parameter set that has a global minimum χ^2 .

Two independent LMA trials are exercised with the 1D and 2D measurement channels to demonstrate the accuracy of parameter determination in the high resolution 2D data. In the first trial the seven horizontal channels from the single detector on the midplane among the ECEI detectors array are selected to simulate the 1D measurement, and then the 140 channels from 20 detectors are used in the second trial. The results of the LMA fits for 1D data and 2D data are shown in figures 4(a) and (b). Figure 4(a) shows the dependence of χ^2 on four parameters in the 1D data trial. It has the minimum $\chi^2 = 0.0168$ at $\alpha = 0.0534$, $\beta = 1.000$, $\gamma = 0.0276$ and $(\kappa_{\perp}/\kappa_{\parallel})^{1/4} \sqrt{B_0} = 0.00366$, where B_0 is magnetic field strength at the plasma major radius R_0 . Note that the χ^2 includes the measurement error in ECEI data ($\sqrt{((\partial \chi^2 / \partial y) \delta y)^2}$) estimated as 0.0017 in the 1D data. In other words, the parameter sets whose χ^2 difference is less than this value are statistically indistinguishable. Therefore, a group of parameter sets which have $\chi^2 < 0.0185$ is selected (below the dashed line in figure 4(a)) for estimation of Δ' and w_c rather than a single parameter set.

The result of the 2D fit that has the minimum $\chi^2 = 0.0402$ at $\alpha = 0.0382$, $\beta = 0.949$, $\gamma = -0.00382$ and $(\kappa_{\perp}/\kappa_{\parallel})^{1/4} \sqrt{B_0} = 0.00691$ is shown in figure 4(b). The parameter sets of $\chi^2 < 0.0422$ are selected for further analysis considering the χ^2 error of 0.002 (below the dashed line in figure 4(b)). More data points used in the 2D case increased the propagated error on χ^2 .

Finally, $\Delta' = \frac{\psi'}{\psi} \Big|_{r_s-w}^{r_s+w}$ and $w_c = \sqrt{\frac{RqLq}{m} \left(\frac{\kappa_{\perp}}{\kappa_{\parallel}}\right)^{1/4}}$ calculated using the selected parameter sets of 1D (black squares) and 2D (red squares) fits are shown in figure 4(c). Note that the island separatrix estimated by the ECE images is used for the Δ' calculation and $w \sim 3$ cm at both ends. The distribution of Δ' and w_c values of each group is fitted with the Gaussian-function. The results are $r_s \Delta' = 7.653 \pm 2.251$ and $w_c = 0.899 \pm 0.154$ cm for 1D fit and $r_s \Delta' = -1.633 \pm 1.265$ and $w_c = 0.612 \pm 0.0726$ cm for 2D fit. The estimated $r_s \Delta'$ and w_c values from the 1D and 2D fits are very different, and the standard deviation of the 1D fit is significantly larger than that of 2D result in both $r_s \Delta'$ and w_c as expected from the previous section. Large standard deviation implies that the statistically selected parameter sets from the 1D fit have too large uncertainty to have a physically convergent solution. In fact, the result of the 1D fit has a non-physical perturbed flux function ψ_1 which does not converge to zero at the plasma boundary in contrast to the result from the 2D fit, meaning that

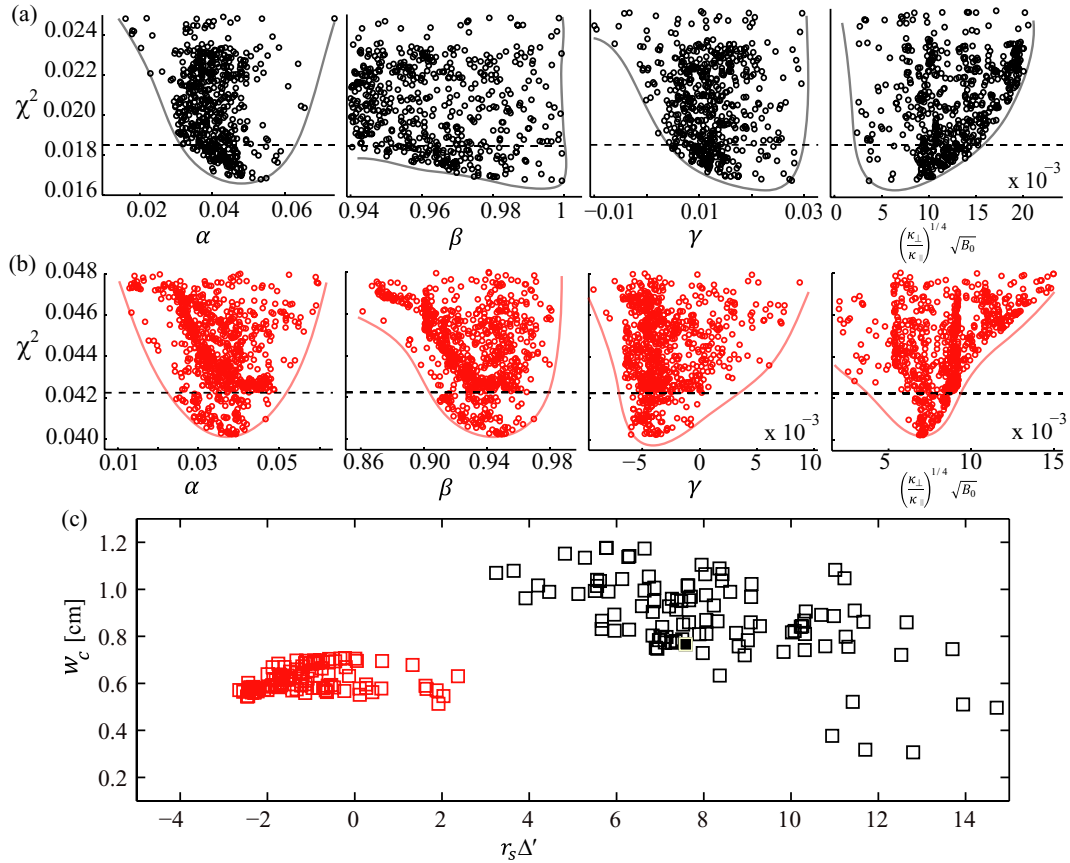


Figure 4. Parametric dependence of χ^2 from (a) 1D fit and (b) 2D fit. Small χ^2 parameter sets are selected (below the dashed line) for estimation of Δ' and w_c (c) Distribution of $r_s \Delta'$ and w_c from 1D (black squares) and 2D (red squares) fit. The result from 2D fit is statistically more convergent and also provides physically meaningful solution.

only the 2D fit results in physically meaningful output. Also, the stability calculation based on the ideal MHD theory (see appendix B) [13, 14] is consistent with the estimation of the 2D fit, i.e. classically stable. In conclusion, from the result of the 2D analysis, the negative $r_s \Delta' = -1.633 \pm 1.265$ represents that the tearing mode is classically stable and $w_c/w \sim 0.2$ implies that the pressure profile is almost flat and that the bootstrap current loss is not negligible.

Good agreement between the measured 2D experimental data and synthetic data at the minimum χ^2 parameter set is illustrated in figure 5. The upper trace in figure 5 is a point by point comparison of the measured and synthetic data sets. The 2D measured (upper) and synthetic (lower) ECE images at four different phases are compared and an excellent agreement at every phase provides a high confidence in the estimated values of Δ' and w_c .

5. Conclusion

High resolution 2D images of electron temperature fluctuations near the $m/n = 2/1$ magnetic island of the tearing mode were measured with the ECEI diagnostic in KSTAR plasmas. The important stability parameters of the tearing mode (Δ' and w_c) are estimated using the 2D $\delta T_{e,ECEI}/\langle T_{e,ECEI} \rangle_t$ data. The measured data were compared with the synthetic data from the T_e solution of the heat flow equation near the magnetic island. The T_e solution has four dependent parameters:

three parameters (α, β, γ) are associated with the magnetic geometry and the parameter $\kappa_{\perp}/\kappa_{\parallel}$ is associated with the perpendicular transport over the island. The importance of high resolution 2D data in estimation of Δ' and w_c is demonstrated by comparing with analysis of the self-consistent 1D data. The estimated tearing mode parameters using 2D data are $r_s \Delta' = -1.633 \pm 1.265$ and $w_c = 0.612 \pm 0.0726$ cm. The observed tearing mode is expected to be classically stable, but to have non-negligible neoclassical bootstrap current drive.

Acknowledgments

This work was supported by NRF Korea under grant no NRF-2009-0082507 and US DoE under contract No DE-FG-02-99ER54531. Two of the authors (KJG and CB) would like to acknowledge support from the UK Engineering and Physical Sciences Research Council under grant EP/H049460/1.

Appendix A. The heat flow equation

The heat flow equation for electron temperature can be rewritten with equation (6) as

$$\left[\frac{\kappa_{\parallel}}{\kappa_{\perp}} \left(\frac{m}{r_s |B|} \right)^2 \left(\psi_1 \sin \zeta \frac{\partial}{\partial r} + \psi'_0 \frac{\partial}{\partial \zeta} + \psi'_1 \cos \zeta \frac{\partial}{\partial \zeta} \right)^2 + \frac{\partial^2}{\partial r^2} + \left(\frac{m}{r_s} \right)^2 \frac{\partial^2}{\partial \zeta^2} \right] T_e = 0. \quad (\text{A.1})$$

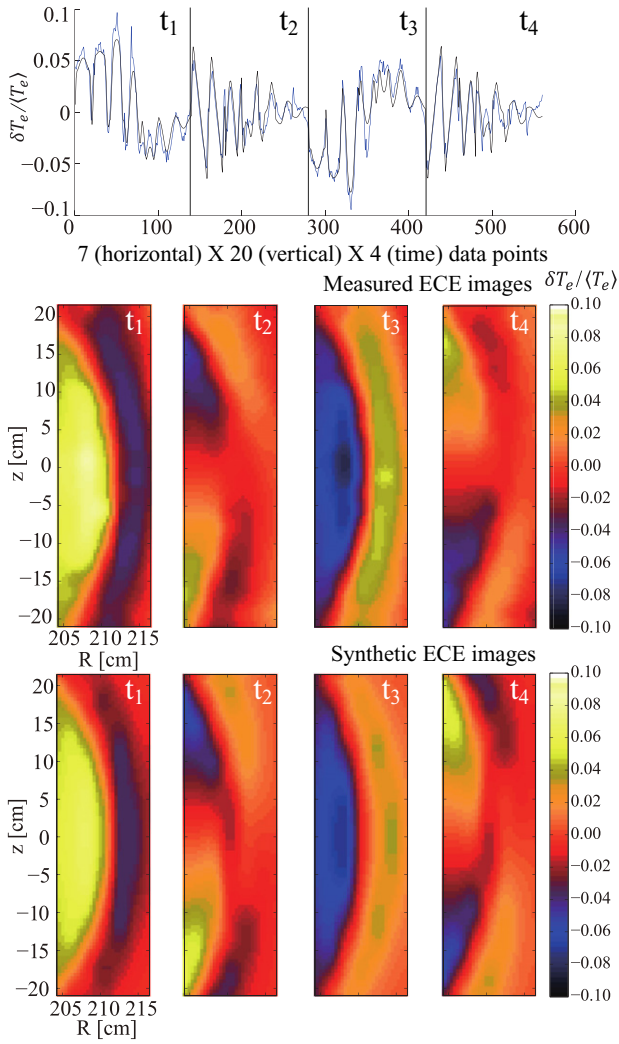


Figure 5. An excellent agreement between the measured images and the synthetic ones is shown. The parameter set of the minimum χ^2 in 2D fit was used to generate the synthetic images. The measured and synthetic images are matched well at all phases (t_1 – t_4) of the magnetic island.

In the above equation, T_e is expanded in Fourier series solutions,

$$T_e = \sum_{j=0} T_j(r) \cos j\zeta. \quad (\text{A.2})$$

Substitute (A.2) into (A.1), and then (A.1) is multiplied with $\frac{1}{2\pi} \cos k\zeta$ and integrated with respect to ζ to give the second order ordinary equation for each k as shown in below:

$$\sum_{j=0} a_{k,j} T_j'' + b_{k,j} T_j' + c_{k,j} T_j = 0, \quad (\text{A.3})$$

where $a_{k,j}$, $b_{k,j}$ and $c_{k,j}$ are corresponding coefficients and the prime denotes the radial derivative. This equation is now solved using the second order finite difference method with boundary T_e values and Fourier harmonics up to the 15th order.

Appendix B. Δ' calculation from the Ideal MHD theory

The tearing mode equation from the ideal MHD theory can be reduced as [13, 14]

$$\frac{d^2 \psi_1}{ds^2} - \frac{k}{s} \psi_1 = 0, \quad (\text{B.1})$$

where $k = -(\mu_0 j' q / B_\theta q')_{r_s}$, j' is the toroidal current gradient and $s = r - r_s$. The equation has a singularity at $r = r_s$. This second order ordinary differential equation is solved with the shooting method [14]. Form of two independent solutions near the rational surface r_s is known to be

$$\psi_1 = (1 + ks \ln |s| + \frac{1}{2} k^2 s^2 \ln |s| - \frac{3}{4} k^2 s^2) + A_\pm (s + \frac{1}{2} ks^2 + \frac{1}{12} k^2 s^3) \quad (\text{B.2})$$

and its radial derivative is

$$\psi_1' = k(\ln |s| + 1) + k^2(s \ln |s| - s) + A_\pm (1 + ks + \frac{1}{4} k^2 s^2) \quad (\text{B.3})$$

where A_- and A_+ are constants for $r < r_s$ and $r > r_s$ regions, respectively. The solution is restricted by the decaying boundary condition at both ends ($r = 0$ and $r = a$ where a is the plasma boundary). Arbitrary initial A_\pm values are tried and proper constants A_\pm which satisfy the boundary condition could be found by after some iterations. Then $\Delta'_{\text{ideal}}(w) = \frac{\psi_1'}{\psi_1} \Big|_{r_s-w}$ can be calculated with the solution ψ_1 . The result is $r_s \Delta'_{\text{ideal}}(w) = -4.12$, which means classically stable.

References

- [1] Fitzpatrick R. 1995 *Phys. Plasmas* **2** 825–38
- [2] Wilson H.R. 2004 *Fusion Sci. Technol.* **45** 123–31
- [3] La Haye R.J. 2006 *Phys. Plasmas* **13** 055501
- [4] Ren C., Callen J.D., Gianakon T.A., Hegna C.C., Chang Z., Fredrickson E.D., McGuire K.M., Taylor G. and Zarnstorff M.C. 1998 *Phys. Plasmas* **5** 450–4
- [5] Meskat J P, Zohm H, Gantenbein G, Günter S, Maraschek M, Suttrop W, Yu Q and the ASDEX Upgrade Team 2001 *Plasma Phys. Control. Fusion* **43** 1325–32
- [6] Snape J A, Gibson K J, O'Gorman T, Barratt N C, Imada K, Wilson H R, Tallents G J, Chapman I T and the MAST Team 2012 *Plasma Phys. Control. Fusion* **54** 085001
- [7] Park H K, Luhmann, Jr. N C, Donn e A J H, Classen I G J, Domier C W, Mazzucato E, Munsat T, van de Pol M J and Xia Z 2006 *Phys. Rev. Lett.* **96** 195003
- [8] Classen I G J, Westerhof E, Domier C W, Donn e A J H, Jaspers R J E, Luhmann, Jr N C, Park H K, van de Pol M J, Spakman G W, Jakubowski M W and the TEXTOR Team 2007 *Phys. Rev. Lett.* **98** 035001
- [9] Yun G S, Lee W, Choi M J, Lee J, Park H K, Tobias B, Domier C W, Luhmann, Jr N C, Donn e A J H, Lee J H and the KSTAR Team 2011 *Phys. Rev. Lett.* **107** 045004
- [10] Yun G S *et al* and the KSTAR Team 2012 *Phys. Rev. Lett.* **109** 145003
- [11] Hutchinson I H 2002 *Principles of Plasma Diagnostics* (Cambridge: Cambridge University Press) p 165
- [12] Liang T, Tobias B, Kong X, Domier C W, Luhmann N C Jr, Lee W, Yun G S and Park H K 2010 *Rev. Sci. Instrum.* **81** 10D909
- [13] Nishimura Y, Callen J D and Hegna C C 1998 *Phys. Plasmas* **5** 4292–9
- [14] Wesson J 2004 *Tokamaks* 3rd edn (New York: Oxford University Press) p 324

Bibliography

- [1] International Energy Agency. *Key World Energy Statistics 2015*. 2015.
- [2] Energy Information Authority. *International Energy Outlook 2016*. 2016.
- [3] BP. *BP Statistical Energy Review 2015*. 2015.
- [4] David MacKay. *Sustainable Energy-without the hot air*. 2008.
- [5] World Nuclear Association. *Nuclear Power in Germany*. 2016.
- [6] BBC. *Germany: Nuclear power plants to close by 2022*. 2011.
- [7] ITER organisation. *What is ITER?* 2016.
- [8] S. Atzeni. *The Physics of Inertial Fusion*. 2009.
- [9] ITER organisation. *Fuelling the Fusion Reaction*. 2016.
- [10] EFDA organisation. EFDA online image gallery (<https://www.euro-fusion.org/multimedia/new-picture-gallery/>). 2016.
- [11] J. Wesson. *Tokamaks*. 1997.
- [12] Paulett C. Liewer. Measurements of microturbulence in tokamaks and comparisons with theories of turbulence and anomalous transport. *Nuclear Fusion*, 25:543–621, 1985.
- [13] A. Costley. "Materials in fusion" lecture slides, Fusion doctoral training network. 2012.
- [14] G. T. Von Nessi, M. J. Hole, J. Svensson, and L. Appel. Evidence cross-validation and Bayesian inference of MAST plasma equilibria. *Physics of Plasmas*, 19(1), 2012.
- [15] J Svensson, A Werner, and JET-EFDA Contributors. Current tomography for axisymmetric plasmas. *Plasma Physics and Controlled Fusion*, 50(8):85002, 2008.
- [16] R. Fischer, C. Wendland, A. Dinklage, S. Gori, V. Dose, and W7-As Teams. Thomson scattering analysis with the Bayesian probability theory. *Plasma Physics and Controlled Fusion*, 44:1501–1519, 2002.
- [17] Minjun J Choi, Gunsu S Yun, Woochang Lee, Hyeon K Park, Young-Seok Park, Steve A Sabbagh, Kieran J Gibson, Christopher Bowman, Calvin W Domier, Neville C Luhmann, Jun-Gyo Bak, and Sang G Lee. Improved accuracy in the estimation of the tearing mode stability parameters using 2D ECEI data in KSTAR. *Nuclear Fusion*, 54(8):083010, 2014.

Bibliography

- [18] R. T. Cox. Probability, frequency and reasonable expectation. *American Journal of Physics*, 14(1):1–13, 1946.
- [19] Devinderjit Sivia and John Skilling. Data Analysis: A Bayesian Tutorial. *Technometrics*, 40(2):155, 1998.
- [20] Denis Coniffe. R.a. Fisher and the Development of Statistics - a View in His Centenary Year. *Journal of the Statistical and Social Inquiry Society of Ireland*, 26(3):55–108, 1990.
- [21] R. A. Fisher. *Statistical methods for research workers*. 1925.
- [22] H Jeffreys. An Invariant Form for the Prior Probability in Estimation Problems. *Proceedings of the Royal Society A*, 186, 1946.
- [23] P. Gregory. *Bayesian Logical Data Analysis for the Physical Sciences: A Comparative Approach with ‘Mathematica’ Support*. 2005.
- [24] Andrew Gelman, John B Carlin, Hal S Stern, and Donald B Rubin. *Bayesian Data Analysis*. 2004.
- [25] J. K. Kruschke. *Doing Bayesian Data Analysis*. 2011.
- [26] P. B. Brooks. Markov chain monte carlo method and its application. *The Statistician*, 1997.
- [27] Stephen P Brooks and Gareth O Roberts \tilde{A} . Convergence assessment techniques for Markov chain Monte Carlo. 1998.
- [28] Mary Kathryn, Bradley P Carlin, Mary Kathryn Cowles, and Bradley P Carlin. Markov Chain Monte Carlo Convergence Diagnostics : A Comparative Review. 91(434):883–904, 2016.
- [29] William A Link and Mitchell J Eaton. On thinning of chains in MCMC. 53:112–115, 2012.
- [30] G. S. Yun, W. Lee, M. J. Choi, J. B. Kim, H. K. Park, C. W. Domier, B. Tobias, T. Liang, X. Kong, N. C. Luhmann, and A. J H Don. Development of KSTAR ECE imaging system for measurement of temperature fluctuations and edge density fluctuations. *Review of Scientific Instruments*, 81(10):12–15, 2010.
- [31] J a Snape, K J Gibson, T O’Gorman, N C Barratt, K Imada, H R Wilson, G J Tallents, and I. T. Chapman. The influence of finite radial transport on the structure and evolution of $m / n = 2/1$ neoclassical tearing modes on MAST. *Plasma Physics and Controlled Fusion*, 54(8):085001, 2012.
- [32] Richard Fitzpatrick. Helical temperature perturbations associated with tearing modes in tokamak plasmas. *Physics of Plasmas*, 2(1995):44, 1995.
- [33] P. C. Gregory. A Bayesian revolution in spectral analysis. *AIP Conference Proceedings*, 568:557–568, 2001.
- [34] J. Schoukens, J. Renneboog. Modeling the Noise Influence on the Fourier Coefficients After a Discrete Fourier Transform, 1986.
- [35] S. O. Rice. *Mathematical Analysis of Random Noise*, 1944.
- [36] B. P. Lathi. *Modern digital and analogue communication systems*. 1983.

- [37] C. Chrystal, K. H. Burrell, B. A. Grierson, and D. C. Pace. Spatial calibration of a tokamak neutral beam diagnostic using in situ neutral beam emission. *Review of Scientific Instruments*, 86(10), 2015.
- [38] J. W. Connor, F. L. Waelbroeck, and H. R. Wilson. The role of polarization current in magnetic island evolution. 8, 2001.
- [39] R. Fitzpatrick, F. L. Waelbroeck, and F. Militello. The influence of the ion polarization current on magnetic island stability in a tokamak plasma. 13, 2006.
- [40] I. H. Hutchinson. *Principles of Plasma Diagnostics*, 2005.
- [41] R C Isler. An Overview Of Charge-Exchange Spectroscopy As A Plasma Diagnostic. *Plasma Physics And Controlled Fusion*, 36(2):171–208, 1994.